高圧下で合成された部分充填スクッテルダイトRxCo4Sb12 (R = La, Ce および Nd) の熱電特性

Muroran IT

MURORAN INSTITUTE OF TECHNOLOGY

DISSERATION THERMOELECTRIC PROPERTIES OF PARTIALLY FILLED SKUTTERUDITES $R_xCo_4Sb_{12}$ (R = La, Ce, and Nd) SYNTHESIZED UNDER HIGH PRESSURE

MONA Yuttana

THERMOELECTRIC PROPERTIES OF PARTIALLY FILLED SKUTTERUDITES $R_xCo_4Sb_{12}$ (R = La, Ce, and Nd) SYNTHESIZED UNDER HIGH PRESSURE

By

MONA Yuttana

A dissertation submitted in partial fulfillment of the requirements for the degree of Doctor of Engineering

Examination Committee: Assoc.Prof. Takeda KEIKI
Prof. Hideaki NAKANE
Prof. Chihiro SEKINE (Chairman)

Nationality: Thai

Previous Degree: Bachelor of Mechanical Engineering
North-Chiang Mai University, Thailand
Master of Energy Engineering
Chiang Mai University, Thailand

Muroran Institute of Technology
Division of Engineering

March 2019

Acknowledgements

During the Ph.D course of my graduate career I have benefited from the help, support, advice and suggestions of a great many people or even supported me in one way. Therefore, I would like to express my grateful appreciations and thanks to the followings:

Firstly, I would like to express my sincere gratitude to my advisor **Prof. Chihiro Sekine** and **Asst. Prof. Yukihiro Kawamura** for the continuous support of my Ph.D study, for their patience, motivation, and excellence knowledge. I am really honored by becoming a member of his group.

Besides my advisor, I would like to thank **Mr. Chul-Ho Lee, Mr. Kunihiro Kihou and Mr. Hirotaka Nishiate** from National Institute of Advanced Industrial Science and Technology (AIST) for their serious but valuable suggestions especially in an experiment and analyze data.

My sincere thanks to **Asst. Prof. Chatchawan Chaichana**, who provided me with an opportunity to join an intern at MurorunIT. Without they precious support it would not be possible to study in Phd.

My sincere thanks **Dr. Enda Toumey**, for support everything, for his continuous encouragement and guidance since my master degree until now. And providing many valuable comments that improved the presentation and contents of this thesis.

Thank you for my roommate A 405 **(Ju Boom, Ju Odd, Ju Ahn)** and **Namphon, Ping and Moll** and all students now in Physics of Strongly Correlated Electron Systems Lab for all happy days.

Finally, I am thankful to my family, especially my beloved **Maw Paweena**, for her continuous support. Her sacrificed her comfort for my higher education.

MuroranIT, March 2019 MONA Yuttana

– Sometimes it”s very hard to move on, but once you move on, you”ll realize it was the best decision you”ve ever made.

To my beloved

For their endless love, support and encouragement

Abstract

Improved of thermoelectric materials were synthesized using high pressure and high temperature methods (HPHT). The limits of filling guest ions in $CoSb_3$ synthesized by HPHT were explored. The used of high-pressure technique expanded the practical filling fraction limit. Explorations of rare-earth nature mischmetal (Mm) were also undertaken, using our group previous work to guide synthesis condition. High filling with guest ions resulted in lower thermal conductivity of approximately half the total thermal conductivity of original compound $CoSb_3$ compound over a wide range in temperatures. The electrical transportivity was enhanced, producing a high-efficiency TE material.

High pressure and high temperature synthesis techniques were then employed to high filling guest ions of individual mischmetal guest ions for TE materials. The performance was created to justify the use of high pressure. The effects of high filled guest ions in this study shows improvement of the *ZT* performance for $Ce_{0.37}Co_4Sb_{12}$ and $Nd_{0.33}Co_4Sb_{12}$, up to 0.26, 0.48 at 700 K and $La_{0.28}Co_4Sb_{12}$ is 0.03 at 300 K respectively. The increased *R* concentration is not only improved the *ZT* performance due to electron doping but also decreased the thermal conductivity due to a rattling behavior.

Suggestion for future work of high-pressure synthesis technique sometime the sample is very small and fragile. Therefore, we should be finding the new combine technique to get a large bulk sample and high density that suitable to measure at high temperature and must be preserving the impact of high filling fraction. Finally, it's should be providing a great boon with high *ZT* value.

List Of Contents

Pages

List Of Figures

Pages

List Of Symbols

TE	Thermoelectric material
ZT	Thermoelectric Figure of Merit
S	Seebeck Coefficient
ρ	Electrical Resistivity
σ	Electrical Conductivity
κ	Total Thermal Conductivity
κ_e	Electronic Thermal Conductivity
κ_l	Lattice Thermal Conductivity
n	Carrier concentration
μ	Carrier mobility
$S^2\sigma$	Power Factor
I	Current
V	Voltage
SPS	Spark Plasma Sintering
PGEC	Phonon Glass Electron Crystal
XRD	X-ray Diffraction
SEM	Scanning Electron Microscopy
EDX	Energy Dispersive X-ray Spectroscopy
PPMS	Physical Property Measurement System
TTO	Thermal Transport Option
PPMS	Physical Properties Measurement System

Chapter 1
Introduction

In this chapter, the basic thermoelectric (TE) concepts will be discussed. The concepts that are related to this thesis will be introduced and summarized, with no extensive theoretical details. Terms for thermal transport and electronic transport will be discussed, and there will be a brief overview of the usability of TE devices.

1.1 Energy Usage

The current consumption of fossil fuel has grown dramatically, whereas the new discovery of new sources has slowed down. With the reliance on fossil fuels, environmental pollution and global warming are growing. To generate energy through fossil fuel combustion results in a typical efficiency of 30-40%. The remaining 60-70% of the energy is lost to the environment.[1,2] This has led to efforts to develop new sources of energy, as well as advances in energy efficiency by recovering waste heat as energy.

Thermoelectric materials is one of the most interesting for new energy resources.[3,4] These materials convert waste heat energy directly into electrical energy from inefficient waste heat.[5–9] However, thermoelectric materials need to be tuned to achieve optimal performance. In order to enhance efficiency and properly understand their electronic transport and thermal transport properties, it is important to develop TE performance.

1.2 Overview of Thermoelectrics

Thermoelectric energy was discovered in the 1820s by Thomas Johann Seebeck. His investigations found that when two dissimilar materials were joined together, and the junctions held at different temperatures, a voltage difference develops which is proportional to the temperature difference,[10,11] as shown in

Figure 1-1. The ratio of the voltage developed to the temperature gradient ($\Delta V/\Delta T$) is related to an intrinsic property of the materials. This is because charge carriers (electrons or holes) at the hot side of the material have more thermal energy than carriers at the cold side, causing a net diffusion of mobile carriers to the cold side. Since there are more mobile carriers at the cold side than the hot side, the inhomogeneous charge distribution forms an electric field which opposes the diffusion. If the material is in an open circuit, equilibrium will be reached when the rate at which carriers diffuse from the hot side to the cold side is balanced by the rate at which carriers move from the cold side to the hot side, due to the electric field. Thus, in equilibrium potential will form in response to a temperature gradient; this potential is known as the Seebeck voltage. The amount of voltage generated per unit temperature gradient is called the Seebeck coefficient. If the material is connected to a circuit, the potential will drive a current which can be used to perform electrical work, which is the fundamental for thermoelectric power generation, as shown in Figure 2-2.

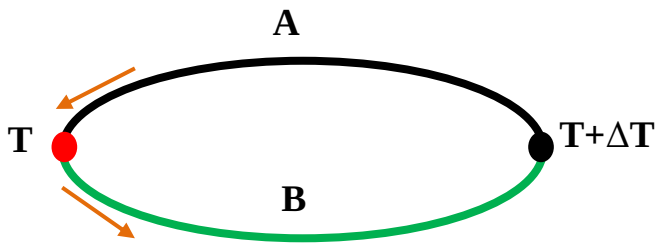

Figure 1-1. Thermodynamic circuit for the relative Seebeck coefficient

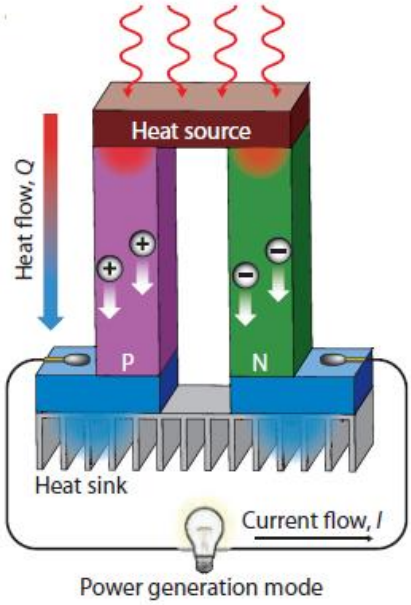

Figure 1-2. Schematic diagram of thermoelectric power generation [i]

Thermoelectrics can also be used as solid-state refrigerators or heat pumps by driving a current in a circuit with two dissimilar materials. This mode exploits the Peltier effect, discovered by Jean-Charles Peltier in 1834. Basically, heat is absorbed or rejected at the interface of two dissimilar materials, when a current flowed around a circuit as shown in Figure 1-3. This is explained by introducing the Peltier coefficient $\prod = ST$, which is a material dependent parameter, related to the Seebeck coefficient and described on how much thermal energy is carried per charge carrier. Since the heat current must be continuous across the interface of two materials. If the materials have different Peltier coefficients, heat will be either ejected or absorbed at the interface, depending on the sign of the difference between the Peltier coefficient and the direction of the current. If the current is injected in one direction the junction will extract heat, which is the basis for thermoelectric refrigeration. A current in the other direction will produce heat at the junction, and the device is acting as a heat pump. The rate at which the Peltier

[i] http://www.1-material.com/organic-thermoelectric-ote-materials/

heat is liberated or rejected at the junction (Q_P) is givenby $Q_P = SIT$, where I is the current through the junction and T is the temperature in Kelvin (K). Usually the two materials are chosen to be thermoelectric materials with the opposite majority carrier in Figure 1-4 (one n-type leg and one p-type leg) to maximize the difference between the Peltier coefficient and hence the amount of heat absorbed or generated

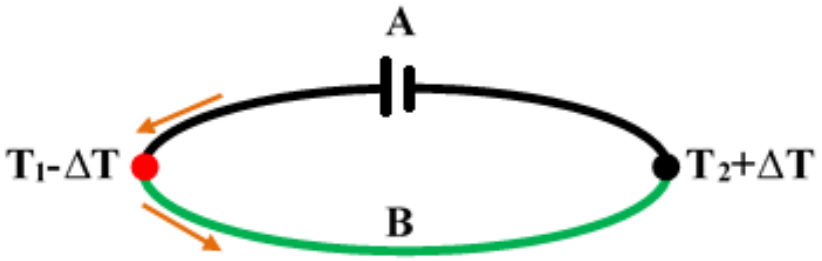

Figure 1-3. Thermodynamic circuit for the Peltier effect

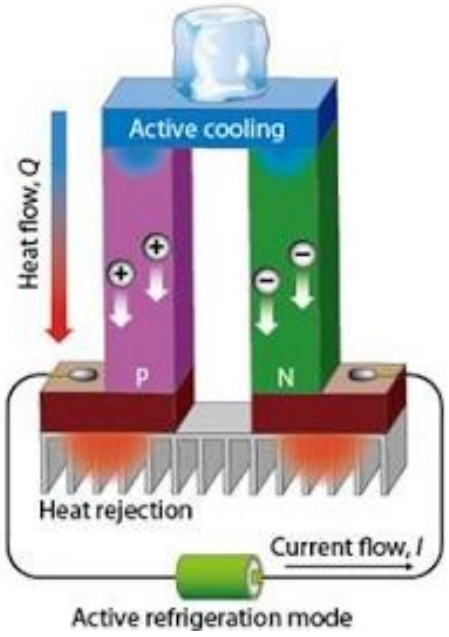

Figure 1-4. Schematic of thermoelectric refrigeration [ii]

[ii] https://sites.google.com/site/cl663lcj1/home/thermoelectric-materials

The guideline to develop applications to be accepted broadly are a focus on developing the performance of material by improving thermopower or decrease the thermal transport of material. The efficiency of thermoelectric devices is determined by the dimensionless figure of merit;

$$ZT = S^2\sigma T/\kappa \quad (1)$$

Where Z is the figure of merit, S is the Seebeck coefficient, σ is the electrical conductivity, T is the absolute temperature, κ is the total thermal conductivity. In the case of the total thermal conductivity can be separate with two terms is ($\kappa = \kappa_e+\kappa_l$), the electronic and the lattice contributions.[12–15] In order to maximize ZT of the material should be improved power factor ($S^2\sigma$) are required to be the highest and decrees κ to the lowest. Due to their transport property is needed to be optimized to achieve maximum ZT.

1.3 Improving Thermoelectric Performance

Improving thermoelectric performance is difficult due to the coupled nature of the relevant properties. Thermoelectric performance can be improved through two directions: improving the power factor, or lowering the thermal conductivity; however, a loss in one factor results in a losses in other factors. For example, increasing the carrier concentration is an easy way to raise electrical conductivity. However, doing so will generally decrease the Seebeck coefficient through changes in the Fermi level. In addition, if carrier concentration is increased to boost electrical conductivity, the electron contribution to thermal conductivity will increase as well. Therefore, ZT is obtained by carefully considering the carrier concentrations property.

Phonon Glass Electron Crystal (PGEC) [16] is a concept for improving ZT performance, by scattering phonons heat (rattle effect). This is possible due to the

differing lengths scales on lattice conductivity and electron conductivity, then PGEC materials attempt to reduce lattice thermal conductivity.

Thermal conductivity in TE materials comes from two sources: Electrons or holes transporting heat (κ_e) and phonons transporting of lattice (κ_l). By electronic term (κ_e) is directly related to the the Wiedemann–Franz law:

$$\kappa_T = \kappa_l + \kappa_e \tag{2}$$

$$\kappa_e = L\sigma T \tag{3}$$

Where L is the Lorenz number, 2.443 x 10^{-8} V^2/K^{-2} for free electrons.[15,17,18)]

1.4 Skutterudites-type thermoelectric

Thermoelectric Skutterudites-type one of the most promising class of thermoelectric materials, because they exhibit high hole mobility values, [3,16)] leading to high electrical conductivities, and they present a unique approach to reduce lattice thermal conductivity. The CoSb3-skutterudite structure includes two empty voids per unit cell, which can be filled with guest atoms for doping, with the aim of reducing lattice thermal conductivity.[14,18,19)] The $CoSb_3$-skutterudite structure of unfilled Skutterudite (a) and filled (b) are shown in Figure 1-5.

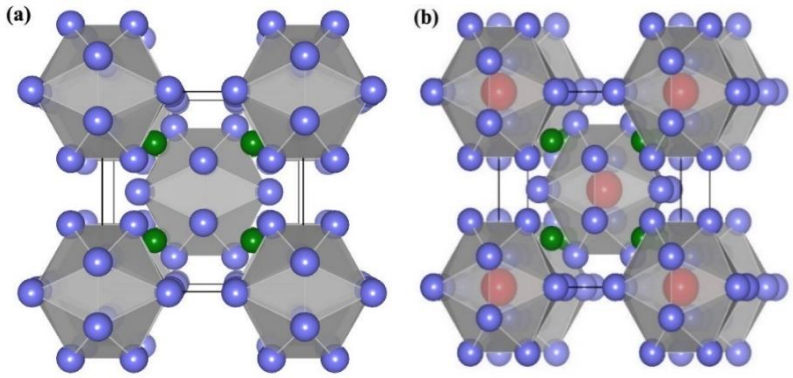

Figure 1-5. Schematic illustration of skutterudite crystal (a) Binary skutterudite structure; (b) Filled skutterudite structure

1.5 High Pressure and High Temperature Synthesis

High-pressure synthesis techniques, more familiar in experimental, in order to reach favorable synthesis conditions for the high filling fractions rate, which conventional under ambient pressure method can not improve upper limit. Which contrast of high-pressure technique, they can increase upper limit and improve *ZT* performance.

High pressure synthesis benefits to increase upper limit of filled guest atoms to the voids of the skutterudite structure than ambient pressure. $Mm_xCo_4Sb_{12}$, $Yb_xCo_4Sb_{12}$ and $Sn_xCo_4Sb_{12}$ have been succeeded synthesized by using high pressure and high-temperature method.[18–20] Those methods show various interesting physical properties. Furthermore, we can fill guest atoms to voids of skutterudite structure with high filling ratio and they show the advantages of fast process.

1.6 Research objective

The main objective of this thesis is to synthesize individual nature mixchmetal (Mm) filled $CoSb_3$-skutterudites TE materials for improved performance.

1. To study individually of Mm-filled skutterudite compounds with high filling fraction by using a high-pressure and high-temperature technique.
2. To synthesize and characterize the properties of high pressure filled skutterudite.
3. To investigate which element is more effective to fill skutterudite and can be used to design an artificial Mm-filled skutterudite for high *ZT* performance by using HPHT method.

Chapter 2
Experimental Methods

2.1 Chemical reagents

1) Cerium chunk, Ce, Rare Metallic co., Ltd.
2) Neodymium, chunk, Nd, Rare Metallic co., Ltd.
3) Lanthanum, chunk, Ce, Rare Metallic co., Ltd.
4) Cobalt, powder, Co, New materials and Chemical Ltd.
5) Antimony, powder, Sb, Soekawa Chemicals.
6) Ethanol, C_2H_6O.
7) Acetone, C_3H_6O.

2.2 High Temperature and High Pressure Synthesis

Although skutterudites could be synthesized without high pressure, high filling fractions targeted in this project required high pressure. All the samples reported in this work were synthesized by using the high pressure and high temperature apparatus (UHP-1500, Sumitomo Heavy Industries), as shown in Fig. 2-1. Kawai-type multi-anvil apparatus (6–8 system, sample pressure is generated by successive com- pression:

(1) A hydraulic ram drives six first-stage anvils.

(2) The six first-stage anvils compress eight second-stage anvils.

(3) The second-stage anvils compress an octahedral cell assembly.

Tungsten-carbide cubes with a truncated edge are used as the second-stage anvils. The sample cell assembly is similar to that used for the cubic anvil apparatus (Fig. 2.2). The sample container, made of magnesia (MgO + 5% Cr_2O_3), was transformed into an octahedron. The starting materials were put in a crucible made of BN. The crucible, with a graphite heater surrounded with a zirconia (ZrO_2) thermal insulator, was inserted into the magnesia octahedron.[13)]

The heat system is achieved by current heating method. The AC current is passed from the cubic tungsten, transfer to graphite heater. The temperature inside the graphite tube will be increased. A hole were punched in the place which tangency to the graphite. The temperature is detected by putting a K-type thermocouple in the hole.

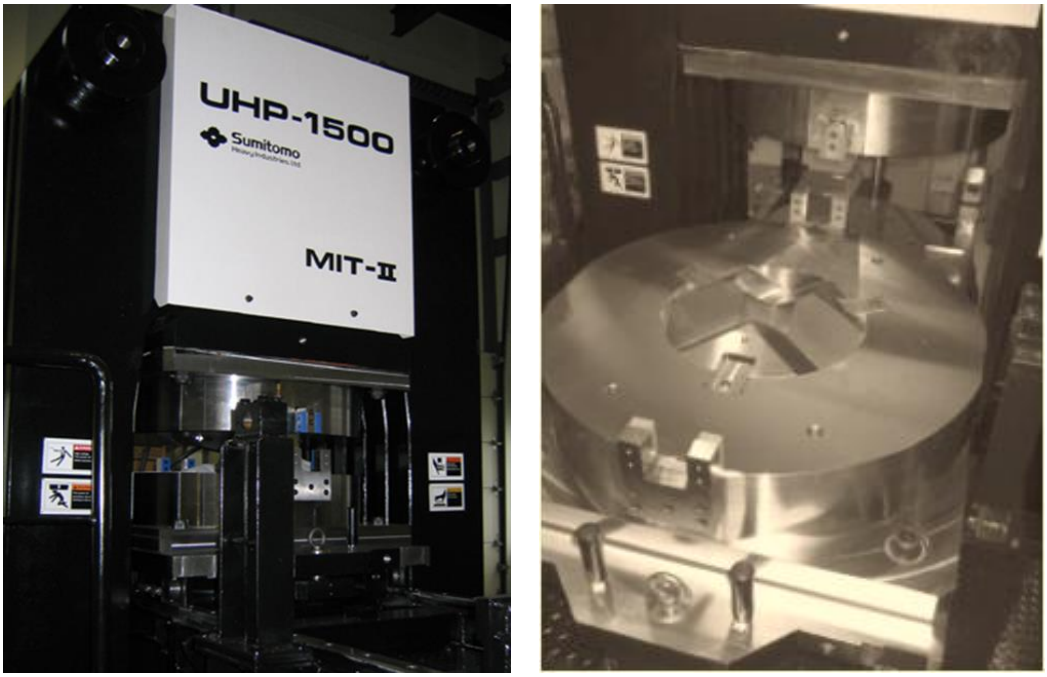

Figure 2-1. Kawaii-type multi-anvil apparatus UHP 1500 and guide block.

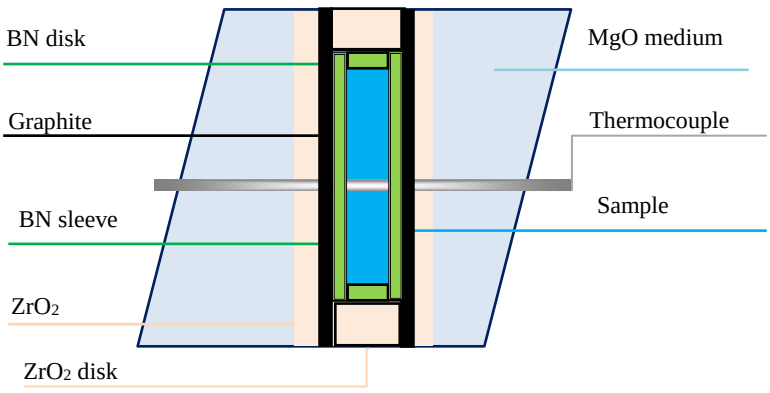

Figure 2-2. Cell assembly anvil high-pressure apparatus.

High-purity Cerium (Ce), Neodymium (Nd) or Lanthanum (La) powders were mixed and milled in stoichiometric ratio using the agate mortar and then sealed in the BN capsule. The octahedral magnesia in Fig. 2-2 was pressed to 4 GPa and heat generated. The heating rate was 37 °C/min and the target temperature 900 °C. Keep the temperature at 900 °C for 2 minute and then decrease to 600 °C and keep at 600 °C for 120 minutes. The displayed temperature depends on the precious of the parts, especially the place of the thermocouple. Therefore, the temperature cannot be controlled only depend on the temperature, but also need pay attention on the current power.

2.3 Spark Plasma Sintering (SPS)

Spark Plasma Sintering (SPS) is a sintering process that make large bulk sample and densification. By SPS pulse current flow through the graphite mold and stacked sample powder. The system consists of a SPS sintering machine with a vertical single-axis pressurization mechanism, two punch electrodes with built-in water cooler, a water-cooled vacuum chamber, a vacuum/air/argon-gas atmosphere control mechanism, a cooling water control unit, a position measuring unit, a special DC-pulse sintering power generator, an applied pressure display unit and other interlock safety unites. All samples from HPHT after remove impurity were pulverized into powders with a mortar. The powders was then placed into a 10 mm diameter graphite die with graphite sheet in between the powder and graphite punches for the ease of removal after sintering and a more uniform current flow. The graphite die was then placed in between graphite spacers with a thermocouple placed in a hole on the side of the die to measure the temperature of the powder during the sintering. After setting up the place for the graphite die, the chamber was closed and the furnace was purged and backfilled with Argon three times to ensure a vacuum environment before sintering. This study is sintering sample was pressed at up to 60 MPa and kept at 600 °C for 120 min.

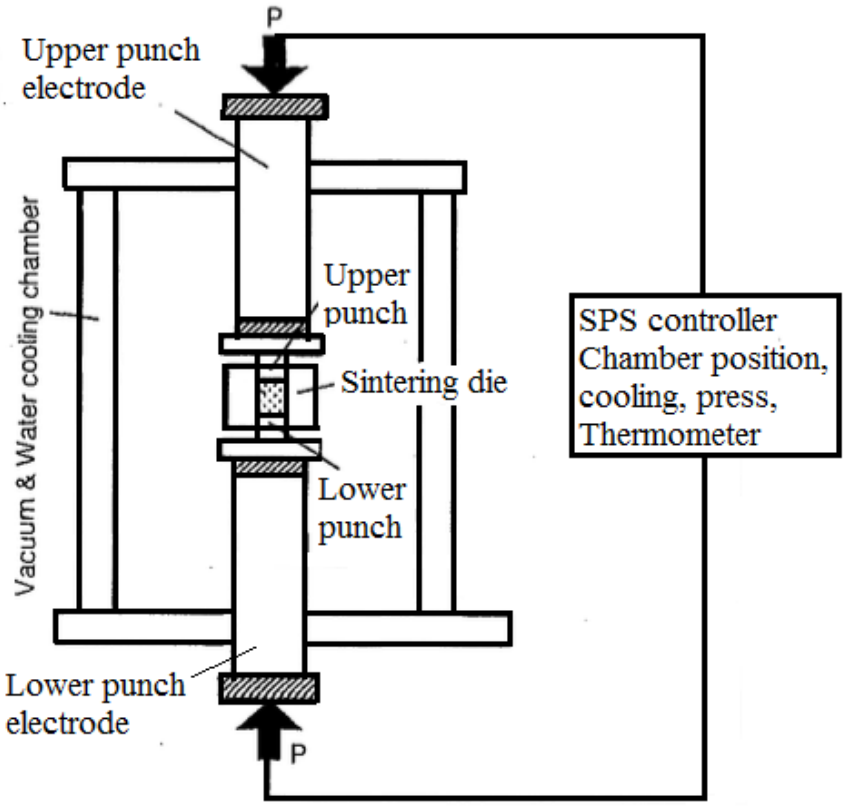

Figure 2-3. Schematic diagram of Spark Plasma sintering (SPS).

2.4 X-Ray Diffraction (XRD)

X-Ray Diffraction is an analytical tool to obtain crystallographic information of materials. It is a non-destructive, reproducible and fast characterization technique to identify crystalline phases and orientation, to determine structural properties such as crystallite size, lattice parameters, grain size, phase composition, atomic arrangement etc. The interaction of the incident beams with the sample produces diffracted beams that satisfies the Bragg's law

$$n\lambda = 2d\sin\theta \tag{2.1}$$

This equation relates the wavelength of electromagnetic radiation (λ) to the diffraction angle (θ) and the lattice spacing in a crystalline sample (d). As illustrated in figure 2-3

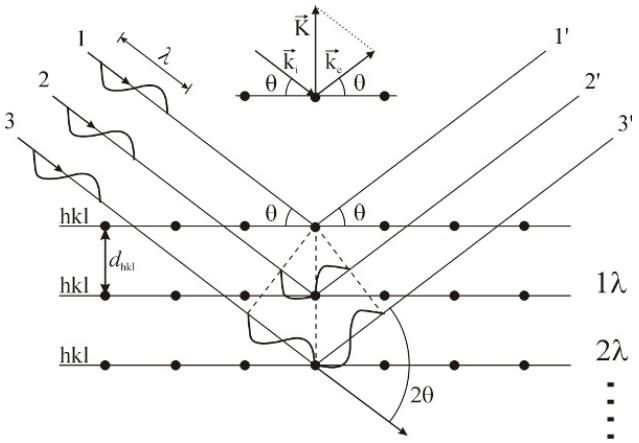

Figure 2-4. Basic working of X-Ray diffraction

by scanning the sample through a range of *2θ* angles, all possible diffraction patterns of the lattice is obtained due to the random orientation of the material. Diffracted X-ray beams are detected, processed and counted. By analyzing the position, shape and intensity of the diffraction peaks important atomic and molecular structure of the crystal can be obtained. Rigaku RINT-RAPID-II using Co $K\alpha_1$ radiation and silicon as a standard wavelength source of 1.5406 Å wavelength.

2.5 SEM and EDX

Scanning Electron Microscopy (SEM) is a very convenient and dynamic characterization tool to obtain high-resolution microstructure images of desired materials. SEM utilizes electrons for imaging as they have much shorter wavelengths than light, enabling better resolution and magnification. SEM can be operated in various modes for analyzing surface morphology, elemental composition, microstructure studies etc.

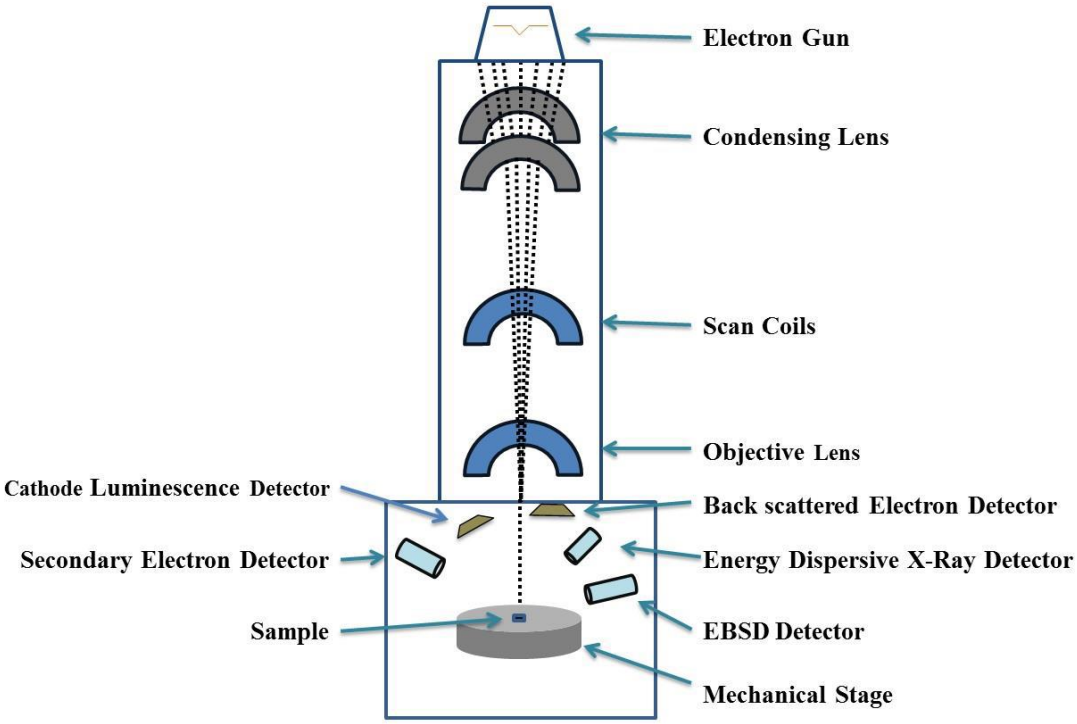

Figure 2-5. Schematic diagram of a typical Scanning Electron Microscopy.

The basic working principle of SEM is a beam of incident electrons, which is generated in an electron column above the sample chamber. Depending on the evaluation objectives the energy of the incident electrons may vary from 100eV up to 30 keV. The electrons generated are focused into a small beam by a series of electromagnetic lenses in the SEM column. Scanning coils near the bottom of the column direct and position the focused beam onto the sample surface. The incident electrons cause electrons to be emitted from the sample due to elastic and inelastic scattering from the sample's surface and nearsurface material. High energy electrons that are ejected by an elastic collision of an incident electron are referred to as backscattered electrons. Back scattered imaging mode provides image contrast as a function of elemental composition, as well as, surface topography. Emitted lower energy electrons resulting from inelastic scattering are referred as secondary electrons. The SEM column and sample chamber are maintained at a moderate vacuum to allow the electrons to travel freely from the

electron beam source to the sample and then to the detectors. Energy Dispersive Spectroscopy (EDS) is an analytical tool used for the elemental analysis or chemical composition of the materials. Backscattered electron images in the SEM shows compositional contrast that results from different atomic number elements and their distribution. EDS allows to identify what those particular elements are and their relative proportions (Atomic % or weight %).

2.6 TE properties characterizations at low Temperature.

Thermoelectric measurements, including Seebeck coefficient (S), and thermal conductivity (κ), were performed on synthesized pellets in a Quantum Design Physical Properties Measurement System (PPMS) coupled with the thermal transport option (TTO). The measurements were done at room temperature.

TTO option is used to measure the thermal transport properties, thermal conductivity κ, Seebeck coefficient S and electrical resistivity ρ. However, the epoxy bond paste which used to fix sample influenced the precious of resistivity, therefore, we will measure resistivity using the standard four-probe method is for the measurement with AC transport mode. The advantage of the four-probe method is that it can prevent the problem from a contact resistance occurred in a two-probe configuration. That is, only thermal conductivity κ and Seebeck coefficient S value were provides the information from TTO option.

The TTO system determines the thermal conductivity κ and Seebeck coefficient S by creating a specified temperature drop between the two ends of sample. The sketch map of sample assembled for TTO measurement is shown in Fig. 2-6. The sample end is adhere to the leads by epoxy bonds. Heat is applied to one end of the sample by running current through the heater ($Q_{+/-}$). In the TTO system, the thermal conductivity the heater source applies heat to a sample and the amount of heat passes through the sample is collected from the observed temperature drop. Thus, thermal conductivity can be calculated directly from

three parameters: an applied heater power, a resulting ΔT, and a sample dimension and the Seebeck coefficient provides the information about the thermal diffusion of free charge carriers, which can be an electron or a hole. According to the majority carrier, charge carrier diffusion generates an electric field inside a material which creates a voltage gradient when a temperature gradient is applied. The TTO system measures Seebeck coefficient by originating a particularized temperature difference (ΔT) and monitoring an electrical voltage difference (ΔV). The ratio of these two measured parameters ($\Delta V/\Delta T$) is equal to S are calculated as follows:

$$\kappa = \mathrm{Q} \cdot \frac{d}{T_{hot} - T_{cold}} \tag{2. 2}$$

$$S = \frac{V_+ - V_-}{T_{hot} - T_{cold}} \tag{2. 3}$$

where T_{hot}, T_{cold} is the temperature measured at the thermometer shoes (copper lead); V+, V- is the voltage responded at the sample two ends during the heat pulse; Q is the heat energy and d is the height of the sample.

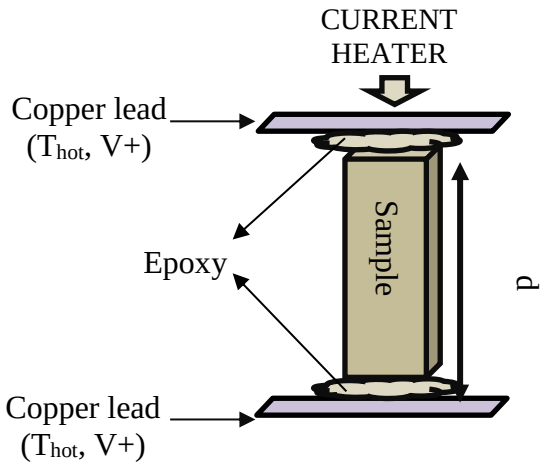

Figure 2-6. Sketch map of sample connect for TTO.

For TTO measurement, the sample should be modified to rectangular bulk about (2.0mm×1.0mm×0.5mm). The surface should be polished with abrasive paper

(#3000 and #8000) and cleaned. After measured the size of sample, the sectional area and the total surface area of the other 4 surface need calculated by self. The mounting sequence proceed as below with the help of a puck-mounting station.

(1) Prepare adhesive agent (Silver-filled H20E epoxy). Take out equivalent part A and part B of epoxy bond (made by EPO-TEX. Co.) on the clean paper by using toothpick. (The toothpick for taking Part A and Part B should be separated.) Mixed the part A and Part B thoroughly using another new toothpick.

(2) Prepare copper lead. As shown in Fig. 2-6, there are two kinds of copper lead. Shape a can be used for small sample while shape B can be used for big sample. Besides, the shape b need to be cut to shape c for the convenient of assembling. Those copper lead can be used again after measurement.

(3) Adhere copper leads to the ends of sample. Adhere sample to copper lead as shown in Fig. 2-7 and heat it at 150°C for 5 min. A

(4) few of epoxy bond would be enough because too much epoxy will influenced the measurement result.

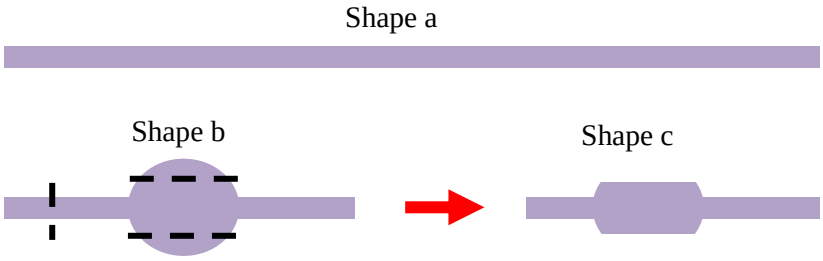

Figure 2-7. Shape of copper lead.

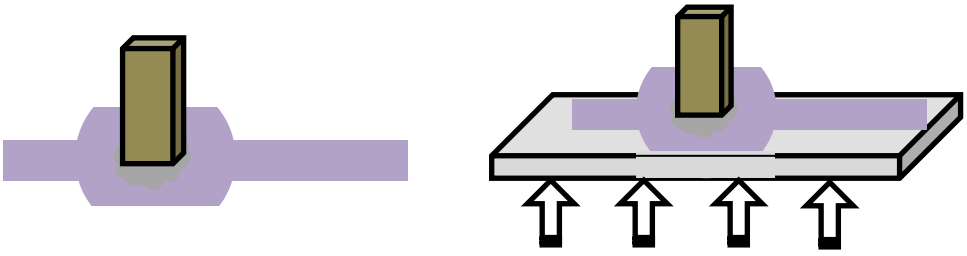

Figure 2-8. Adhere lead to bottom end of sample.

After the bottom of the sample is fixed to the lead, adhere the other lead to the top of sample. Before adhere the lead to the top end of sample, the lead should be bended to the following shape as fig 2-8.

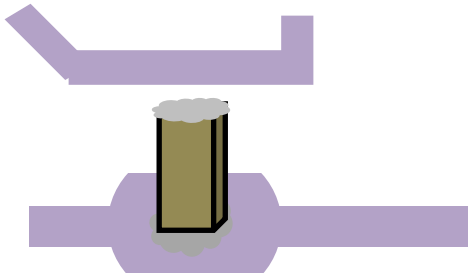

Figure 2-9. Adhere lead to the top end of sample.

(5) Install shoes for sample. Because the shoe is very easy soft, so excessive force or mis-threading of the piece can easily damage the threads. The corresponding sample lead need inserted and held in the shoe by hands and a small stainless steel metric M1 screw carefully. The metal tweezers cannot touch the shoes at any time. The sequence of assembling shoes is: Hot-Heat-Cold.

(6) Install sample on TTO puck. Place the puck in the TTO puck-mounting station and clamp the cold-foot lead to the cold-foot on the puck with the help of the small screwdriver. Then, the other end of each shoe should also inserted to corresponding in Fig. 2-9. In addition, all of the line should neither touch each other nor any part of the puck.

(7) Place the shield on the puck. Remove the shield cap and screw the shield carefully into the base of the puck. Be care to verify that no wires, shoes, or the sample do not touch the shield. Replace the shield cap after fixed the shield well.

(8) Checking the sample contact. In order to ensure the condition of sample contact is well or not, the electrical contact to the sample must be checked

after mounting it on the puck. Plug the puck into the test box and check resistivity between V+/- and I+/- with an ohmmeter. The corresponding resistivity value should be:

3-4: around 200Ω;

5-6: around 2 kΩ;

7-8: around 100Ω;

9-10: around 100Ω;

11-12: show different resistivity value according to sample property;

13-14: show different resistivity value according to sample property.

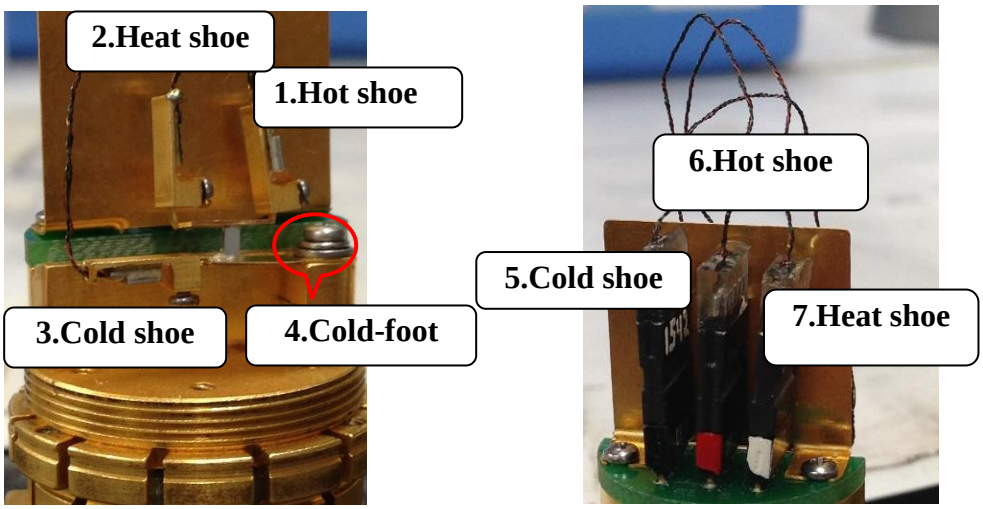

Figure 2-10. Illustrating sockets shoe.

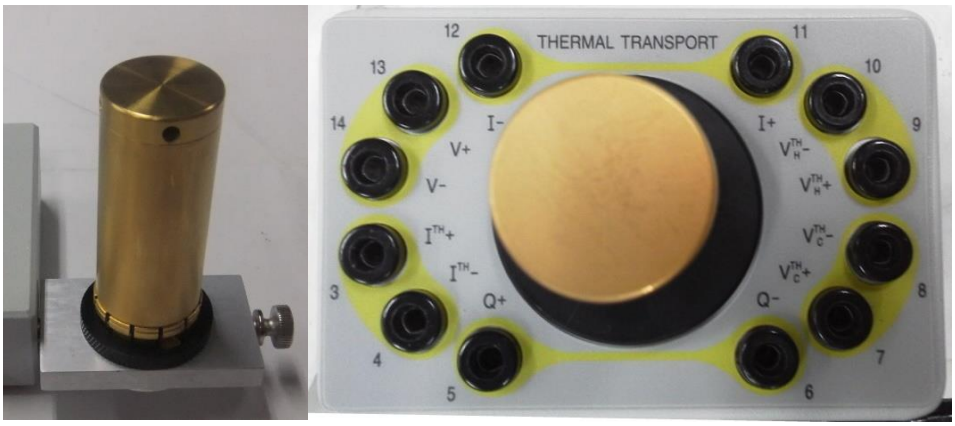

Figure 2-11. Sample holder with the shield.

After assembled sample on the parts, the measurement sequence need to be prepared as following.

(1) For TTO measurement, the thermal transport option need to be active if not currently active. Do the following at the PPMS Multivu window: select **Utilities – Activate Option**, click on **Thermal Transport** under the Available Options heading, and then select **Connection Diagram**.

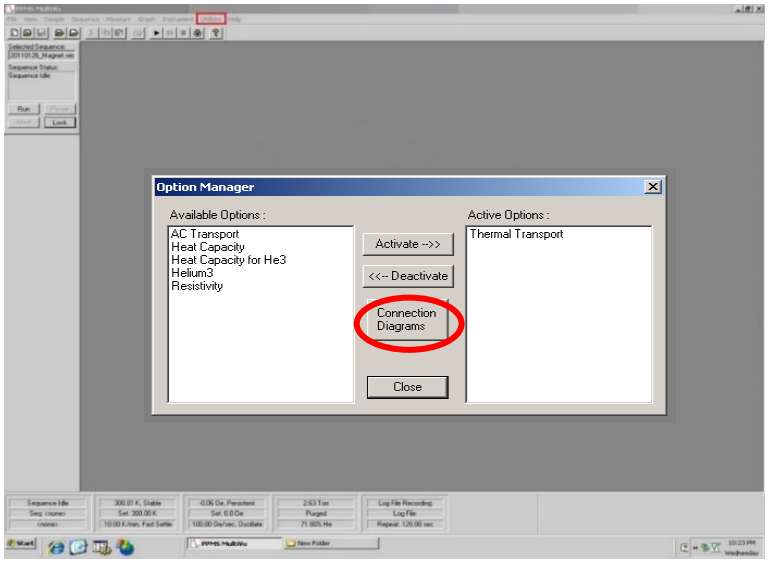

Figure 2-12. PPMS Option Manager.

(2) Change cable according to the Connection Diagram.

(3) Check the Power. TTO measurement use the MODEL6000, MODEL6500 and MODEL7100 (Fig.2-13). Sometimes only MODEL6000 is active, if so, the power of MODEL6500 and MODEL7100 need to be turn on and then restart the PC.

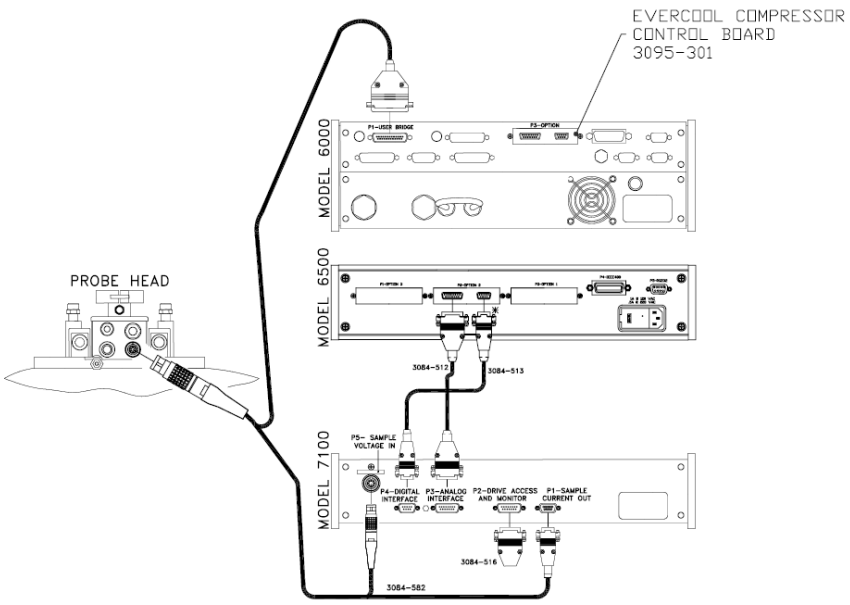

Figure 2-13. TTO connect diagram.

Figure 2-14. Model 6000, Model 6500 and Model 7100.

(4) Ensure temperature setting at 300 K. Before open the chamber, first ensure the temperature is 300 K. If the temperature of the chamber is low, open the chamber will result frost in the chamber and cannot vacuum.

(5) Insert sample in the chamber. Do the following fig 2-14: click **Vent Cont.** button at the **Chamber** windows; After the state became Flooding at the

bottom of the status bar. Insert the sample puck inside the chamber using the sample insert tool as shown in the Fig. 2-15.

(6) Assembled Charcoal (4038-010) in the bottom of the Contact Baffle (as illustrated in Fig. 2-16 and insert it inside the chamber and then close the chamber. The Charcoal will help to create a more uniform thermal environment for the puck when high vacuum is enabled in the chamber.

(7) Click **Purge/Seal** button to vacuum the chamber. Wait until the status become purged, then click the **HiVac** button. The status will show AtHiVac when the chamber became high vacuum.

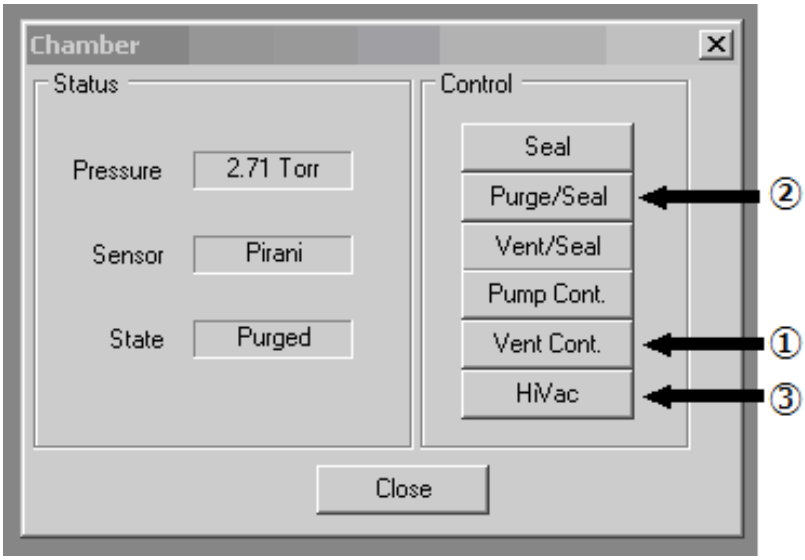

Figure 2-15. Chamber control window

Figure 2-16. Sample insert tool.

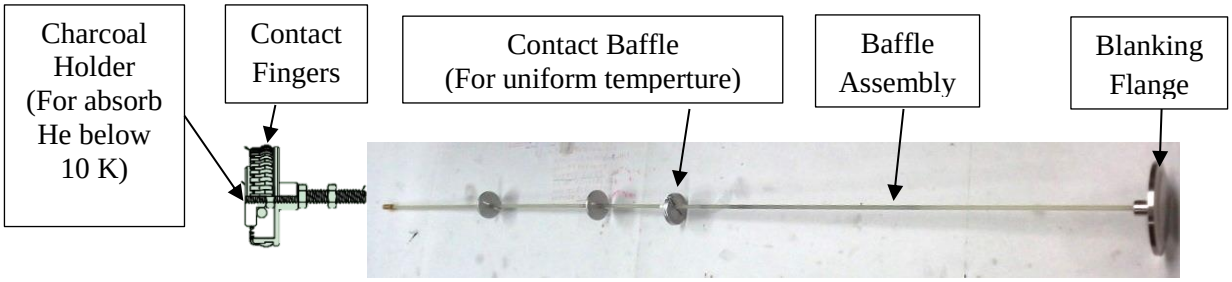

Figure 2-17. Charcoal and Contact Baffle Assembly.

(8) Active TTO option. Choose the **Thermal Transport** and the click the **Activate** button. Because only one measurement option may be active at a time, first click Deactivate if the another option is activate and then activate Thermal Transport option.

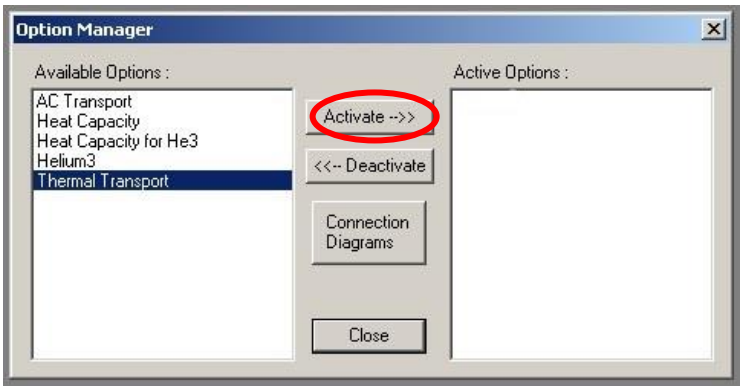

Figure 2-18. Option manager

(9) Ensure the Config file. After activate the Thermal Transport option, the windows in Fig. 2-19 will be shown. Thermal transport log window signify the Config file of the Hot, Cold and heat, respectively. The number indicated in Thermal Transport log should be same with the Hot, Cold and Heat shoe number which used in sample puck.

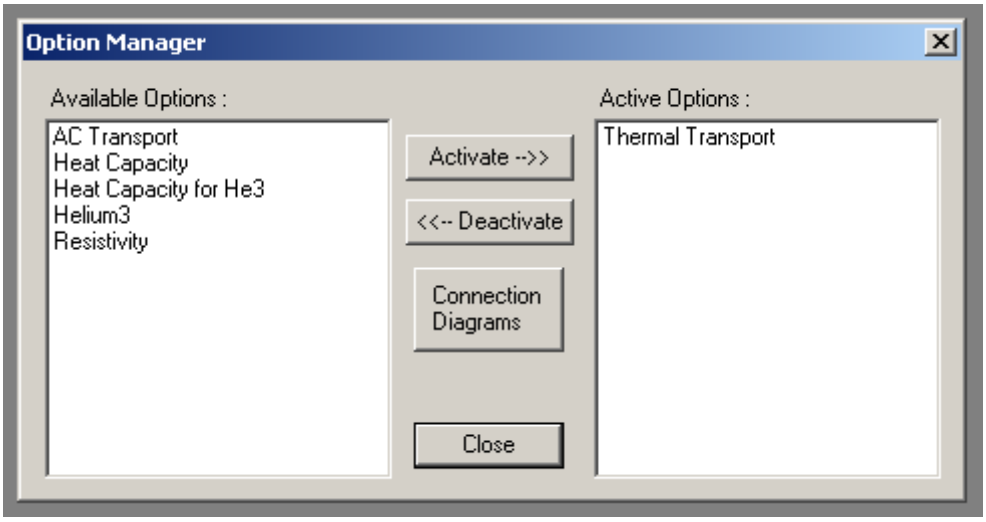

Figure 2-19. Windows after activate the Thermal Transport option.

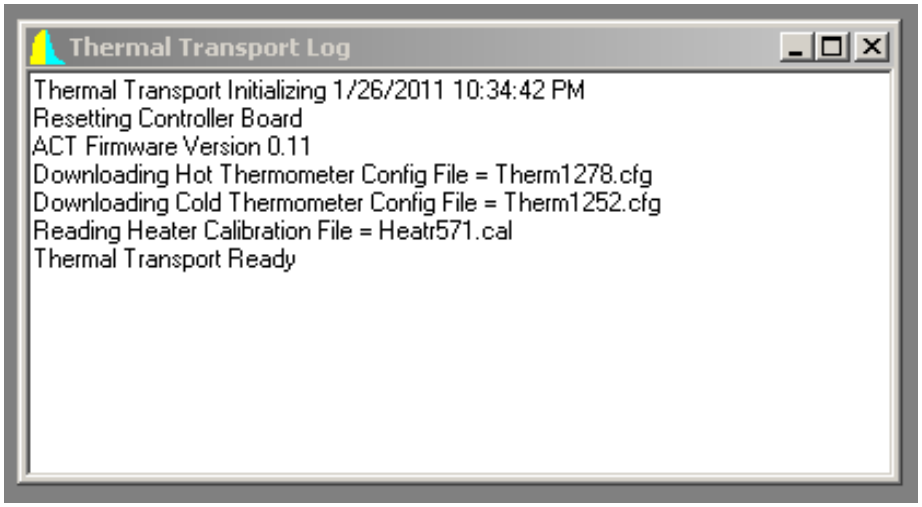

Figure 2-20. Change the Config File in Thermal Transport Log

(10) Click the data file in the Thermal transport windows as shown in Fig.2-20. Click the Browse button to make a data file. Fig.2-21 shows the input windows of sample information. Input the sample length, cross section and Surface Area.

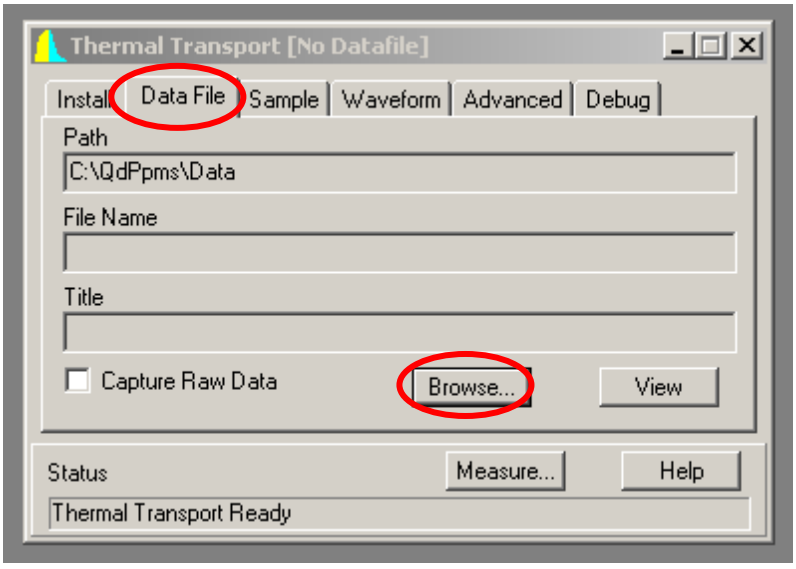

Figure 2-21. Data file.

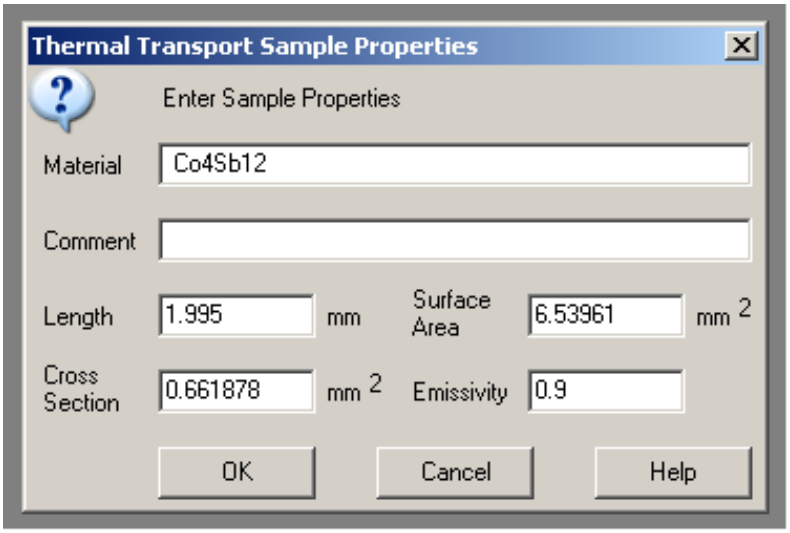

Figure 2-22. Sample information.

(11) Click the **Measure** in the bottom of the Thermal transport window. The Thermal Transport Measurement windows shown in Fig. 2-22 will be shown. Change the parameter shown in the red circle and click Start button. Wait few minutes to check the waveform. The corrected waveform is shown in Fig. 2-23.

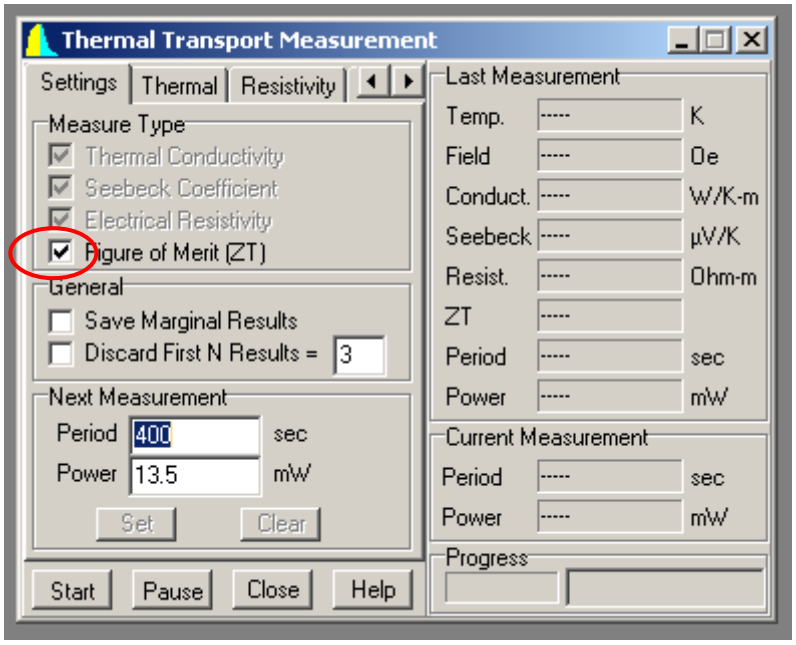

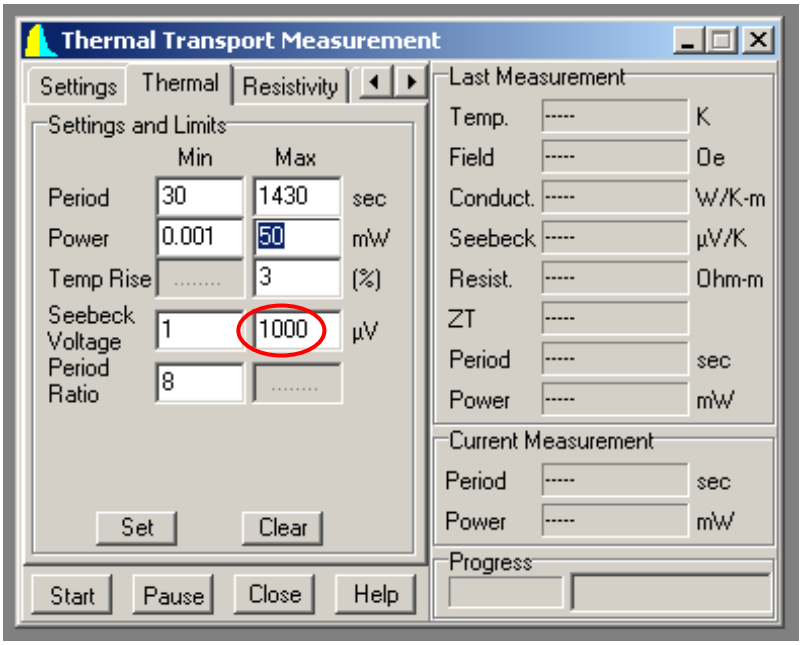

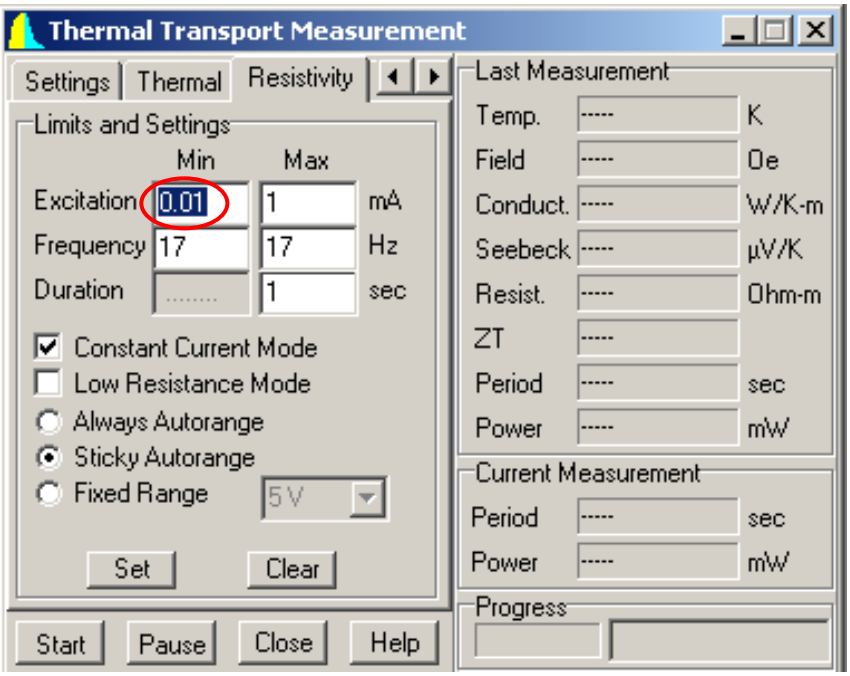

Figure 2-23. Thermal Transport Measurement.

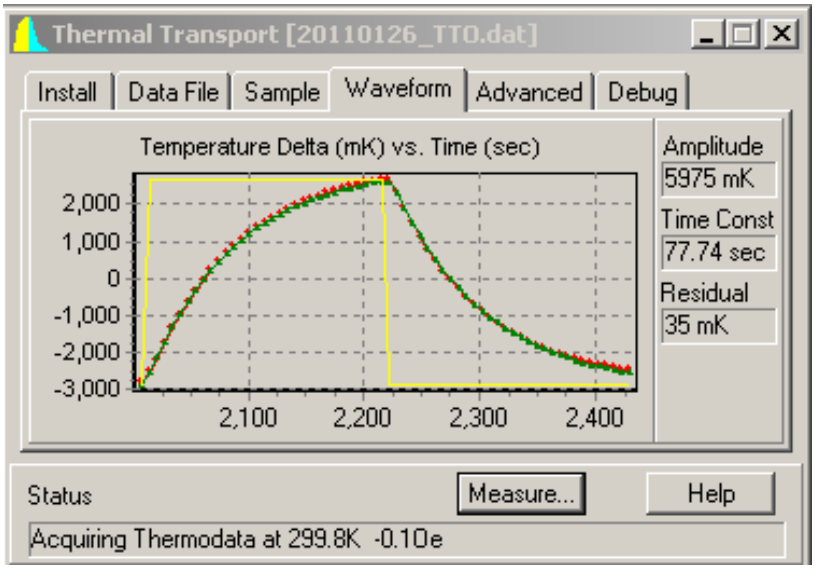

Figure 2-24. Thermal Transport Waveform.

(12) Write Sequence. As shown in Fig. 2-25. To get stable data at 300K, the temperature was keep at 300 K for 1 hour and then decrease to 5 K with 0.3 K/min.

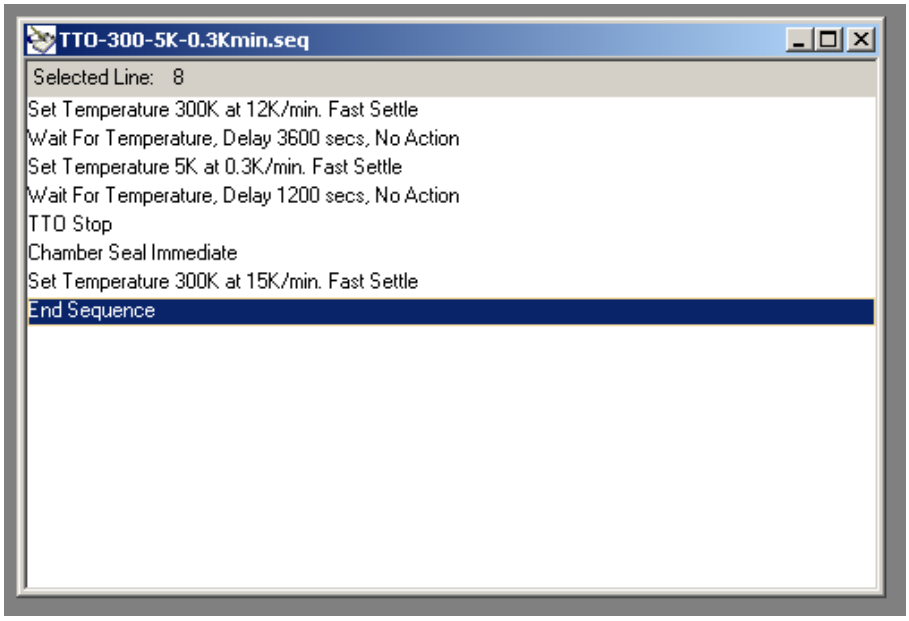

Figure 2-25. Example of TTO Sequence.

(13) Run sequence and clicking the **View** in the **Data File** panel of the Thermal Transport Windows to open the result figure.

In addition, the Log need to be taken for any measurement. Do the following: **Utilities/Log PPMS Data/General-Browse**, make a new folder and click open, **Select all** the Standard Item and Diagnostic Items/Click **Start** button to take the Log data/Click the **View Data** to show the Log Data.

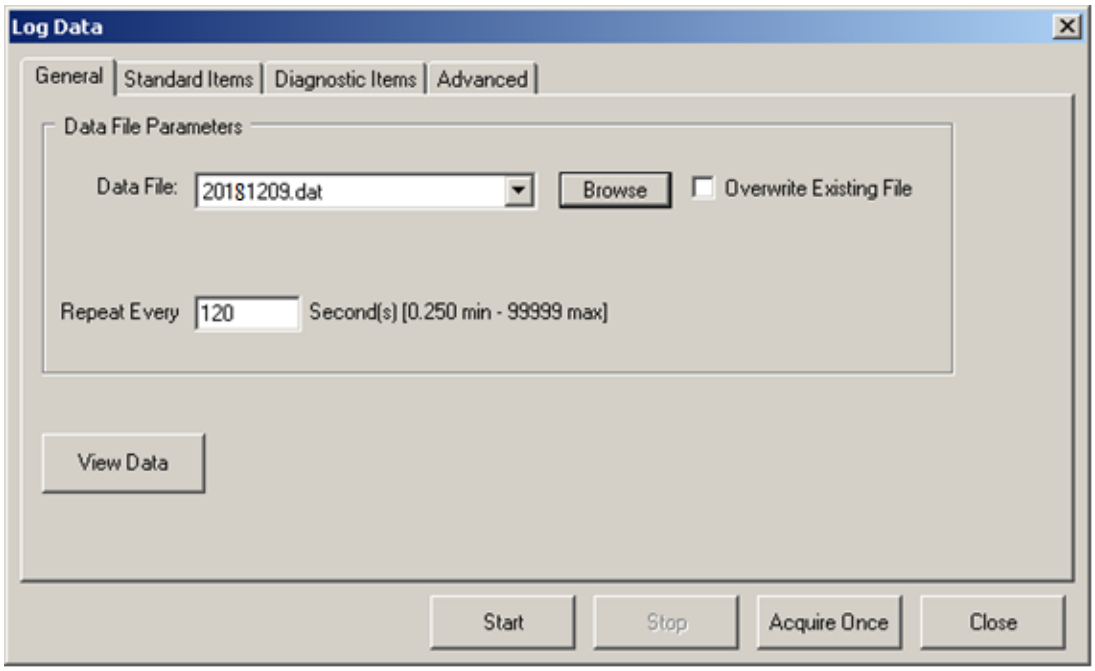

Figure 2-26. Log Data.

(14) After the measurement finish, the status in left will became **Sequence Idle**. Ensure the chamber temperature is 300K. Then, open the chamber by click **Vent Cont.** Button. Then open the Dewar and take off the sample. Close the Dewar and click **Purge/Seal** button to seal the chamber.

2.7 Resistivity

The electrical resistivity at T < 300 K were evaluated by the cryostat apparatus using four-wire resistance measurement method, the sample resistivity can be precious measured with greatly reduction of the contribution of the leads and the joints to the resistance. Fig. 2-27 shows the attach way of wires on the sample. After attached the wire on sample one by one, the sample with four –wire is mounted on resistivity plate and wired to the four contact. The outer wire contact applied current on sample and the inside two wire detect the voltage between the inside wires. The resistance then can be calculated with Ohm's law. Fig. 2-27 shows the schematically and actual four-wire resistivity sample.

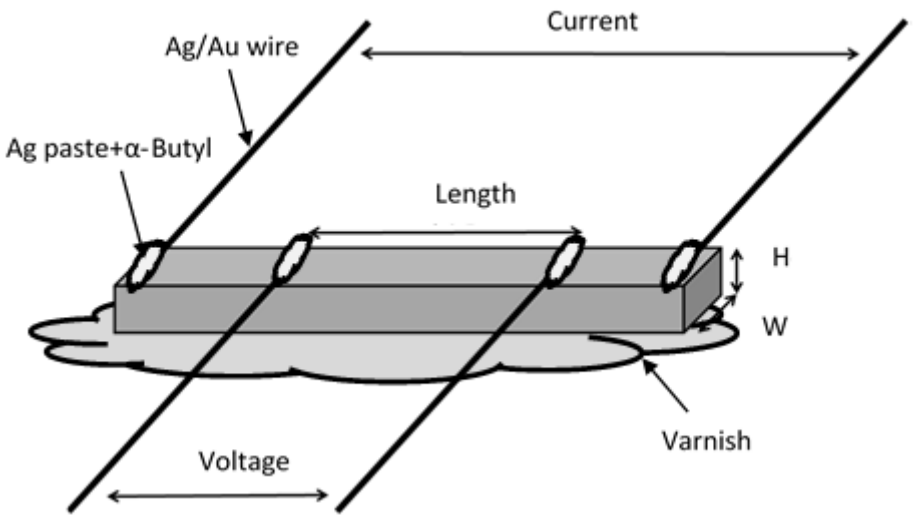

Figure 2-27. Four-wire resistivity measurement.

2.8 Hall effect

The importance of the Hall effect was needed to determine accurately carrier density and the mobility of carriers in sample materials. The objective of the Hall measurement in the van der Pauw technique was to determine the sheet carrier density by measuring the Hall voltage V_H. The Hall voltage measurement

consisted of a series of voltage measurements with a constant current I, and a constant magnetic field B applied perpendicular to the plane of the samples. Conveniently, the samples showed in Figure 2-28, were also used for the Hall measurement. To measure the Hall voltage V_H, a current I was forced through the opposing pair of contacts 1 and 3 and the Hall voltage V_H (= V_{24}) was measured across the remaining pair of contacts 2 and 4. Once the Hall voltage V_H was acquired, the sheet carrier density was able to be calculated via V_H = IB/nqt or R_HIB/t, (R_H = 1/nq) from the known values of I, B, and q, t (where q was the elementary charge, 1.602 x10^{-19} Coulomb and t is a thickness.).

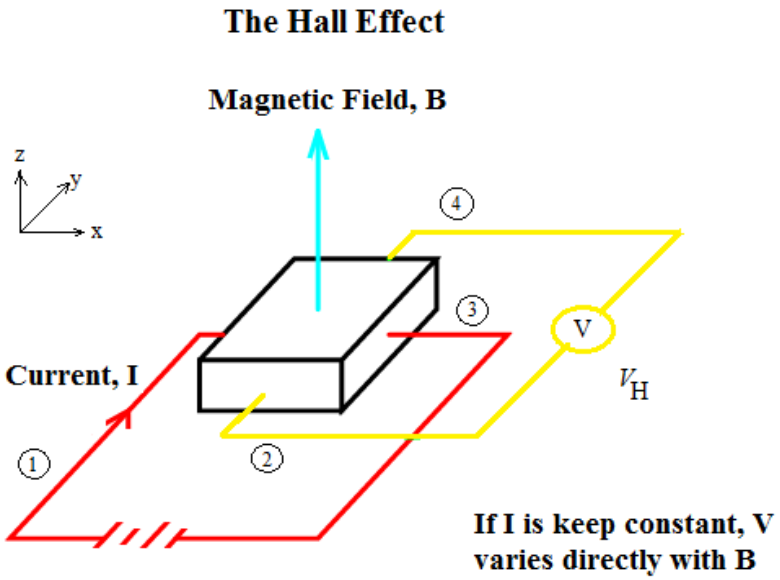

Figure 2-28. Schematic used for the determination of Hall voltage V_H.

We measure Hall effect by using van der Pauw technique, that is, a combination of a resistivity measurement and a Hall measurement. The sample shape for Hall effect measurement is a rectangle, as shown in fig. 2-29. A Fig.2-29, a current I is forced through the contacts I^+ and I^- and the Hall voltage V_H (=$V_{+/-}$) is measured across the remaining contacts V^+ and V^-. The hall coefficient can be expressed as:

$$R_H = \frac{V_H d}{IB} \times 10^8 \ \ (cm^3/C) \tag{2.4}$$

where d is the thickness of sample (cm) and B is the applied magnetic field (Oe), I is the applied current (A), and V_H is the corresponding voltage. According the value of Hall coefficient, the information of main carrier type can be obtained. The corresponding carrier concentration can be calculated by using:

$$n = \frac{1}{|R_H|e} \tag{2.5}$$

Combining with the results of resistivity measurement, the carrier mobility can be estimated by:

$$\mu = \frac{|R_H|}{\rho} \ \ (cm^2/v \cdot s) \tag{2.6}$$

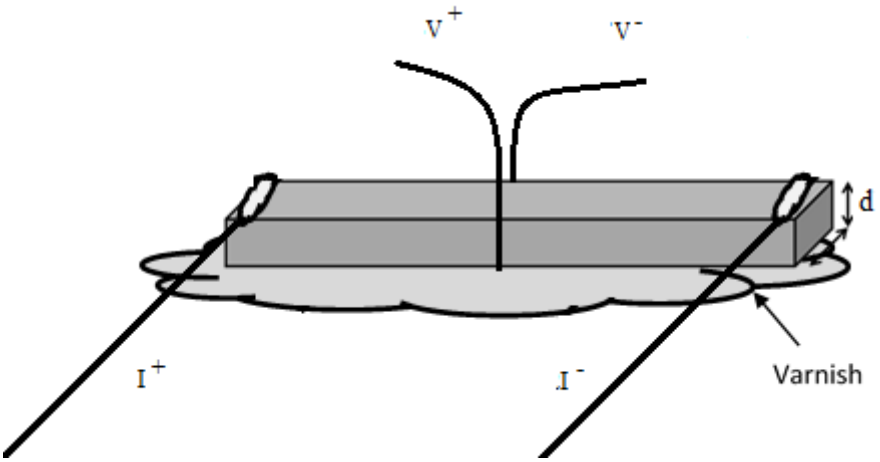

Figure 2-29. Four-wire Van der Pauw Hall effect measurement.

2.9 TE Transport Evaluation at High Temperature.

Thermoelectric power is essential to evaluate the performance at high temperature. ZEM-3 is a device for simultaneous measurement of both Seebeck

coefficient and electrical resistivity under an inert gas. The instrument permits measurement of both 6-22 mm long prism and cylindrical samples. The sample holder used as a unique balance contact mechanism, permitting measurement of high reproducibility. V-I plots were made to judge if the lead is in intimate contact with a set sample. Measurement was controlled by a computer, permitting automatic measurement with each temperature difference. Temperature range was to be raised from room temperature to 500 ^{o}C in this study.

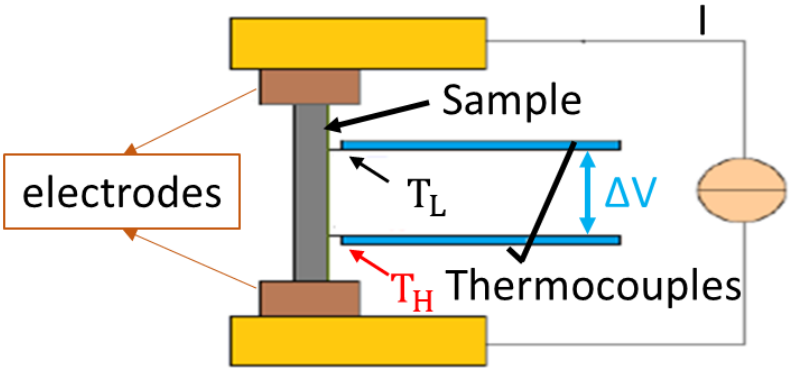

Figure 2-30. Schematic of Seebeck measurement for ZEM-3 unit.

Figure 2-31. A picture of ZEM-3 unit.

In the ZEM-3 system, during the Seebeck measurement, The Seebeck voltage is detected from two voltage probe leads. Together with the temperature signal from the same two thermal couples, Seebeck coefficient is determined. Fig.2-30 shows a detailed schematic of the Seebeck measurement configuration. The actual equipment for the Seebeck measurement is shown in Fig. 2-31.

2.10 Thermal Conductivity Measurement at High Temperature.

A Laser Flash apparatus (LFA) were used to measure three thermal constants: thermal conductivity, thermal diffusivity, and specific heat. Thermal conductivity (κ) was calculated from thermal diffusivity (κ_{dif}), heat capacity (Cp), and sample density (d) based on the relationship $\kappa = \kappa_{dif} C_p d$. The C_p and κ_{dif} was measured under vacuum using the laser flash apparatus (LFA, 457) as shown in Figure 2-32. Whereas the density can calculate by sample size. Thermal diffusivity represents how fast a body can dissipate thermal energy. Or in other words, how fast a body can change its temperature when there is a heat flow through it.

Figure 2-32. A laser flash apparatus LFA 457.

Chapter 3
Experimental Results of $Ce_xCo_4Sb_{12}$

3.1 Introduction

Highly mischmetal (Mm) filled skutterudite $Mm_{0.6}Co_4Sb_{12}$, prepared under high-pressure technique, exhibits a low κ_l of 1.34 W/Km and shows a relatively high *ZT* of 0.25 at 700 K.[13] The large reduction of κ_l suggests that the rattling effect and the mass fluctuation scattering are significant in this system.[17]

Mm is an alloy of rare earth elements in various naturally occurring proportions. A typical composition includes approximately 50% Ce and 25% La, with small amounts of Nd.[13] If we can decide the ideal proportion of Mm (the best combination of each element) instead of the natural proportion, the TE performance could be improved for the system. In order to decide the combination of each element, it is important to investigate the filling effect of each element individually. Therefore, in Chapter 3, we first studied the effect of Cerium (Ce) filled skutterudite under high pressure. The results have confirmed that the high filling rate markedly decreased the lattice thermal conductivity. Furthermore, the result show that Ce ions can be used to fill skutterudites with better TE performances than $CoSb_3$. Then, this section describes the characterization techniques on the samples in term of phases structures, lattice parameter, actual compositions, and thermoelectric properties of $Ce_xCo_4Sb_{12}$.

3.2 X-ray diffraction (XRD) of $Ce_xCo_4Sb_{12}$

Crystalline degree and phase purity of the products were analyzed by X-ray diffractometer (XRD) with Cu Kαl radiation (λ = 0.154060 nm) operating at 40 kV- 40 mA, in the 2θ range of 10° - 160°. The products were specified by a Rigaku RINT-RAPID-II Computer Software (search match program) of the JCPDS database.

Skutterudites of the form $Ce_xCo_4Sb_{12}$ were filled with varying fractions (x = 0.2 - 1.0) using high pressure (4 GPa), heating to 900°C for two minutes, and then decreasing the temperature to 600°C for 120 minutes, the products were composed of $Ce_xCo_4Sb_{12}$ with some impurities. For x = 0.2, both Sb and $CoSb_2$ impurities were left and right in the main peak respectively. When the composition x was varying increase to 1.0, the impurity of Sb in the left in the main peak and the impurity of $CoSb_2$ in the right are increases, likely because the filling fraction limit (FFL) of Ce is excessed.

The sharp peaks indicated shift to lower 2θ of $Ce_xCo_4Sb_{12}$ compare to mother compound $CoSb_3$. The strongest intensity peak is at 2θ = 36.203 degrees whereas $CoSb_3$ the strongest intensity peak is at 2θ = 36.497 degrees and the main peak diffracts is (013) planes of the samples. Moreover, by using high pressure technique the main peaks diffract are split to two peaks by lower 2θ are indicated filled skutterudite phase and higher 2θ are indicated unfilled skutterudite at co-state were shown in x = 0.6 and 0.8.

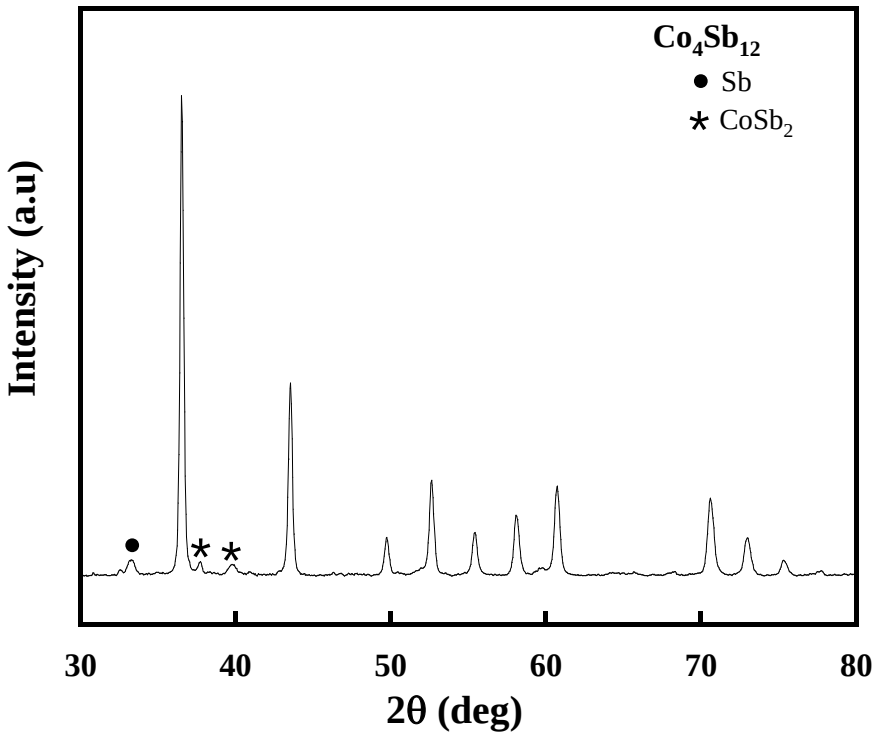

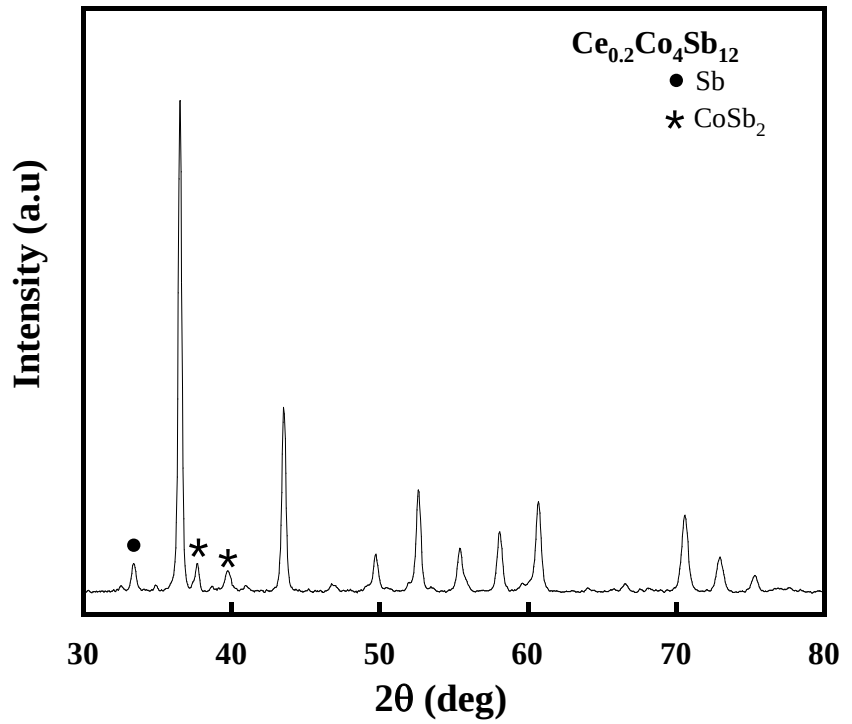
Ce0.2Co4Sb12
● Sb
∗ CoSb2
Intensity (a.u)
30
40
50
60
70
80
2θ (deg)

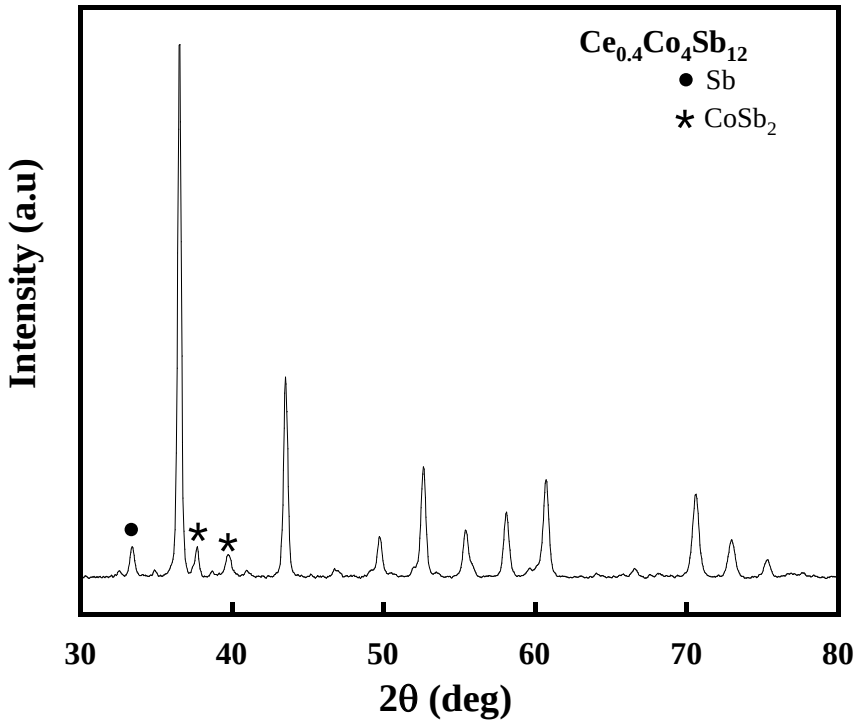
Ce0.4Co4Sb12
● Sb
∗ CoSb2
Intensity (a.u)
30
40
50
60
70
80
2θ (deg)

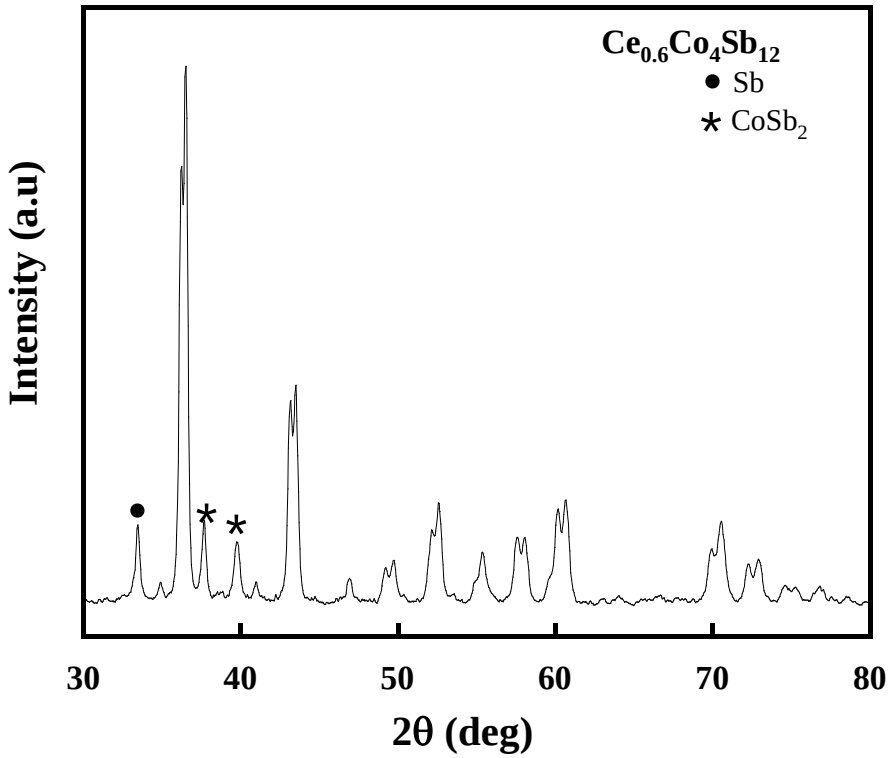
Ce0.6Co4Sb12
● Sb
∗ CoSb2
Intensity (a.u)
30
40
50
60
70
80
2θ (deg)

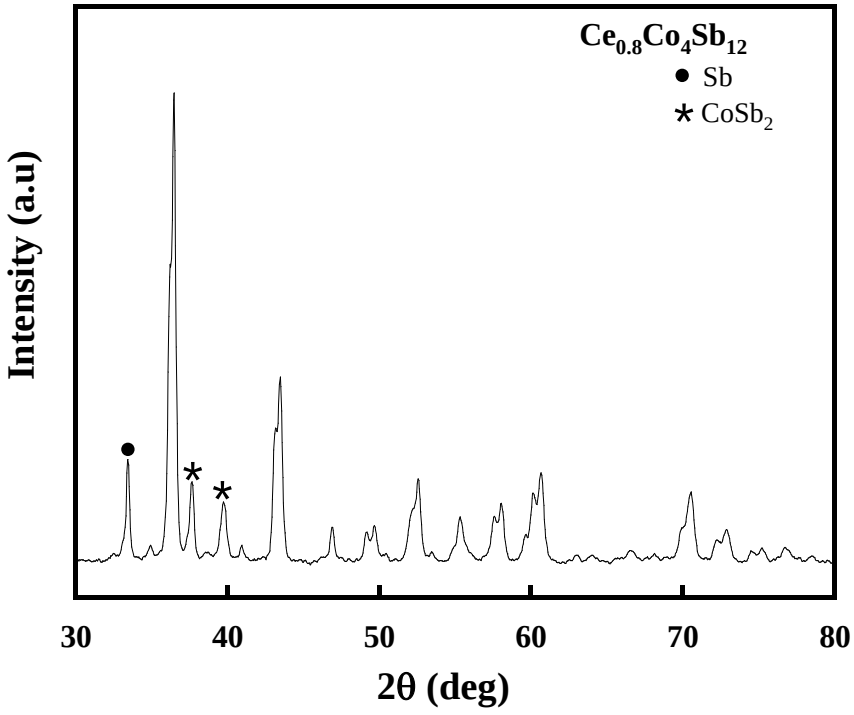
Ce0.8Co4Sb12
● Sb
∗ CoSb2
Intensity (a.u)
30
40
50
60
70
80
2θ (deg)

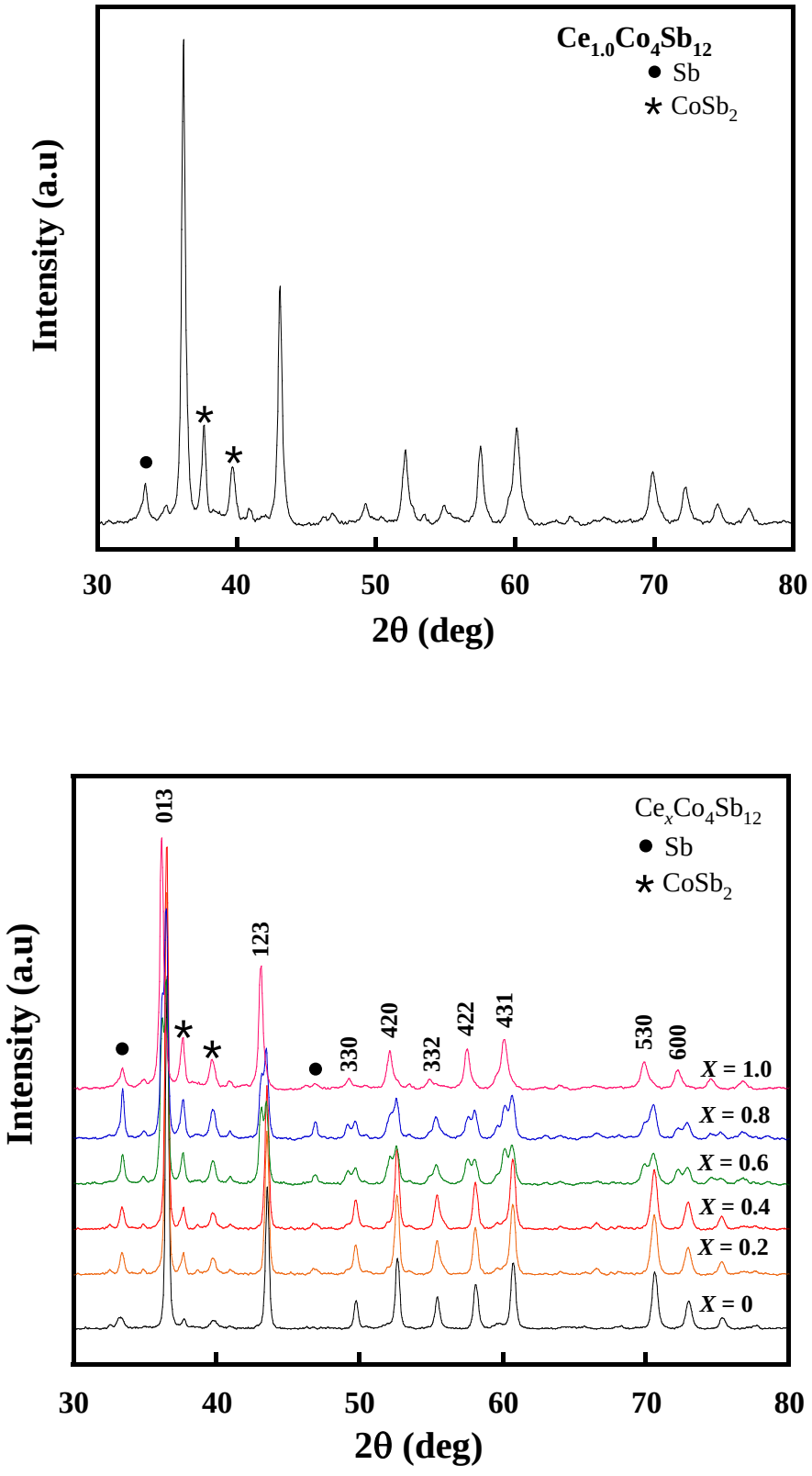

Figure 3-1. XRD pattern of a polycrystalline of $Ce_xCo_4Sb_{12}$.

3.3 Lattice constant and actual composition of $Ce_xCo_4Sb_{12}$

The lattice constant (a) for the samples was calculated using the least-squares fitting method as shown in Figure 3-2 (black line) indicates the effect of increased filling fraction on $Ce_xCo_4Sb_{12}$ compounds. As the Ce filling fraction increased, the lattice constant increases. The lattice constant increased sharply up to 9.120 angstroms with increasing nominal filling of *x* and then remains unchanged. This is the highest value reported for any synthesis method of $Ce_xCo_4Sb_{12}$ demonstrating that the Ce was filling the Sb voids. [21,22] The point analysis of SEM and EDS were used to determine the actual compound composition. Comparing the atomic ratio, it was found that the average composition of the point analysis (red line) the actual filling fraction is lower than the nominal Ce doping rate. The actual filled fraction was found to be 0.37, the highest value reported for any $Ce_xCo_4Sb_{12}$ this might be due to the use of the high pressure, high temperature method.

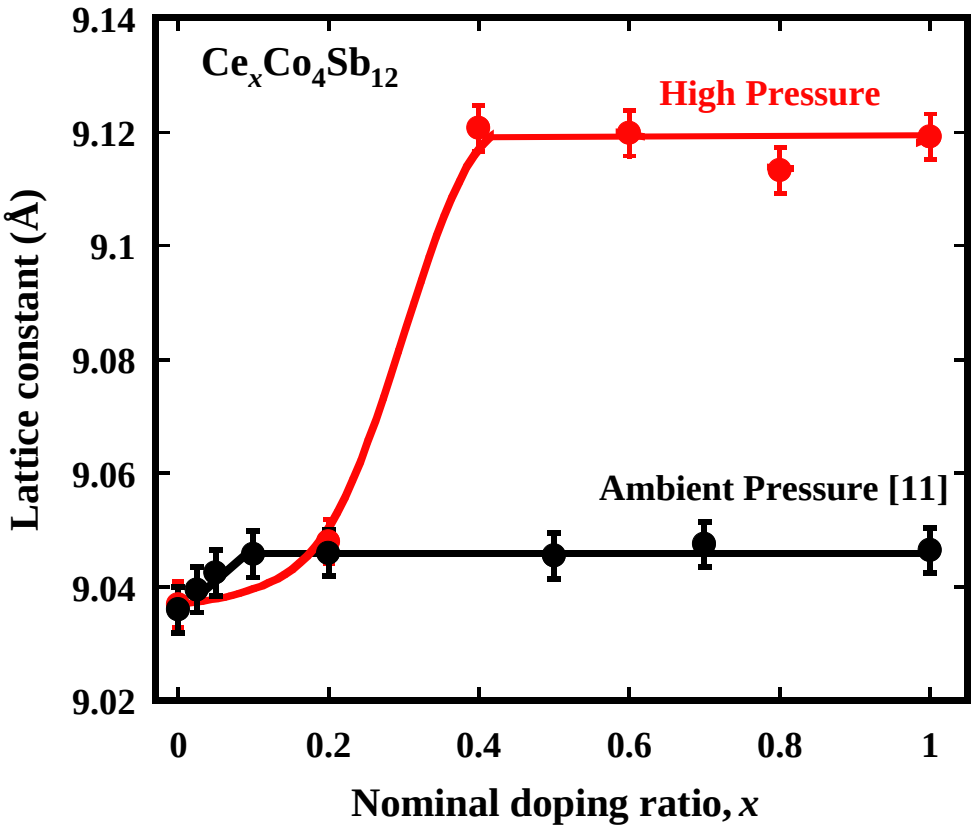

Figure 3-2. Lattice constant and actual Ce filling fraction vs nominal Ce doping rate.

3.4 The electrical resistivity of $Ce_xCo_4Sb_{12}$

The temperature dependence of the electrical properties of the $Ce_xCo_4Sb_{12}$ samples is shown in Figure 3-3. it was found that expected that addition of each atom of cerium to $CoSb_3$ unit cell would contribute additional electrons to the conduction band and lead to n-type metallic behavior. The electrical resistivity (ρ) exhibited a small semimetal-like behavior; small increased with temperature in the whole temperature range and reached a maximum at 300 K. This seems to indicate incomplete of the filling ions, contributing fewer conduction electrons than expected.

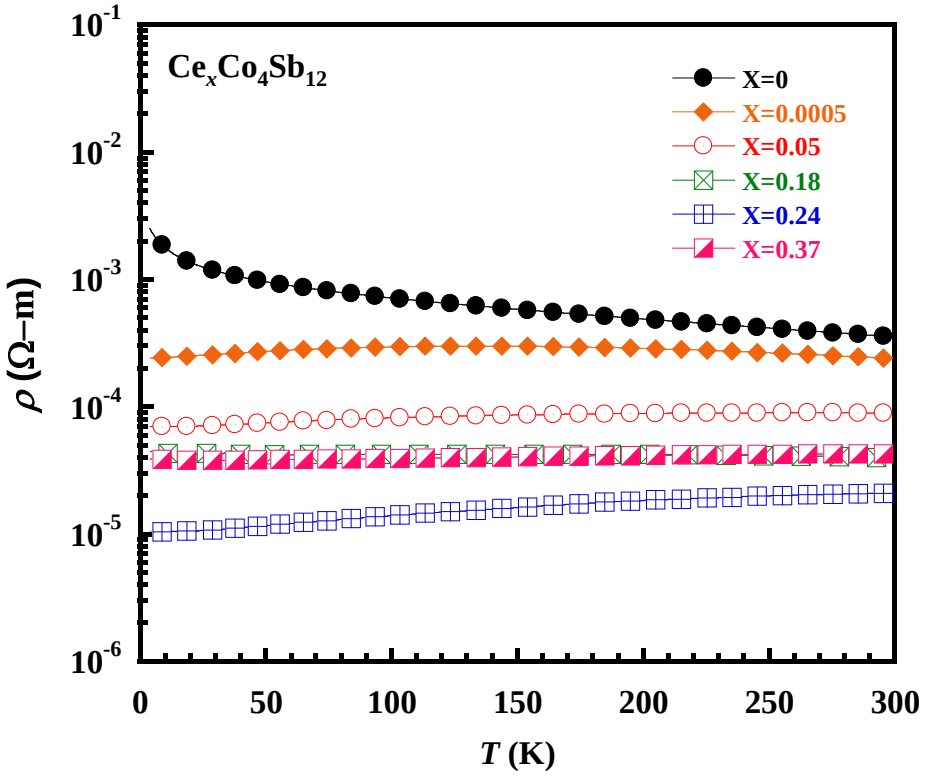

Figure 3-3. Temperature dependences of the electrical resistivity of $Ce_xCo_4Sb_{12}$.

3.5 The thermal transport property of $Ce_xCo_4Sb_{12}$

The temperature dependence of the thermal conductivity (κ) of $Ce_xCo_4Sb_{12}$ is shown in Figure 3-4. The κ values of sample were quite high like metals, and a little bit decreased with temperature increasing this might be due to the boundary scattering. $CoSb_3$ presented the higher κ values than $Ce_xCo_4Sb_{12}$, because of the rattling behaviors are scattering phonon heat. The lattice thermal conductivity κ_l was obtained by subtracting the electronic thermal conductivity κ_l from the total measured thermal conductivity κ. The value of κ_e was calculated using $\kappa_e = L\sigma T$, where σ is the electrical conductivity ($\sigma = 1/\rho$) and L is the Lorentz number ($L = 2.45\times10^{-8}$ $W\Omega K^{-2}$).[15] The lowest value at room temperature values of the κ_l for $Ce_xCo_4Sb_{12}$ were 3.12 $Wm^{-1}K^{-1}$ for $Ce_{0.37}Co_4Sb_{12}$. The significant decrease the

lattice thermal conductivity due to the mass fluctuation effect or the rattling effect or boundary scattering so that the total thermal conductivity is much lower than that of the samples without Ce guest ions [17] as shown in Fig. 3-4 and 3-5.

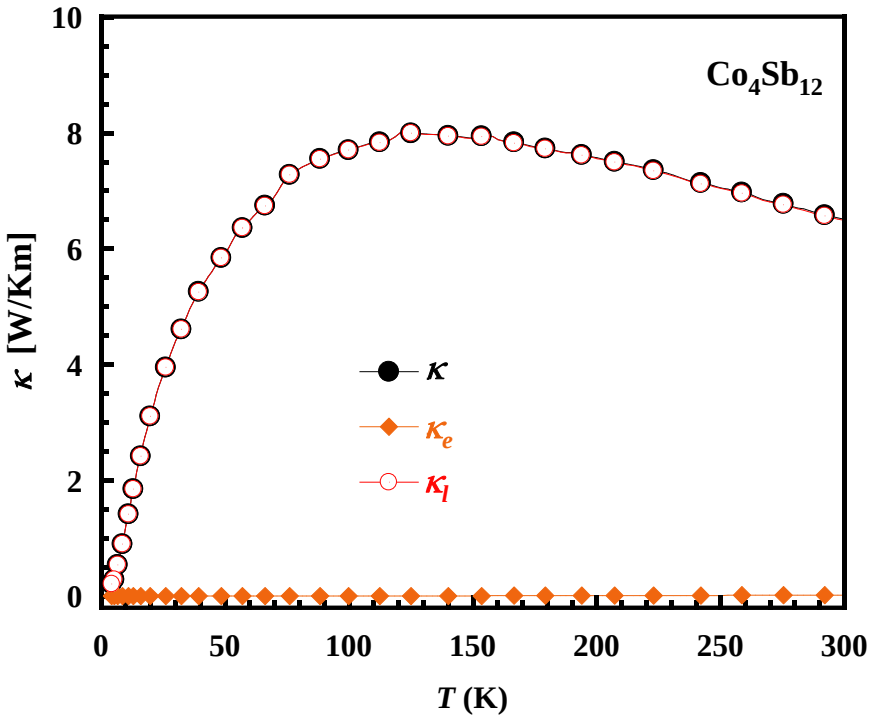

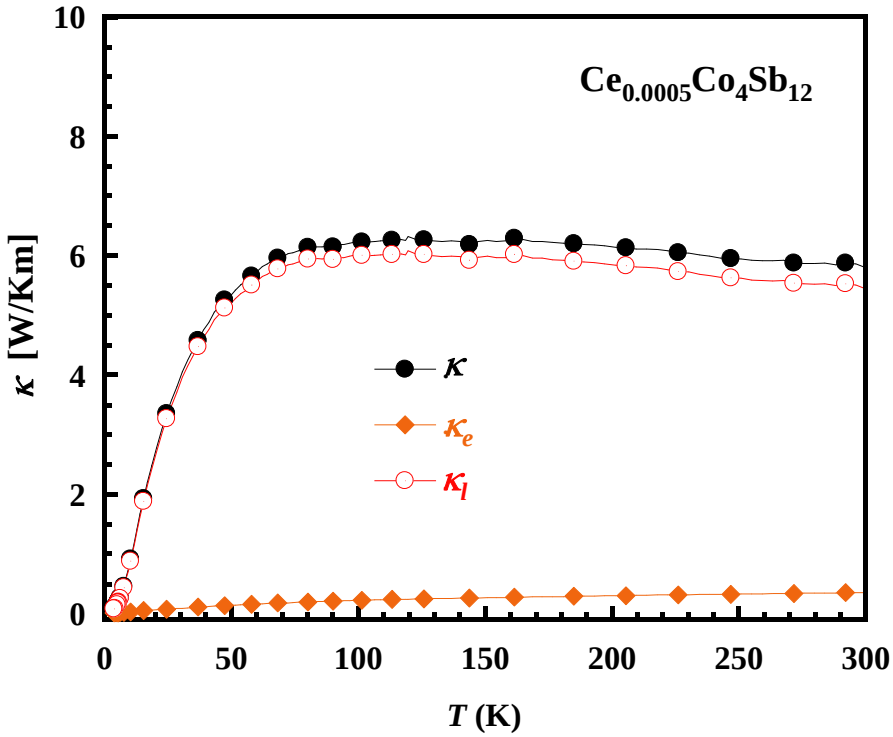
Ce0.0005Co4Sb12
κ [W/Km]
T (K)
κ
κe
κl
0
2
4
6
8
10
0
50
100
150
200
250
300

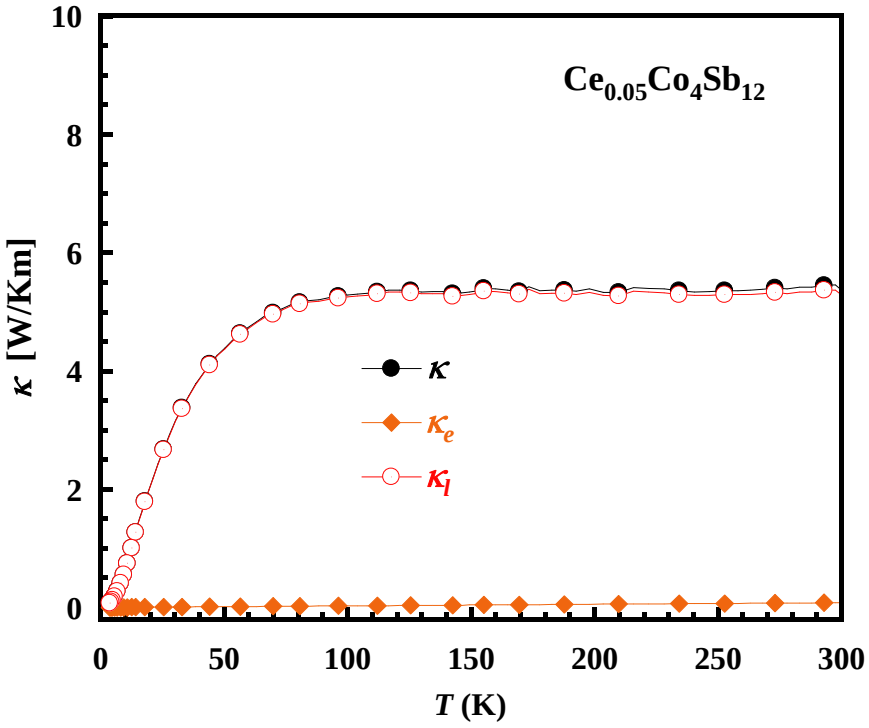
Ce0.05Co4Sb12
κ [W/Km]
T (K)
κ
κe
κl
0
2
4
6
8
10
0
50
100
150
200
250
300

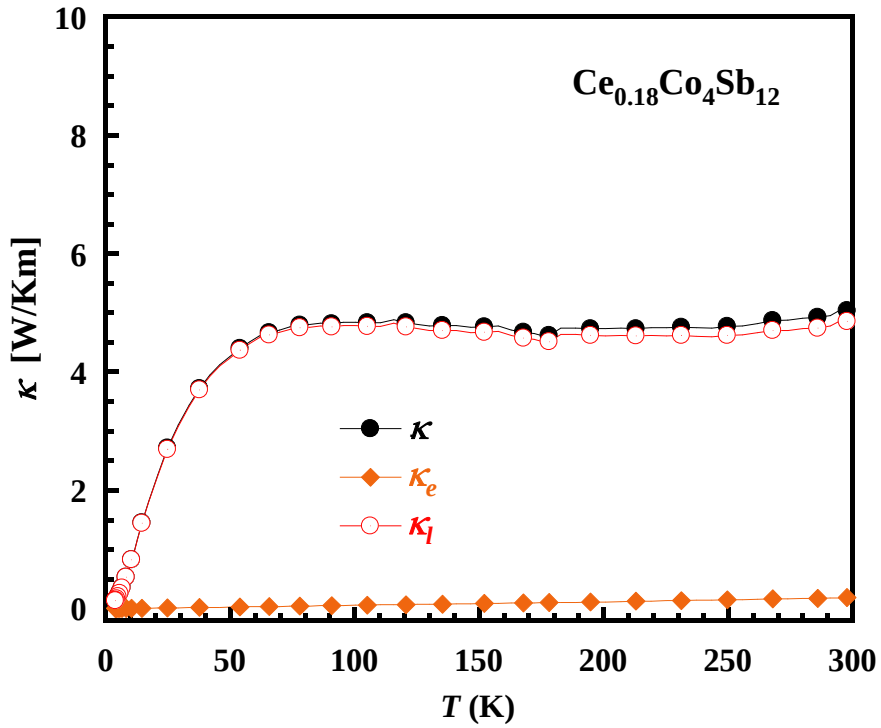
Ce0.18Co4Sb12
κ [W/Km]
T (K)
κ
κe
κl
0
2
4
6
8
10
0
50
100
150
200
250
300

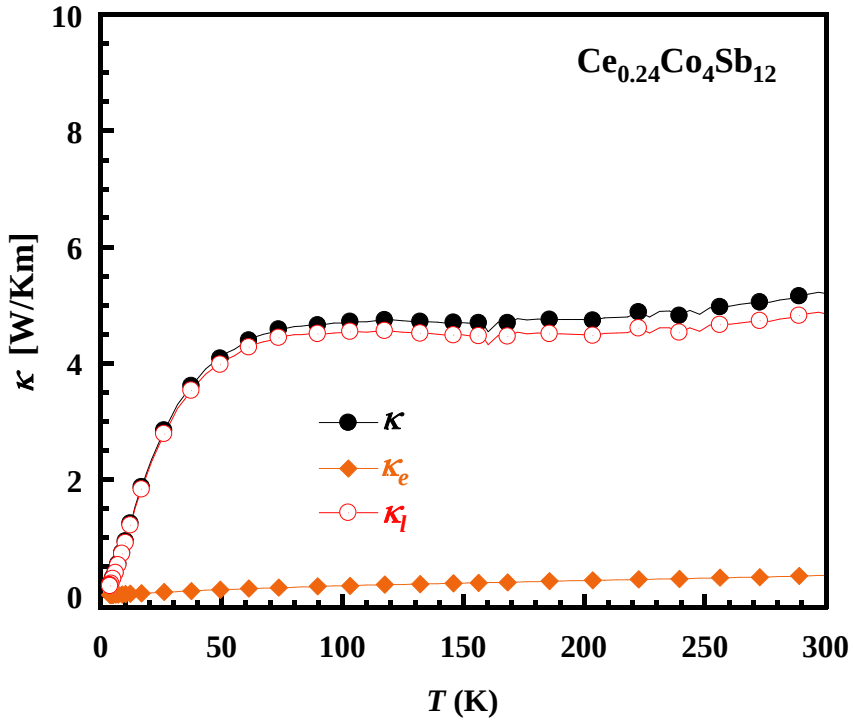
Ce0.24Co4Sb12
κ [W/Km]
T (K)
κ
κe
κl
0
2
4
6
8
10
0
50
100
150
200
250
300

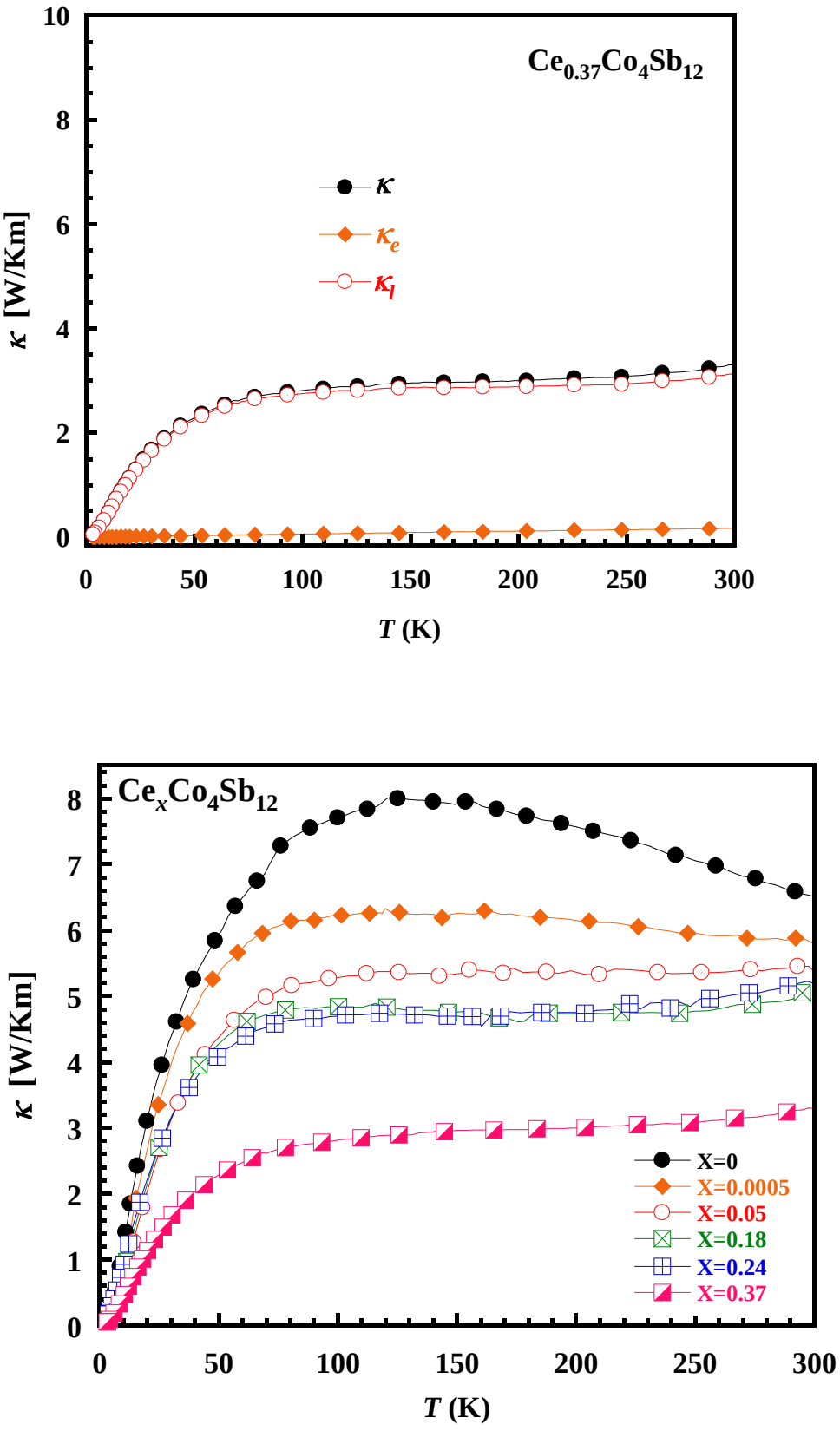

Figure 3-4. Temperature dependences of κ of $Ce_xCo_4Sb_{12}$.

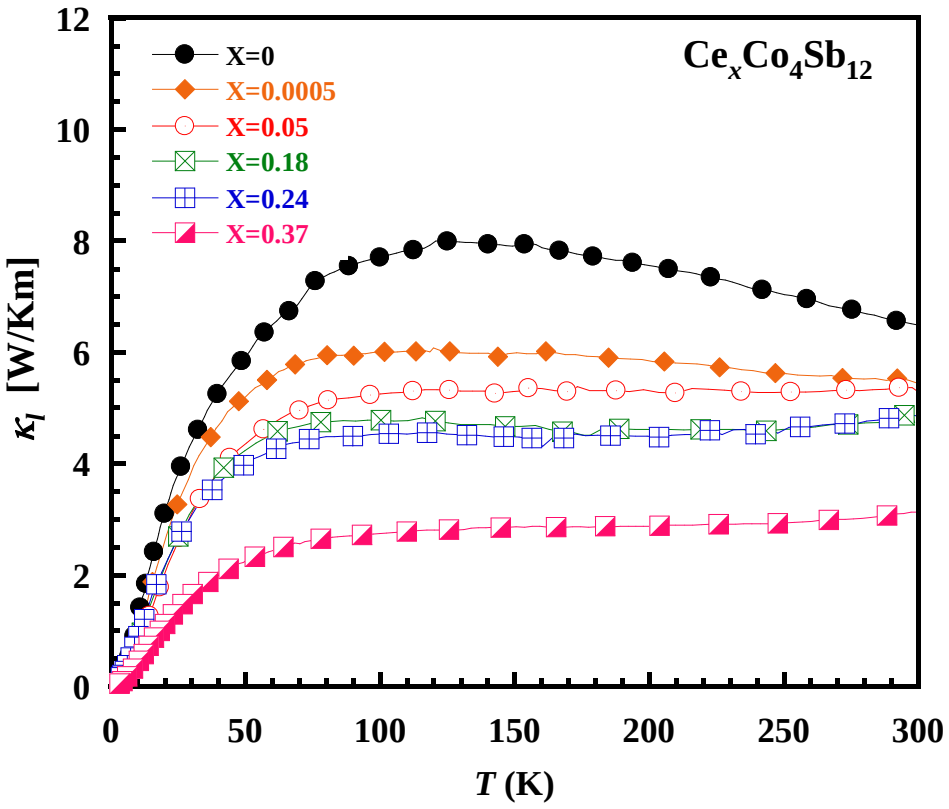

Figure 3-5. Temperature dependences of the lattice thermal conductivity of $Ce_xCo_4Sb_{12}$.

3.6 The Seebeck coefficient and *ZT* value of $Ce_xCo_4Sb_{12}$

The negative seebeck coefficients (*S*) (Fig. 3-6) indicate that electrons are the main carriers. Sample of $CoSb_3$ indicates an intrinsic semiconductor with positive value, whereas Ce-doped samples decrease gradually as Ce-doping increased. The absolute values of *S* with Ce-doping reach a maximum value of 0.37 with *S* = -53 μV/K at 300 K. This behavior corresponds with the change of the carrier concentration from hole to electrons. The conductor changes from p-type to n-type conductor by receiving donated electrons from Ce-doping, consistent with the electrical resistivity decrease with increasing *x*. This behavior due to the increase in the electron concentration. The result of large decrease κ

combine with S and ρ which leads to the highest observed ZT value among all the samples studied were shown in fig.3-7.

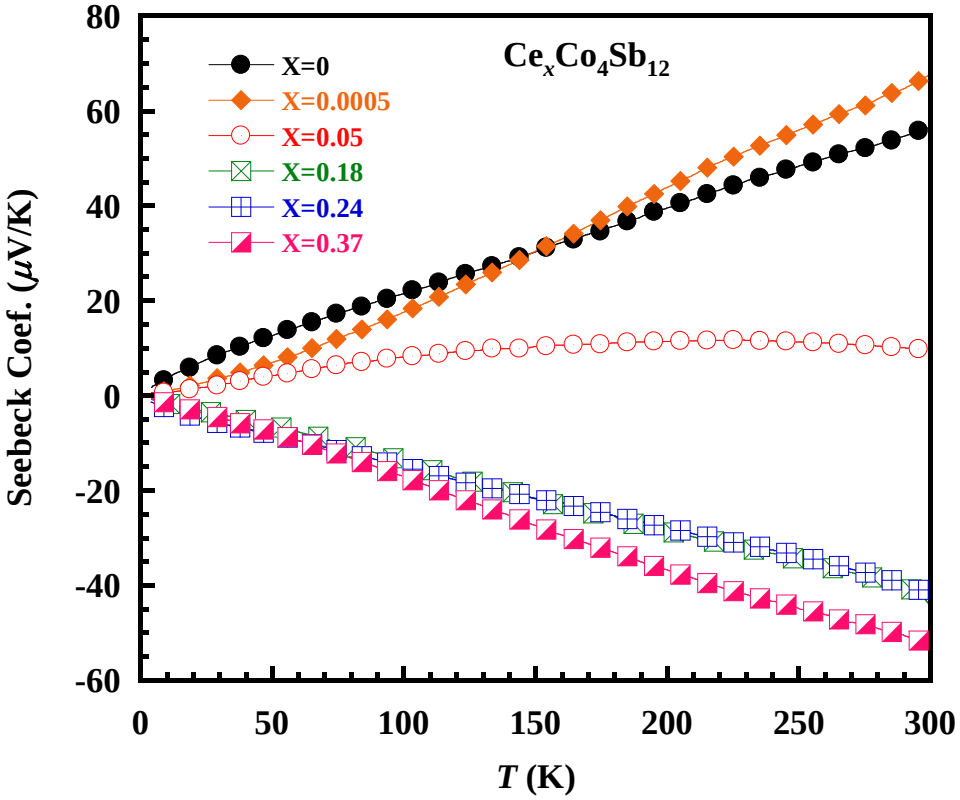

Figure 3-6. Temperature dependences of the Seebeck coefficient of $Ce_xCo_4Sb_{12}$.

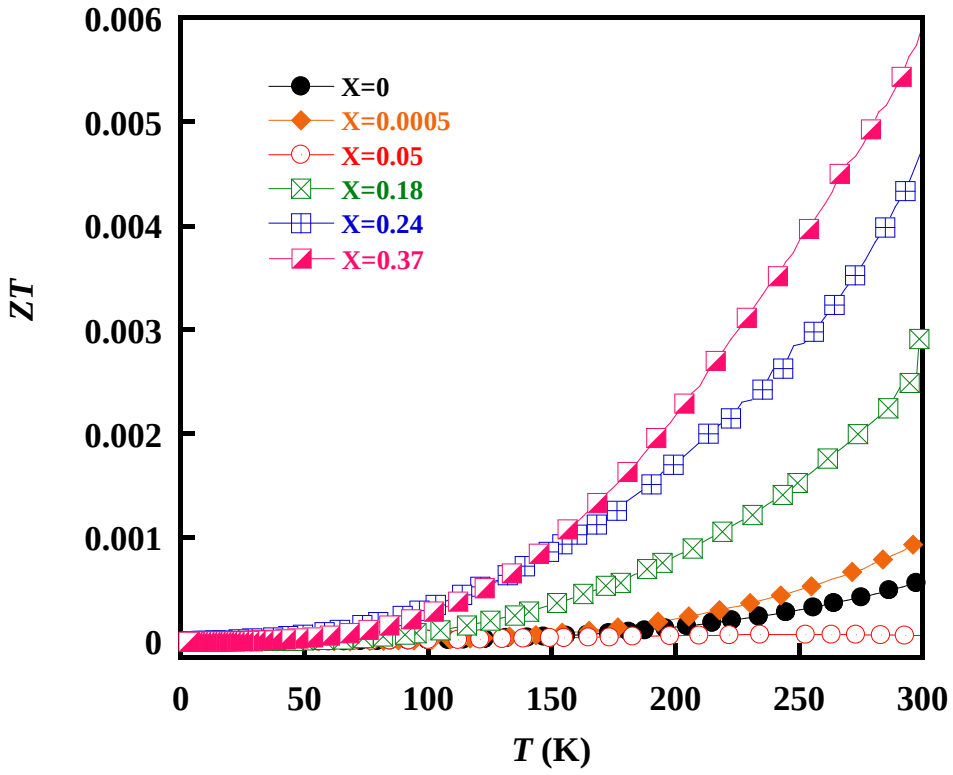

Figure 3-7. Temperature dependences of *ZT* value of $Ce_xCo_4Sb_{12}$.

3.7 Summary

In summary, a high-pressure synthesis technique has been demonstrated to produce TE materials with a high filling rate, the high filling fraction has produced an enhancement of thermoelectric properties. The experimental process was used high pressure at 4 GPa to synthesize a bulk sample. XRD diffraction results indicate that only small amount impurity of Sb and $CoSb_2$ were detected. Samples of nominal composition $Ce_xCo_4Sb_{12}$ (x = 0 – 1.0) started material made through the high-pressure and high temperature synthesis. The increased Ce concentration in this study not only enhance the electric transport due to a better electron doping effect but also decrease the thermal conductivity due to a stronger rattling effect. The highest actual composition of Ce filled $CoSb_3$-based skutterudite of 0.37, and was found to be optimal for achieving a peak *ZT* value of about 0.006 at 300 K.

Chapter 4
Experimental Results of $Nd_xCo_4Sb_{12}$

4.1 Introduction

In chapter 4, we have studied the effect of a a few percent of neodymium (Nd) in filling Mm skutterudites under high pressure. The results have confirmed the high filling rate is markedly decreased the lattice thermal conductivity than Ce filled skutterudite with studied in chapter 3. This is may be due to the distribution of fillers ions. Therefore, this chapter will discuss the detailed experimental result data of the $Nd_xCo_4Sb_{12}$ samples in term of phases structures, lattice parameter, actual compositions, and thermoelectric properties of $Nd_xCo_4Sb_{12}$.

4.2 X-ray diffraction (XRD) of $Nd_xCo_4Sb_{12}$

The XRD patterns of $Nd_xCo_4Sb_{12}$ (x = 0 - 1.0) samples are shown below, respectively. The diffraction peaks of all samples can be indexed as the $Nd_xCo_4Sb_{12}$ phase which has a skutterudite structure with the $Im\bar{3}$ space group. Crystalline degree and phase purity of the products were analyzed by X-ray diffractometer (XRD) with Cu Kαl radiation (λ = 0.154060 nm) operating at 40 kV- 40 mA, in the 2θ range of 10° - 160°. The products were specified by a Rigaku RINT-RAPID-II Computer Software (search match program) of the JCPDS database.

These studies show a small impurity of Sb and $CoSb_2$ amount of impurity of Sb and $CoSb_2$, by Nd increase the impurity of Sb is relatively low but $CoSb_2$ is reverted, and the x-ray study of Nd filled skutterudite gives a shift of lower 2θ compared to the unfilled samples x-ray study as shown in fig 4-1. When the filling fraction of Nd is lower than 0.6 (nominal composition), the reflection lines splits into two peaks in lower intensity, likely due to a quantity of Nd incomprehensive

all area of the samples and some area is unfilled producing a defective point in the samples. The smaller angle with increased filling fraction is very similar to some previous reports of filled skutterudite.[23–25)]

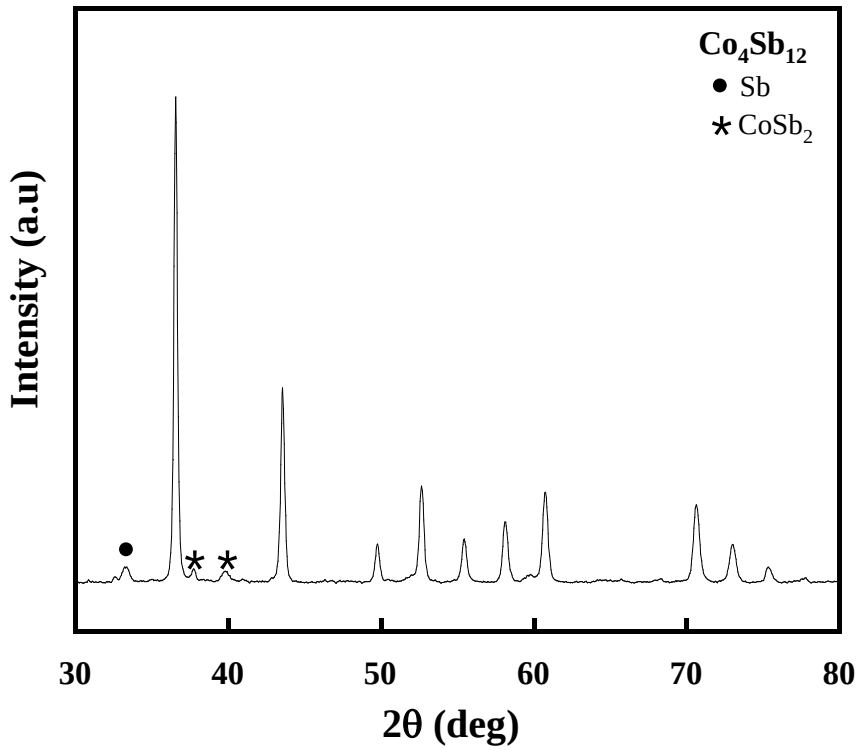

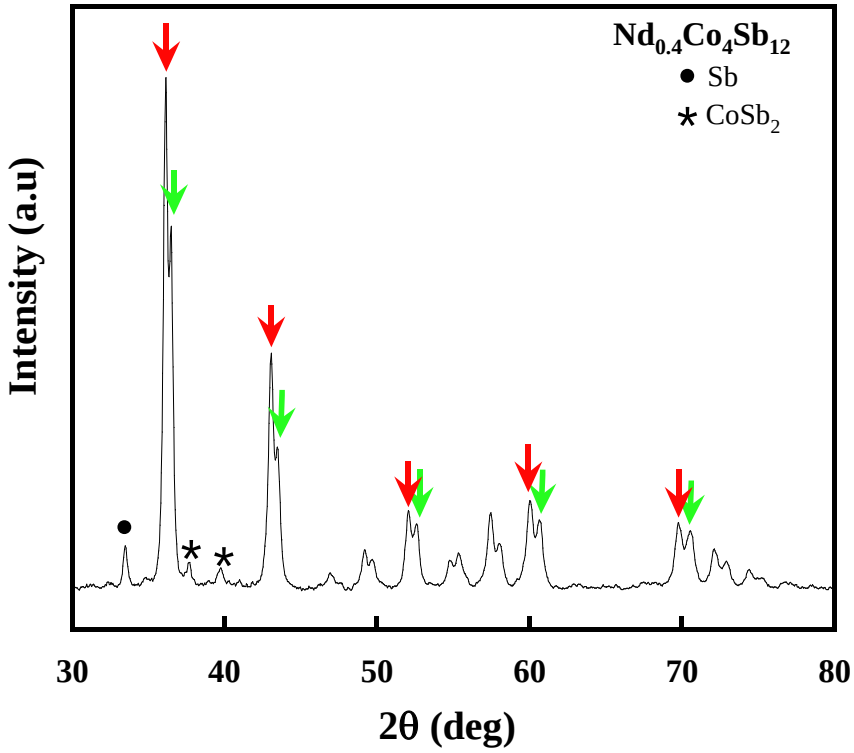
Nd0.4Co4Sb12
● Sb
∗ CoSb2
Intensity (a.u)
30
40
50
60
70
80
2θ (deg)

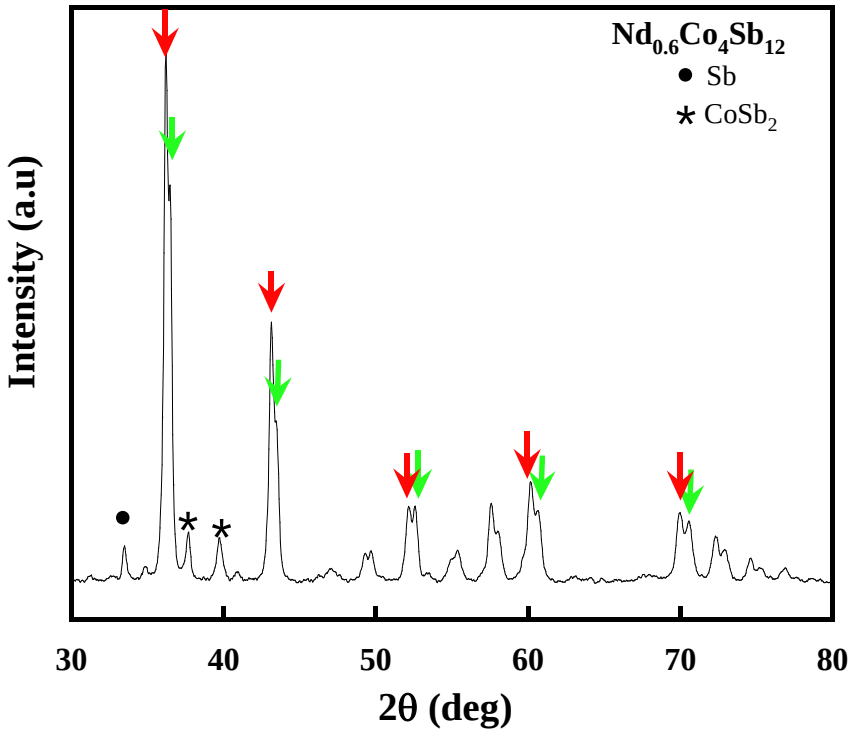
Nd0.6Co4Sb12
● Sb
∗ CoSb2
Intensity (a.u)
30
40
50
60
70
80
2θ (deg)

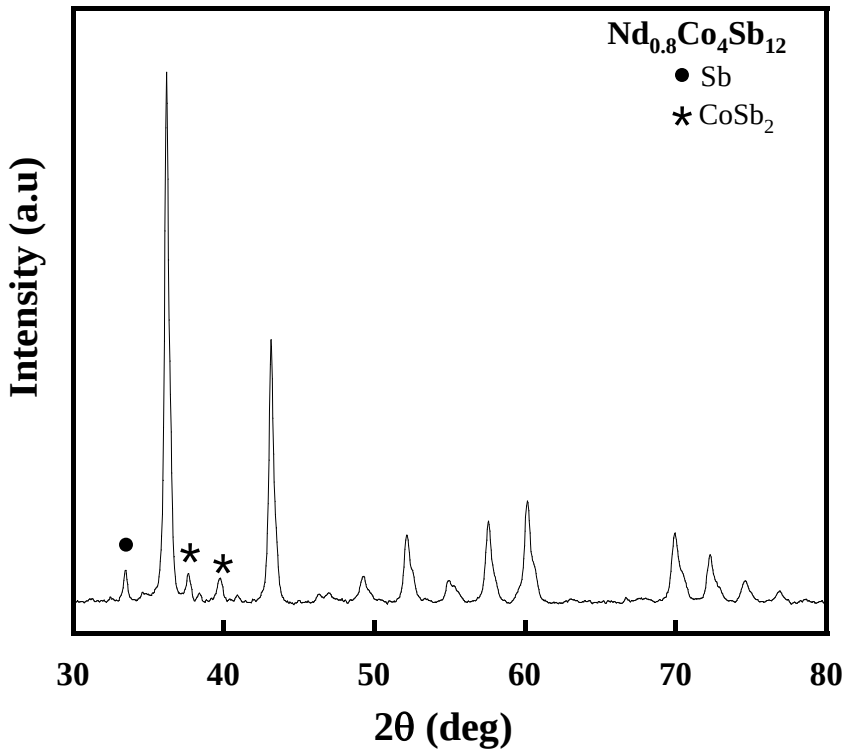
Nd0.8Co4Sb12
Sb
CoSb2
Intensity (a.u)
30
40
50
60
70
80
2θ (deg)

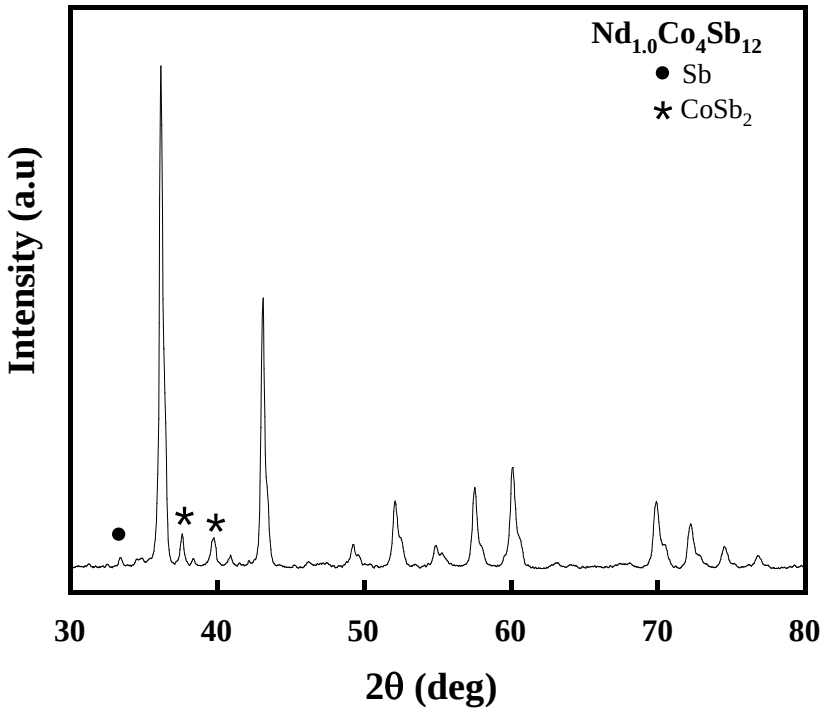
Nd1.0Co4Sb12
Sb
CoSb2
Intensity (a.u)
30
40
50
60
70
80
2θ (deg)

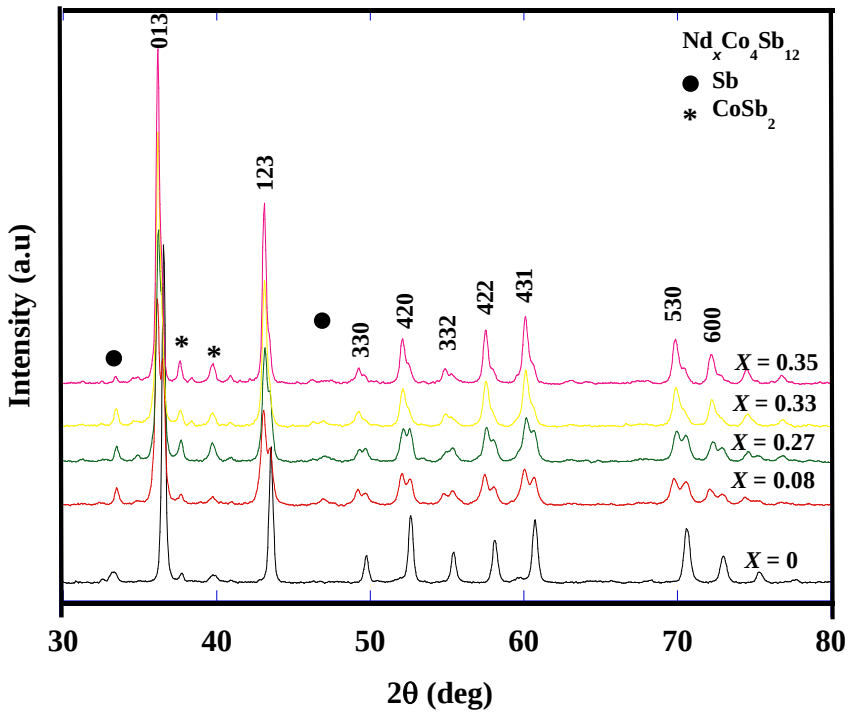

Figure 4-1. XRD pattern of a polycrystalline of $Nd_xCo_4Sb_{12}$.

4.3 Lattice constant and actual composition of $Nd_xCo_4Sb_{12}$

The lattice parameter with a small filled Nd has rapidly increased to 9.10 Å and saturated although Nd doping rate was increased (shown in fig 4-2). The actual compositions were evaluated by SEM and EDX. The SEM examination of $Nd_xCo_4Sb_{12}$ samples indicates a dense structure with closely packed grains. The EDX has been used to examine the actual composition by point analysis, by comparing the atomic ratio. The actual filling fraction of Nd in $Nd_xCo_4Sb_{12}$ is lower than the nominal Nd doping ratio as shown in fig 4-2. The maximum Nd value obtained is 0.35, higher than $Nd_{0.1}Co_4Sb_{12}$ and $Nd_{0.13}Co_4Sb_{12}$ were reported.[26,27] The calculated lattice parameter from the XRD measurement is shown in fig 4-2 (red line).

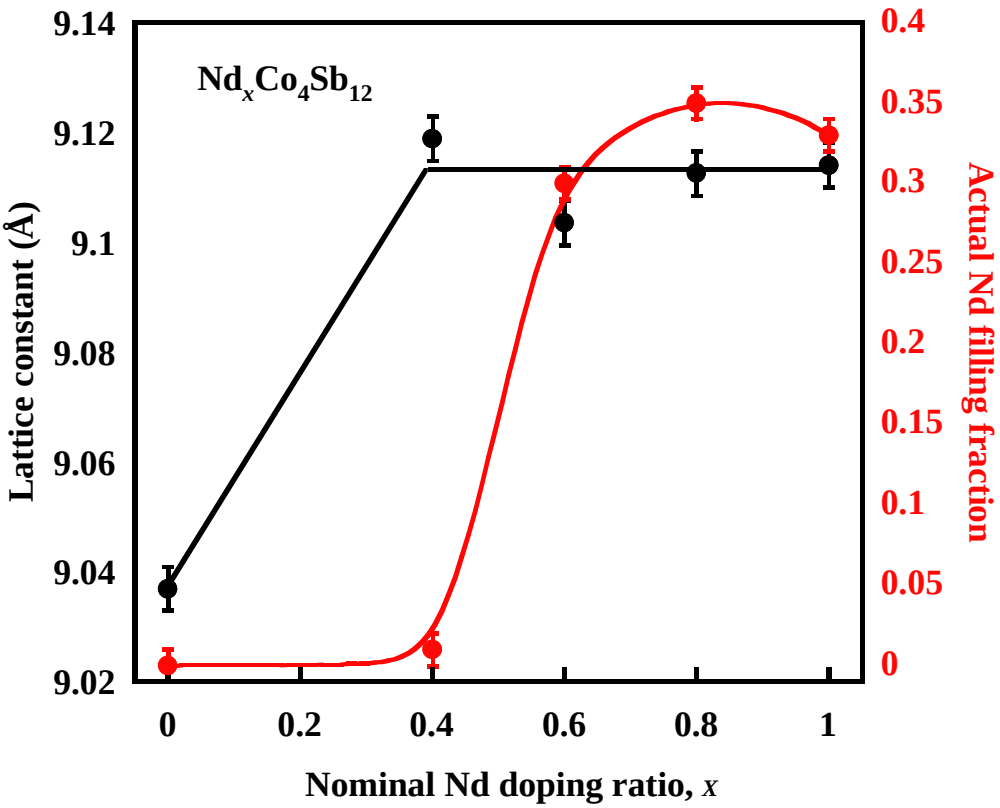

Figure 4-2. Lattice constant and actual Nd filling fraction vs nominal Nd doping rate.

4.4 The electrical resistivity (ρ) of $Nd_xCo_4Sb_{12}$

Temperature dependence of the electrical resistivity were shown in fig 4-3. The electrical conductivity (σ) or electrical resistivity (ρ) of materials relates to charge carrier concentration (n), electric charge (e), and electron mobility (μ) by $\sigma = 1/\rho = ne\mu$ by higher level of charge carrier concentration significantly increases electrical conductivity of material. In general, the charge carrier can be divided into two types; a hole and an electron which are dominant in p- and n-type semiconductors, respectively. In this study, the ρ of unfilled skutterudite decreased with the increasing temperature and shows p type semiconductor behavior in low temperature with large ρ. In contrast, samples doped with Nd

displayed semimetal behavior. The ρ decreases with elevating Nd filled in the voids and x = 0.33 and 0.35 exhibits almost the same value of ρ. This can be attributed to increased electron concentration by donating electron from Nd filled skutterudite. This might be samples having high electron concentration changes from p-type conductivity to n-type conductivity, according to some previous work on rare earth elemental filled skutterudites.[9,28)]

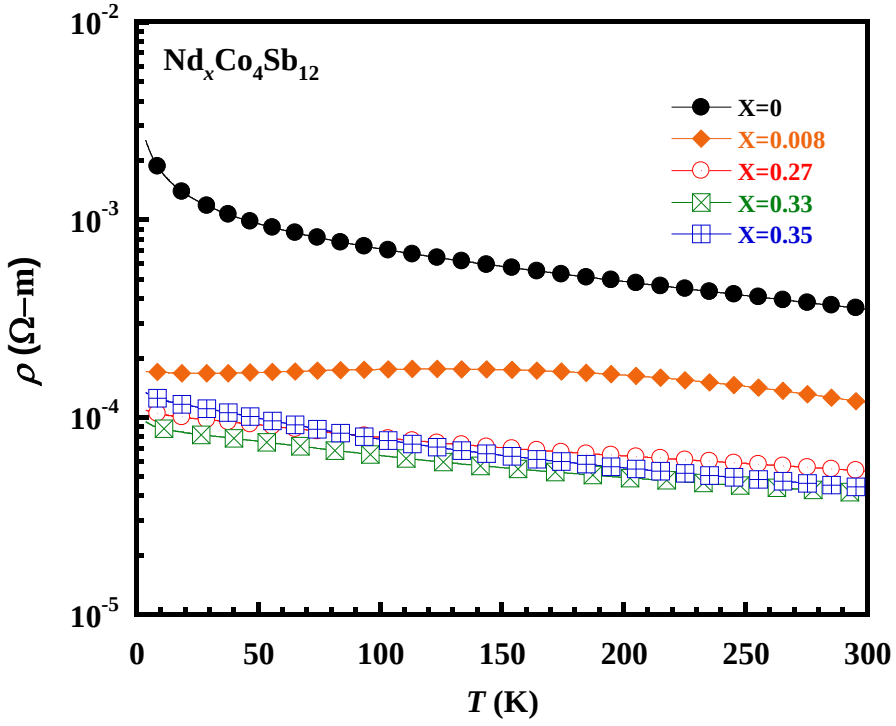

Figure 4-3. Temperature dependences of the electrical resistivity of $Nd_xCo_4Sb_{12}$.

4.5 The thermal transport property of $Nd_xCo_4Sb_{12}$

The ZT value can be further maximized by minimizing thermal conductivity. Filled skutterudite introduce the phonon scattering. Total thermal conductivity (κ) comes from two sources: electronic (κ_e) and lattice (κ_l) part. The κ_e is directly related to the electrical conductivity through the Wiedemann–Franz law which mention above. Fig. 4-4 shows the temperature dependence of lattice thermal conductivity κ_l in the temperature range from 5 K to 300 K for Nd filled

skutterudites and compared to the unfilled $CoSb_3$. The peak value for unfilled $CoSb_3$ in our study reaches 8 W/mK at 150 K and is suppressed a little to 6.49 W/mK at room temperature. This is due to the scattering of grain-boundary in polycrystalline of $CoSb_3$ as shown in fig 4-4. Filled Nd ions in the voids of $CoSb_3$ are reducing κ_l substantially. For the x = 0.09 and x = 0.27 skutterudite samples exhibits the same κ_l value even though the amount is different. This may be related to the Co-phase of Nd-filled and unfilled phase which is observed by the XRD reflections line (see Fig. 4-1). The κ_l of the samples with x value 0.33 exhibits the lowest value of κ_l of 2.49 W/mK. This is lower than Nd-filled $CoSb_3$ skutterudite at ambient pressure of 3.7 W/mK $Nd_{0.25}Co_4Sb_{12}$ and 3.4 W/mK of $Nd_{0.1}Co_4Sb_{12}$.[26,27] The markedly reduction of κ_l due to the rattle behaviors and the random distribution of Nd filled skutterudite demonstrating the more effective scattering of phonons by markedly decreased in κ_l as shown in fig 4-5.

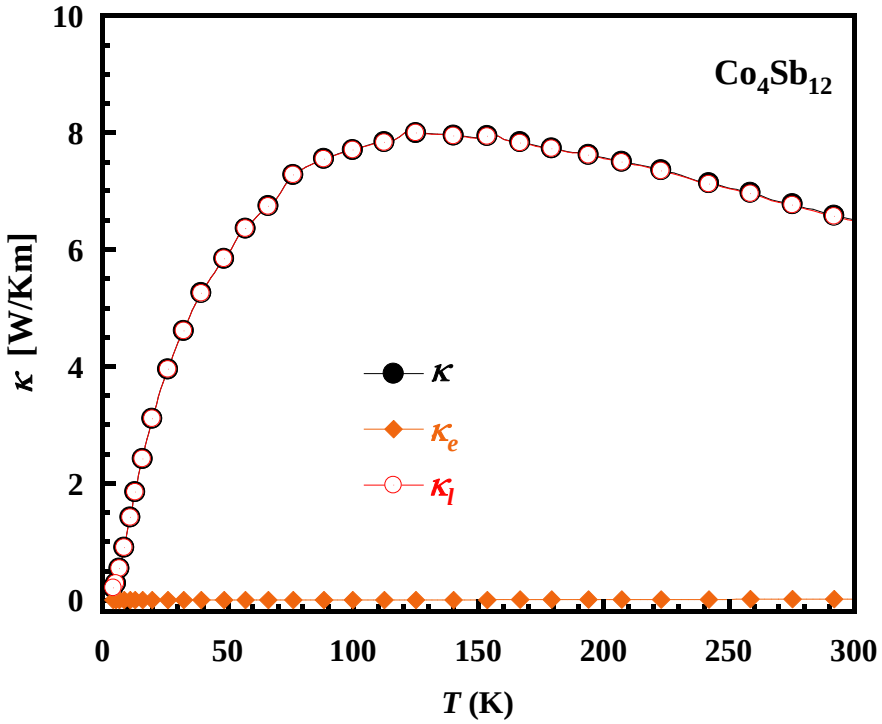

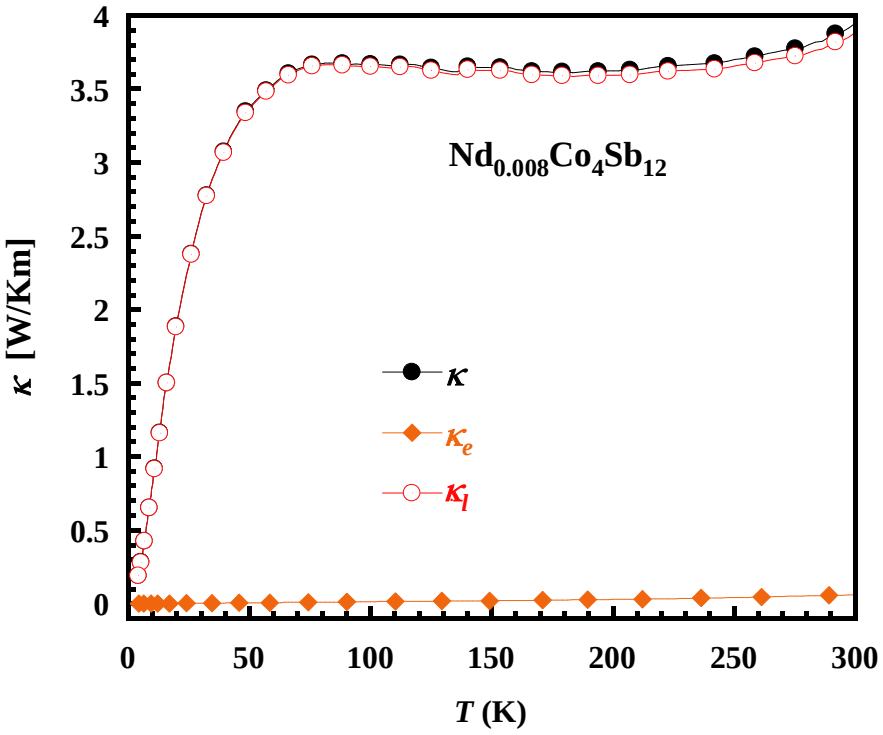
Nd0.008Co4Sb12
κ [W/Km]
T (K)
κ
κe
κl
0
0.5
1
1.5
2
2.5
3
3.5
4
0
50
100
150
200
250
300

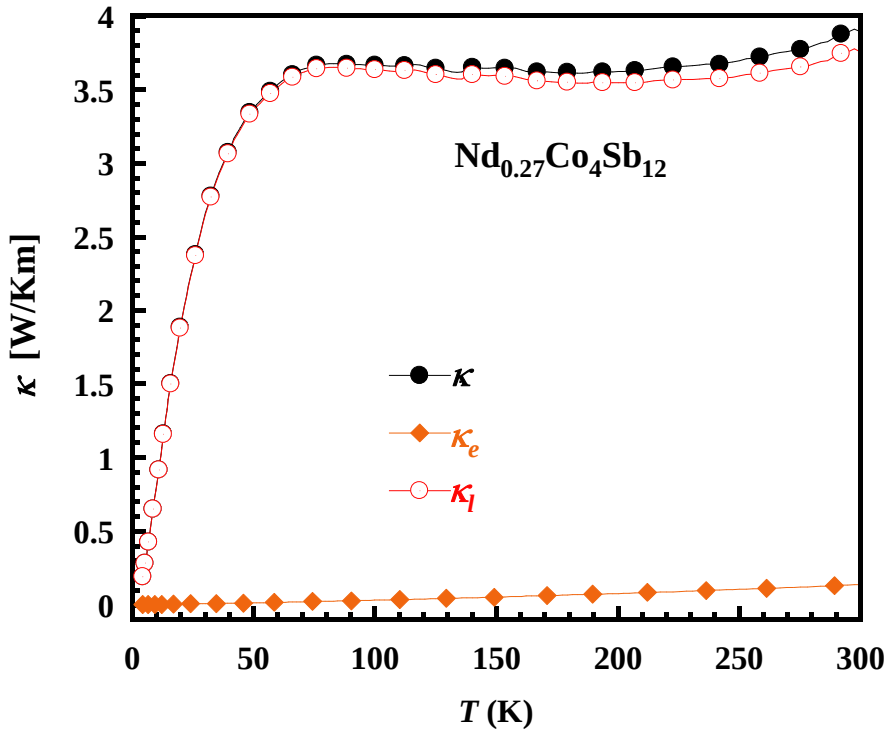
Nd0.27Co4Sb12
κ [W/Km]
T (K)
κ
κe
κl
0
0.5
1
1.5
2
2.5
3
3.5
4
0
50
100
150
200
250
300

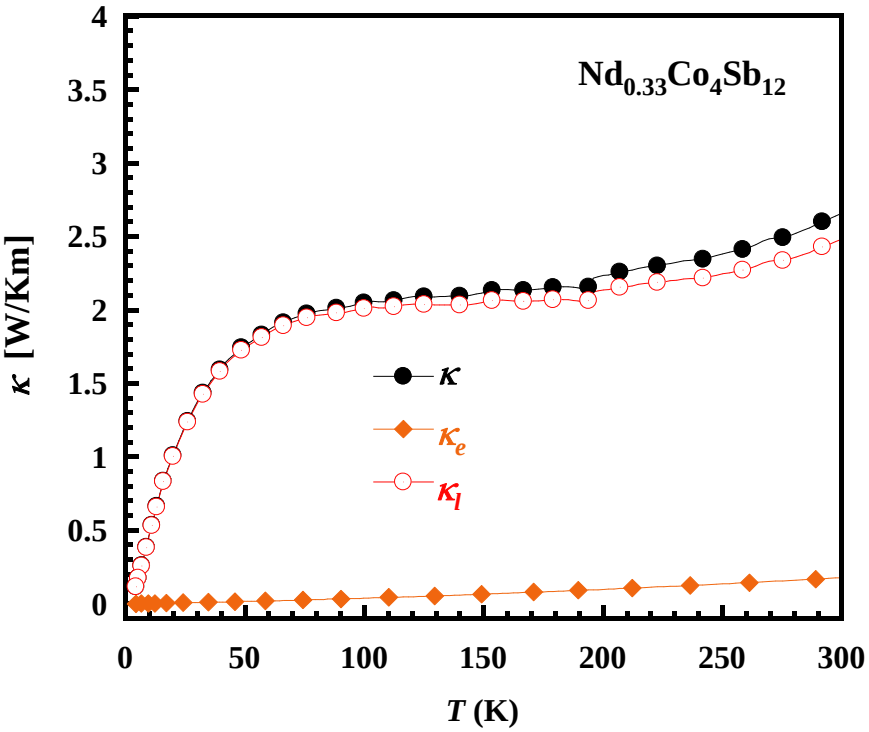
Nd0.33Co4Sb12
κ [W/Km]
T (K)
κ
κe
κl
0
0.5
1
1.5
2
2.5
3
3.5
4
0
50
100
150
200
250
300

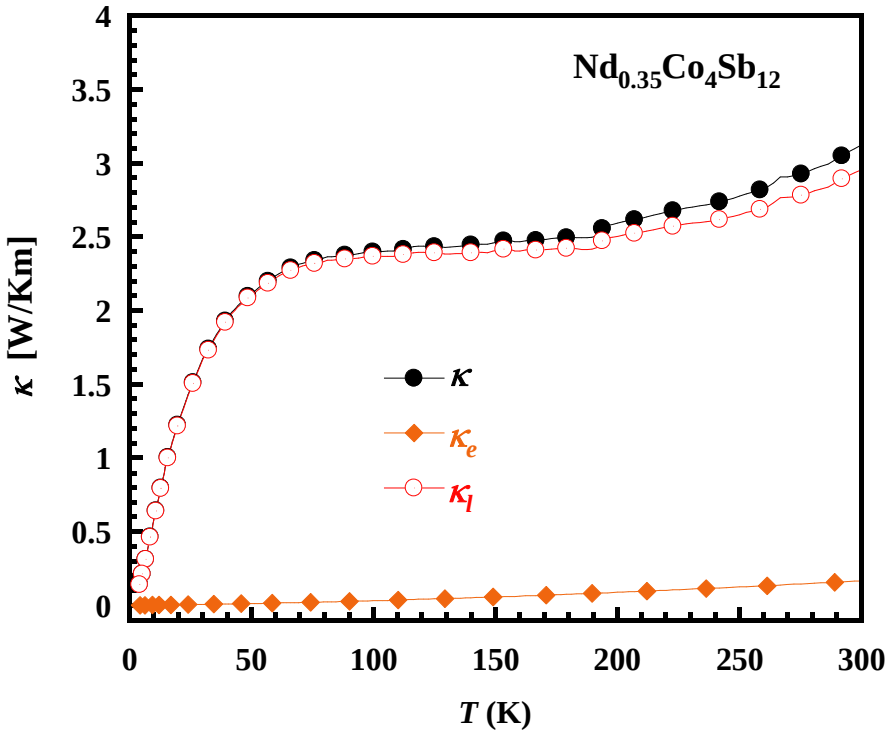
Nd0.35Co4Sb12
κ [W/Km]
T (K)
κ
κe
κl
0
0.5
1
1.5
2
2.5
3
3.5
4
0
50
100
150
200
250
300

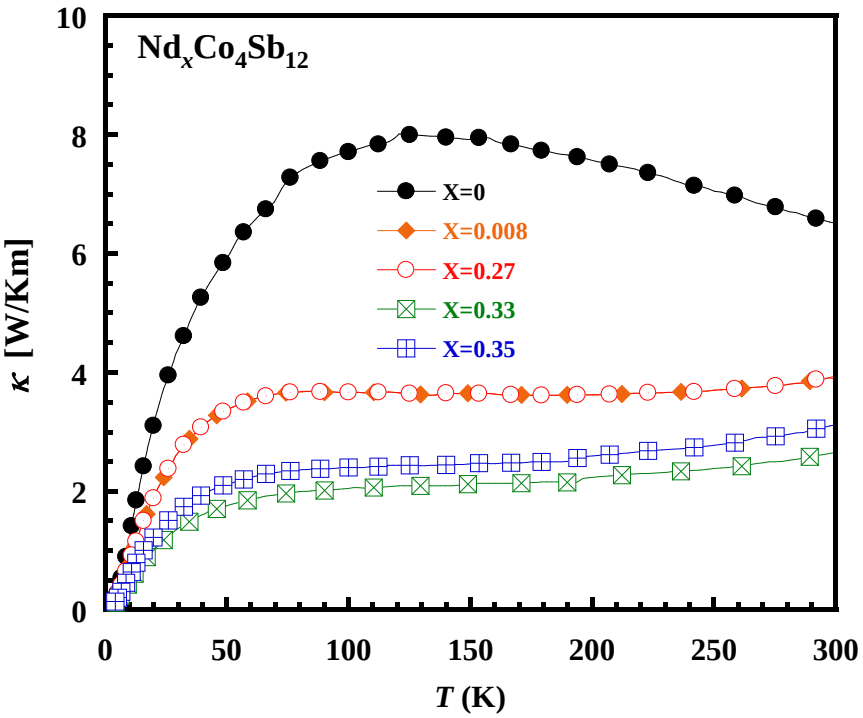

Figure 4-4. Temperature dependences of the thermal conductivity of $Nd_xCo_4Sb_{12}$.

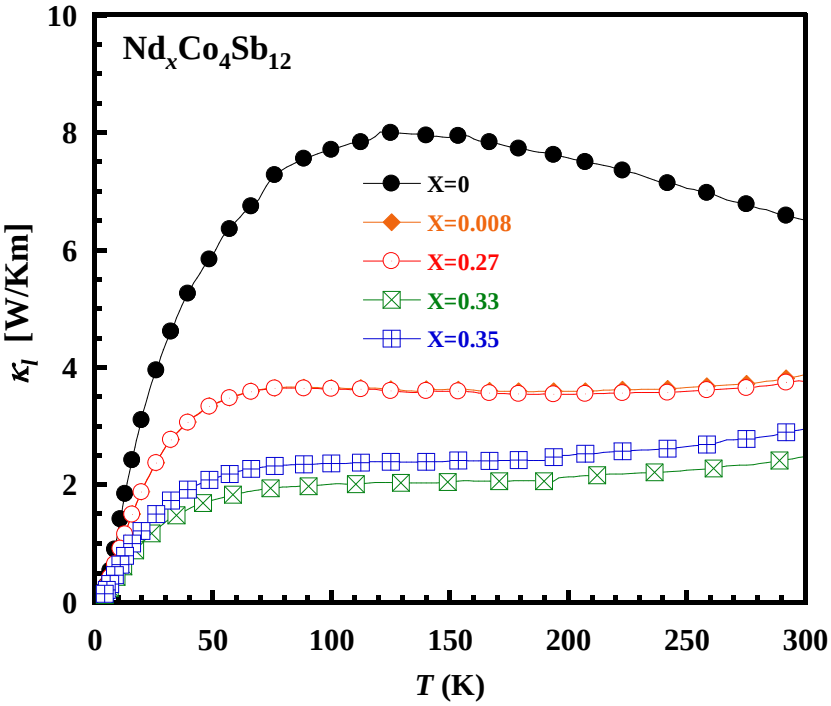

Figure 4-5. Temperature dependences of the lattice thermal conductivity of $Nd_xCo_4Sb_{12}$.

4.6 The seebeck coefficient and *ZT* value of $Nd_xCo_4Sb_{12}$

Regarding the temperature dependence of the Seebeck coefficient (*S*), as shown in fig 4-6, all samples of Nd filled skutterudites acquires negative Seebeck coefficients. It indicates the dominant carriers for the material's n-type conductivity are electrons, meaning that the negative change of *S* is related to the charge carrier concentration. Whereas the *S* of unfilled skutterudite is contrasted, it increases with the increasing temperature. Samples with different Nd filling rate shows a similar temperature dependence of *S* from 5 to 300 K, with the absolute value of *S* increasing to the maximum of -62.6 μVK^{-1} at 300K. The high doping of Nd clearly affects the *S* properties, however Nd filling up to 0.35 the S is conversely lower than those of the $x = 0.33$. It is noteworthy, if high filling of x=0.35 has more efficient, their *S* should be larger than the sample with $x = 0.33$, which the ratio is contrast in our experiment observed. One possible reason is that the sample with $x = 0.35$, over-electron concentration may contribute to the electrical conduction and then results of *S* is decrease. Moreover, $x = 0.08$ and 0.27 show the same value of *S* although the filling rate differs. This is due to the co-state of filled and unfilled of Nd, probably due to a quantity of Nd incomprehensive all area of the sample and some area is unfilled produced a defective point in the samples, observed in fig 4-1. The *ZT* value is estimated from the measured thermoelectric properties. In the experimental samples, the actual filling of Nd slightly increases with increasing Nd doping, which can be attributed to increases in the electron concentration. The *ZT* values increase with increased temperature. In this experiment, an optimal *ZT* figure of 0.011 at 300K was reached at $x = 0.33$. With filling fractions higher than 0.33, the *ZT* performance decreased due to a lower Seebeck coefficient and low carrier mobility. Therefore, tuning the carrier concentration and finding the effective mass of guest ions to reduce thermal conductivity are important for the enhancement of the *ZT* value.

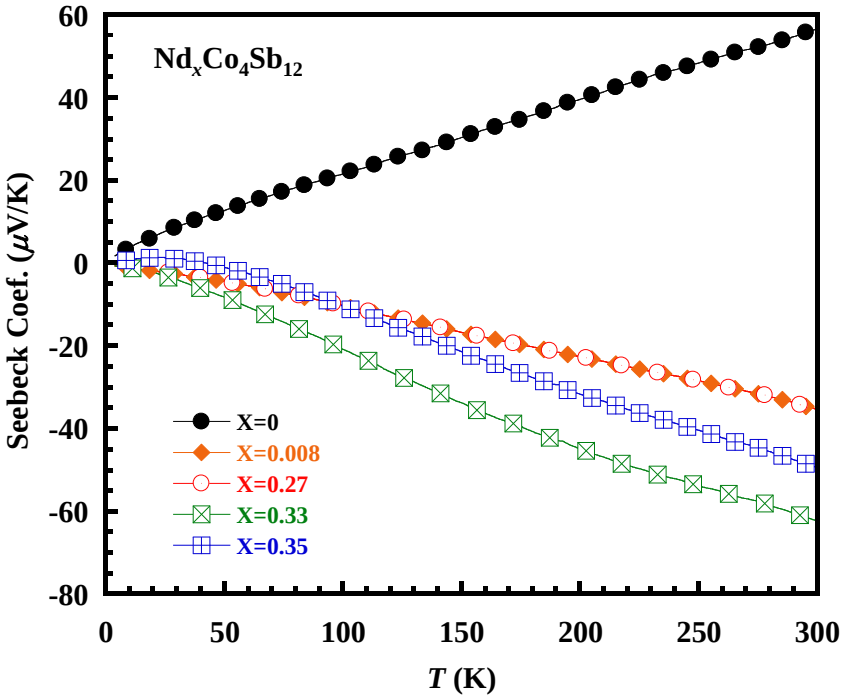

Figure 4-6. Temperature dependences of the Seebeck coefficient of $Nd_xCo_4Sb_{12}$.

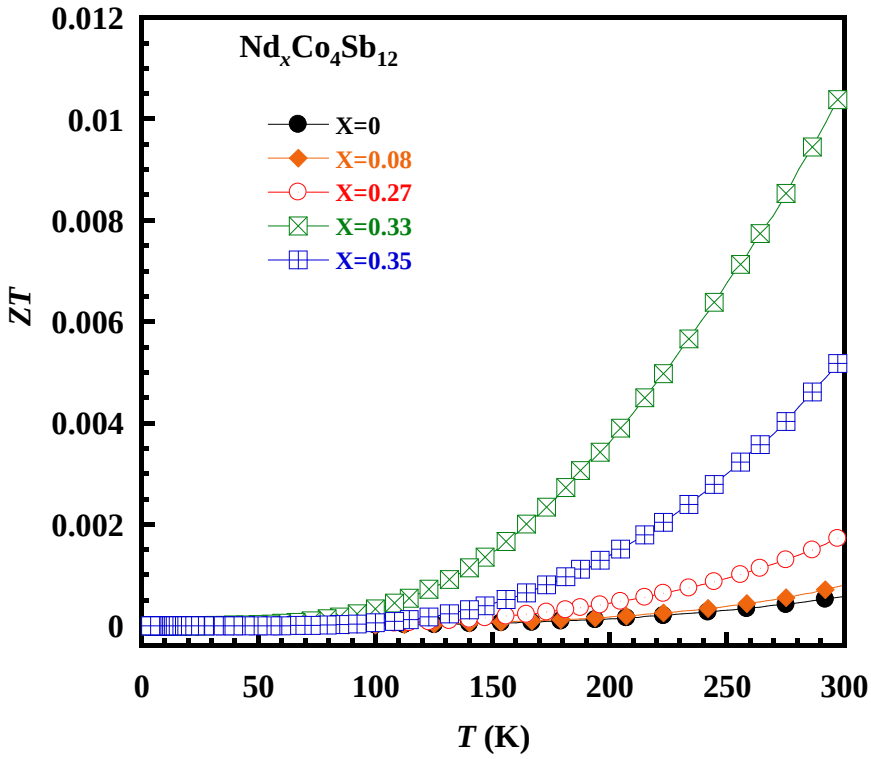

Figure 4-7. Temperature dependences of the dimensionless figure of merit of $Nd_xCo_4Sb_{12}$.

4.7 Summary

In this study, we have successfully synthesized the n-type filled skutterudite using HPHT technique. The actual Nd filling rate indicates an advantage of HPHT technique which can substantially increase the filling fraction into the voids of $CoSb_3$ compared with conventional synthesis techniques. The high filling fraction of Nd-filled skutterudite greatly suppresses the lattice thermal conductivity and approaches the κ_{min}. The lattice thermal conductivity of $Nd_{0.33}Co_4Sb_{12}$ has decreased to 2.49 W/mK at 300K. However, we can observed that the low of κ_l of single filled compared to double filled or multi-filled are higher effective for example $In_{0.13}Lu_{0.05}Co_4Sb_{12}$ of 2.0 W/mK and $Ba_{0.08}Yb_{0.14}Eu_{0.10}Co4Sb_{12.12}$ of 1.1 W/mK.[29,30)] It might possible to introduce lower κ_l by synthesizing double-filled or multi-filled preparing under high pressure. The optimal of Nd filled skutterudite shows significantly enhanced ZT value due to the increment of Nd filling rate, as high as 0.011 at room temperature. HPHT technique is one of the most attractive approaches to fabricating n-type filled skutterudites of TE material, with the advantages of speed, increased filling fraction and markedly decreased lattice thermal conductivity.

Chapter 5
Experimental Results of $La_xCo_4Sb_{12}$

5.1 Introduction

In chapter 5, we have studied the effect of lanthanum (La) 25% of Mm filled skutterudite under high pressure. The results have confirmed the high filling rate of La markedly decreased the lattice thermal conductivity to a greater than that of Ce and Nd filled skutterudite in chapter 3 and 4. Furthermore, the result of La filler, can be used to replace Mm as fillers and greatly reduction in κ_l. This chapter describes the characterization techniques on the samples in term of phases structures, lattice parameter, actual compositions, and thermoelectric properties of $La_xCo_4Sb_{12}$.

5.2 X-ray diffraction (XRD) of $La_xCo_4Sb_{12}$

Figure 5-1 shows x-ray diffraction patterns of filled skutterudite materials, which are mixture of each metal and antimony powder in the atomic ratio of $La_xCo_4Sb_{12}$ (x = 0 - 1), at room temperature and 4 GPa. While a small amount of impurity phase Sb and $CoSb_2$ were detected, most of the observed diffraction lines were indexable using the skutterudite structure. However, with La content lower than 0.8 the main peaks is split to two peaks and with increased La content the main of split peaks were changes to lower θ (red arrows) and finally, the split peaks disappear with x = 1.0 were shown below.

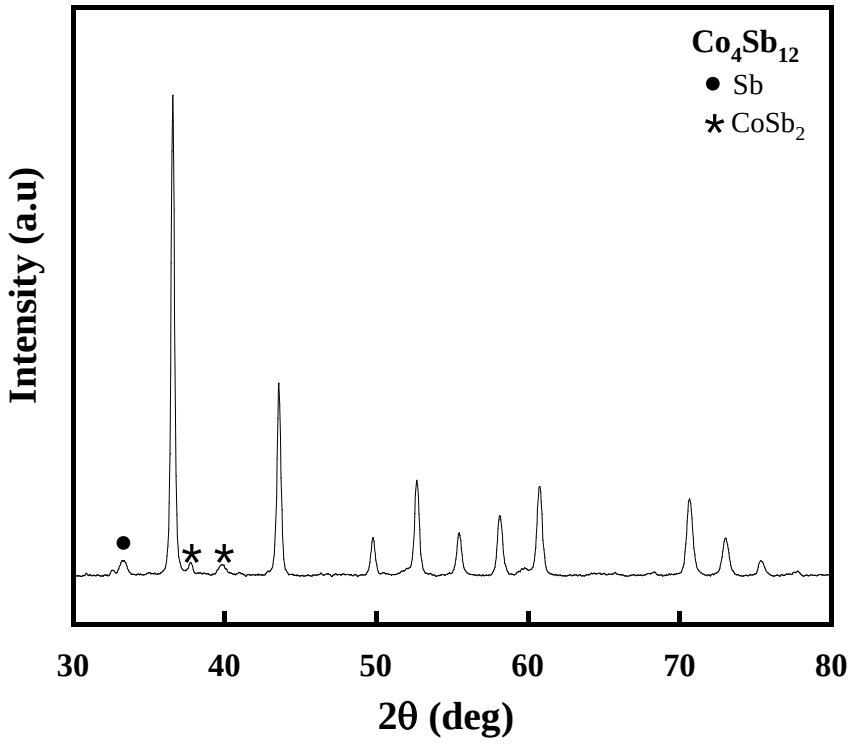
Co4Sb12
● Sb
∗ CoSb2
Intensity (a.u)
30
40
50
60
70
80
2θ (deg)

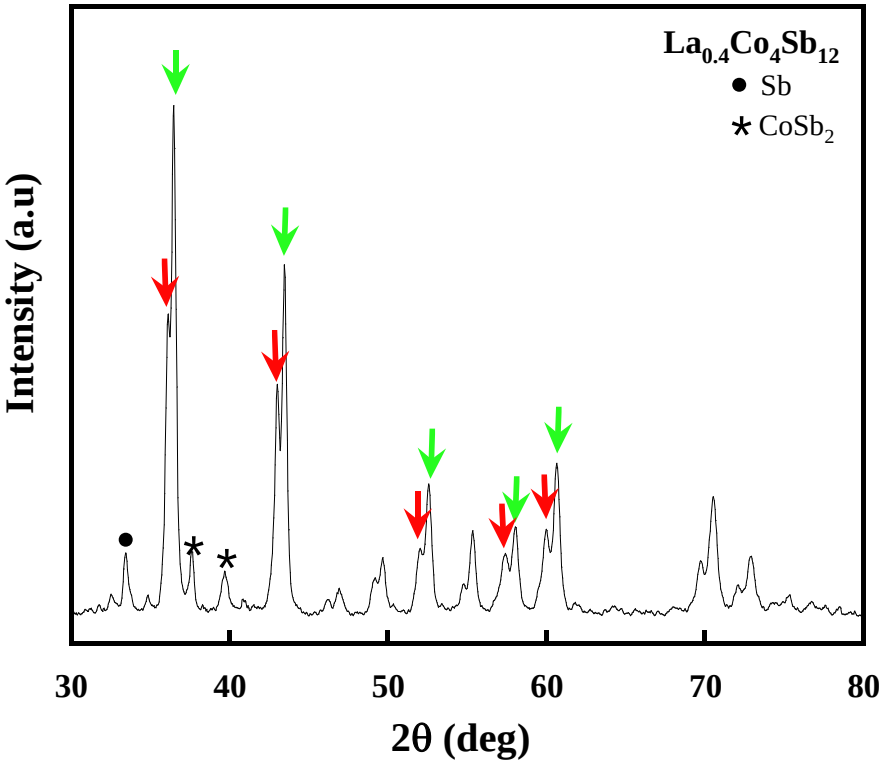
La0.4Co4Sb12
● Sb
∗ CoSb2
Intensity (a.u)
30
40
50
60
70
80
2θ (deg)

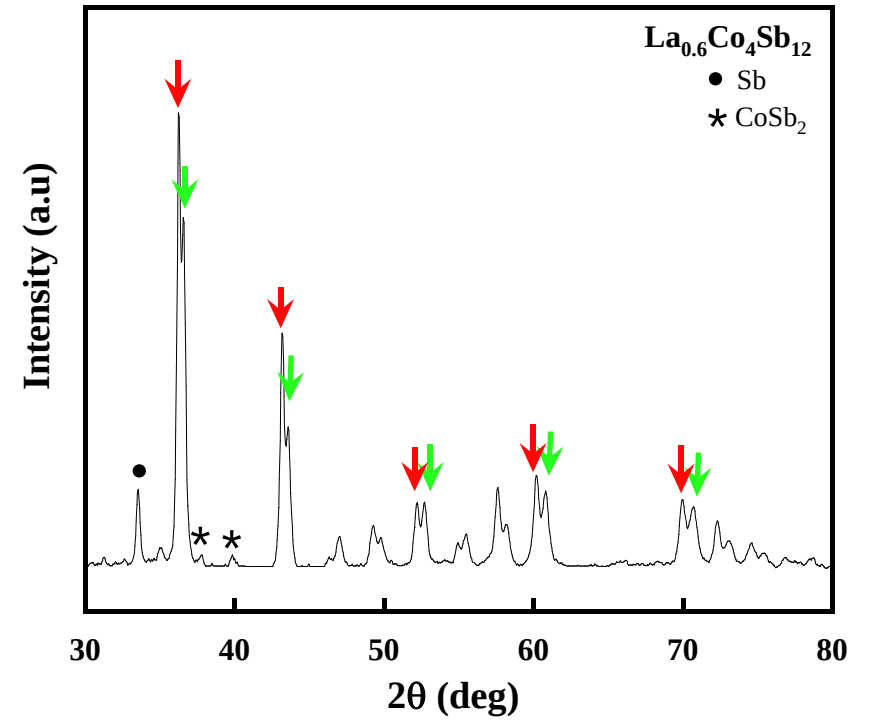
La0.6Co4Sb12
Sb
CoSb2
Intensity (a.u)
30
40
50
60
70
80
2θ (deg)

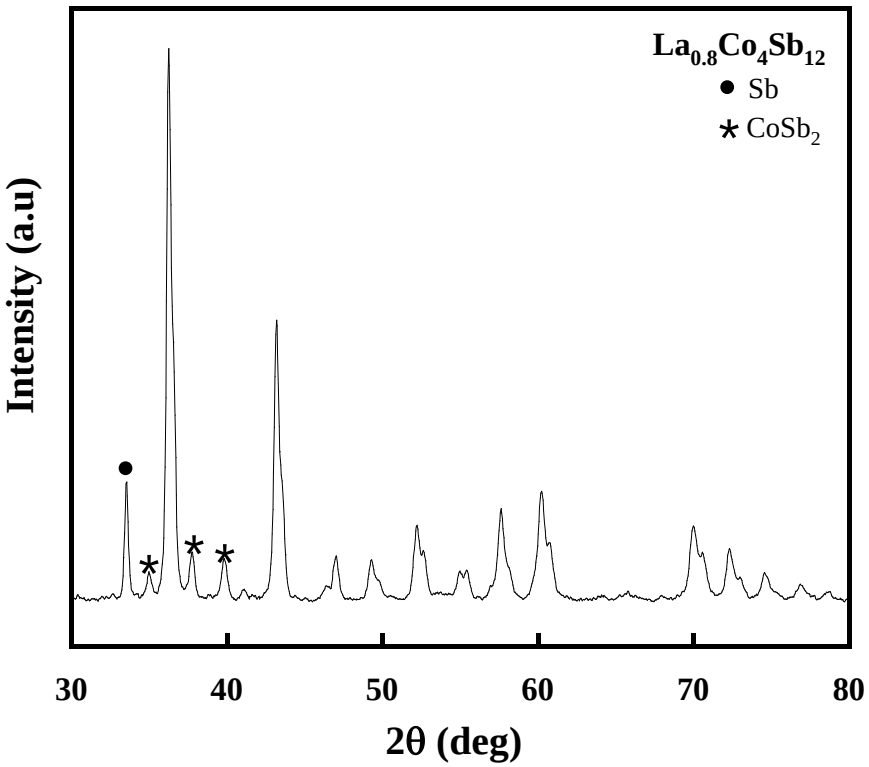
La0.8Co4Sb12
Sb
CoSb2
Intensity (a.u)
30
40
50
60
70
80
2θ (deg)

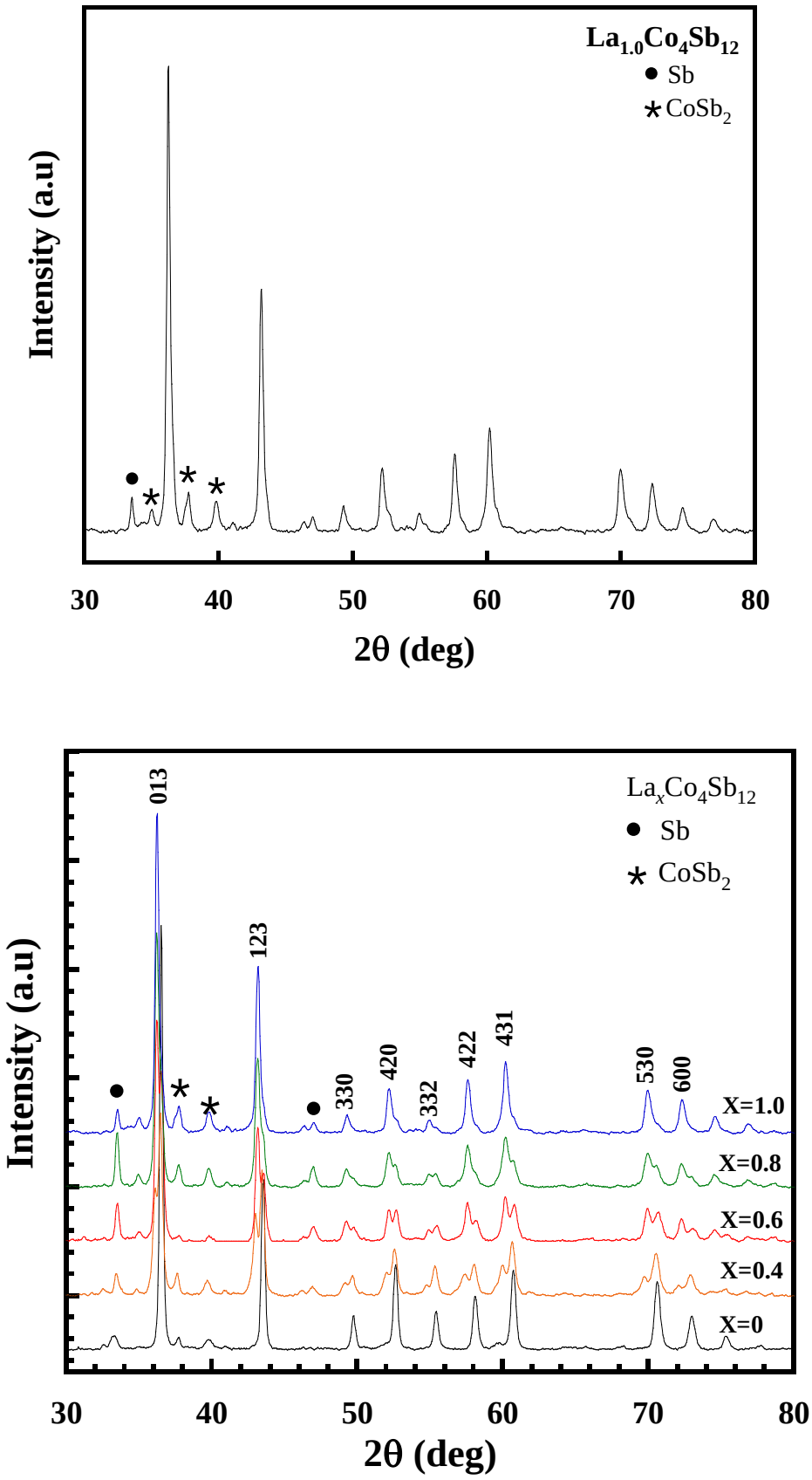

Figure 5-1. XRD pattern of a polycrystalline of $Nd_xCo_4Sb_{12}$.

5.3 Lattice constant and actual composition of $La_xCo_4Sb_{12}$

The lattice constant of La filled skutterudite is almost the same with Ce and Nd filled skutterudite in chapters 3 and 4. The lattice constants were determined in the same manner in this study and the saturate point was found to be about 9.12 Å while small filling of x = 0.4 also steeply increased to 9.12 Å, whereas for $CoSb_3$ the lattice constant data was 9.038 Å (see fig. 5-2, black line). The actual compositions evaluated by SEM and EDX were similar to those in the previous chapter. The SEM examination of La filled skutterudite samples are very fragile. The EDX has been used to examine the actual composition by point analysis, by comparing the atomic ratio. The actual filling fraction were shown in fig 5-2. The maximum La filling fraction of 0.28 see fig 5-2 (red line).

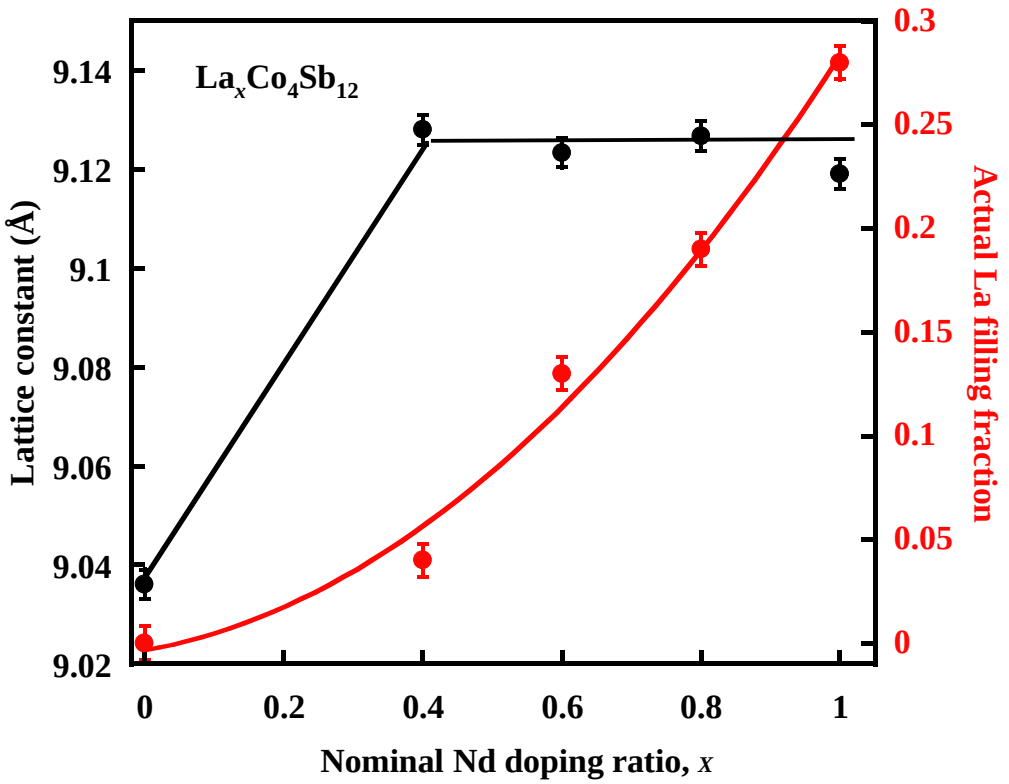

Figure 5-2. Lattice constant and actual La filling fraction vs nominal La doping rate.

5.4 The electrical resistivity (ρ) of $La_xCo_4Sb_{12}$

Temperature dependence of the electrical resistivity were shown in fig 5-3. The electrical resistivity reduced with increasing La-doping content and temperature, indicating a typical semiconductor behavior for all samples. After doping with La to a content maximum of 0.28, the electrical resistivity reduced with increasing La-doping. This might be due to the change of majority concentration and carriers generated with increasing temperature, which contrast with the mother compound of $CoSb_3$. $La_{0.28}Co_4Sb_{12}$ sample showed the lowest electrical resistivity of 17.58 $\mu\Omega$m at 300 K, which is lower than $CoSb_3$ sample of 353.39 $\mu\Omega$m at same temperature. This is mainly due to the electrons supplied by La-doping and also due to increasing the carrier concentrations. Thus, La-filled skutterudite improved the electrical resistivity of the Co_4Sb_{12} sample.

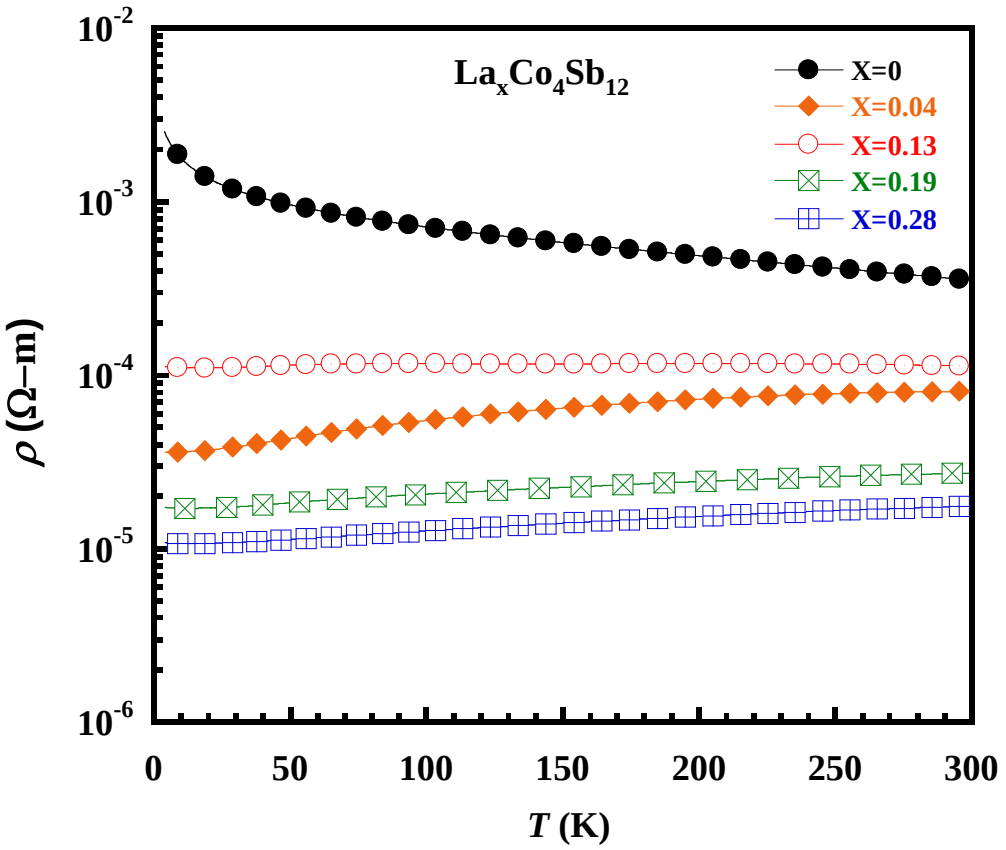

Figure 5-3. Temperature dependences of the electrical resistivity of $La_xCo_4Sb_{12}$.

5.5 The thermal transport property of $La_xCo_4Sb_{12}$

Figure 5-4 shown the temperature dependence of thermal conductivity (κ) of $La_xCo_4Sb_{12}$ bulk samples. The total thermal conductivity is the sum of electronic (κ_e) and lattice (κ_l) thermal conductivities. It was found that the thermal conductivity decreased with increasing La-doped content over the temperature. For the doped samples, $La_{0.28}Co_4Sb_{12}$ sample show the lowest value of thermal conductivity of 1.72 W/mK at 300 K, which is lower than $CoSb_3$ sample of 6.51 W/mK at same temperature. However, which subtraction of the electronic term the κ_l is lower than that of 1.31 W/mK see fig 5-5.

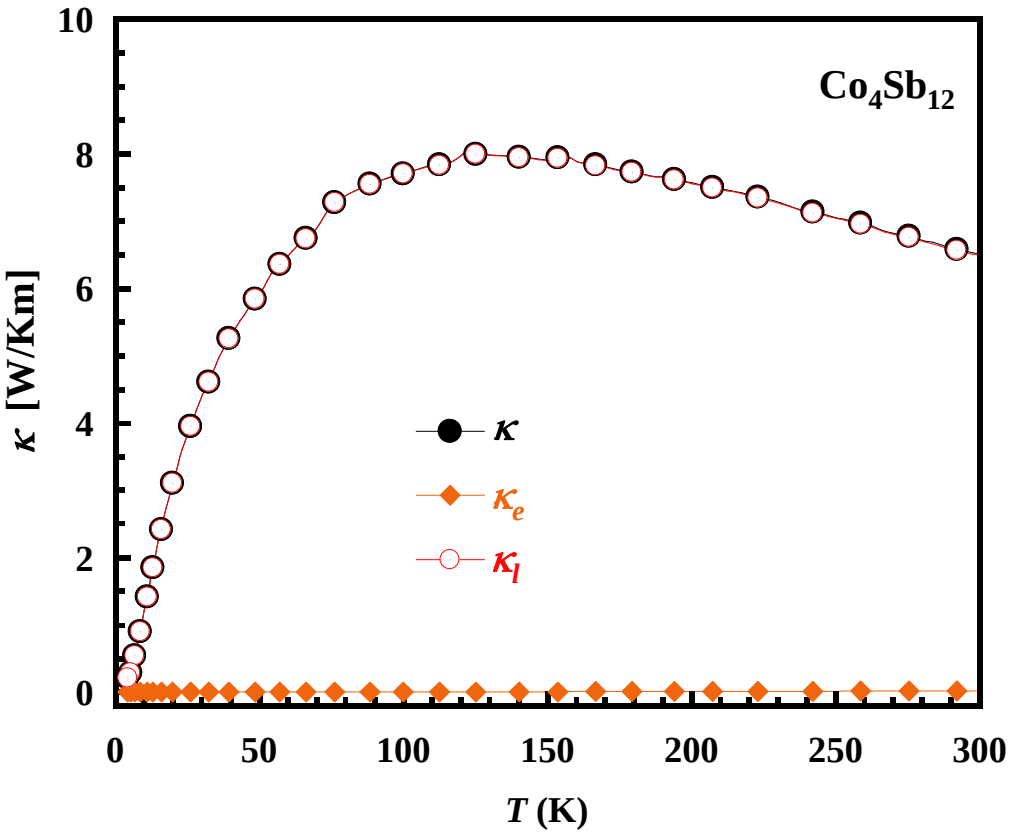

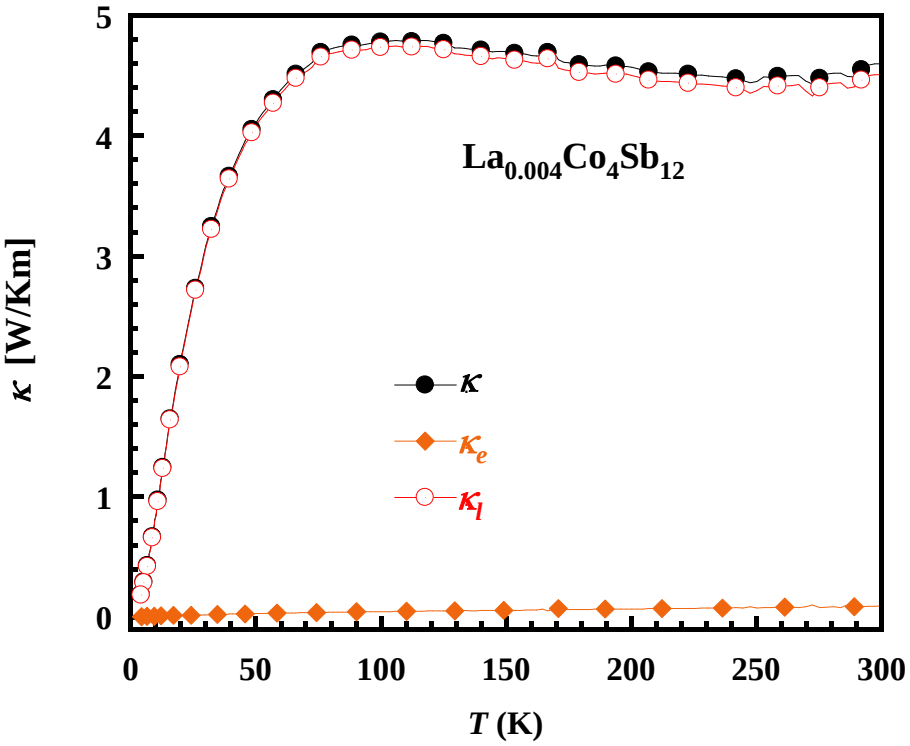
La0.004Co4Sb12
κ
κe
κl
κ [W/Km]
T (K)
0
1
2
3
4
5
0
50
100
150
200
250
300

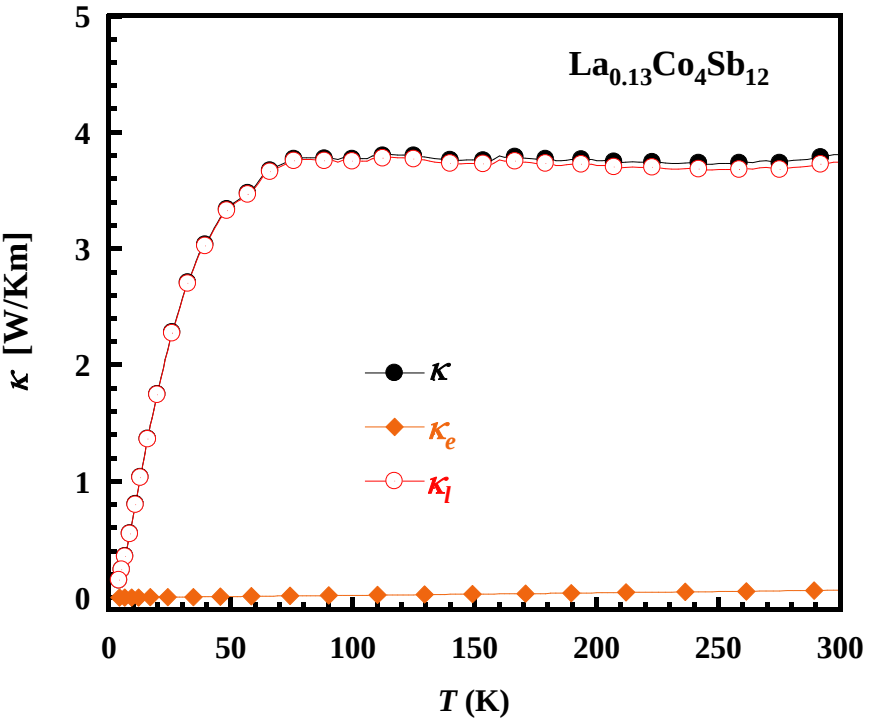
La0.13Co4Sb12
κ
κe
κl
κ [W/Km]
T (K)
0
1
2
3
4
5
0
50
100
150
200
250
300

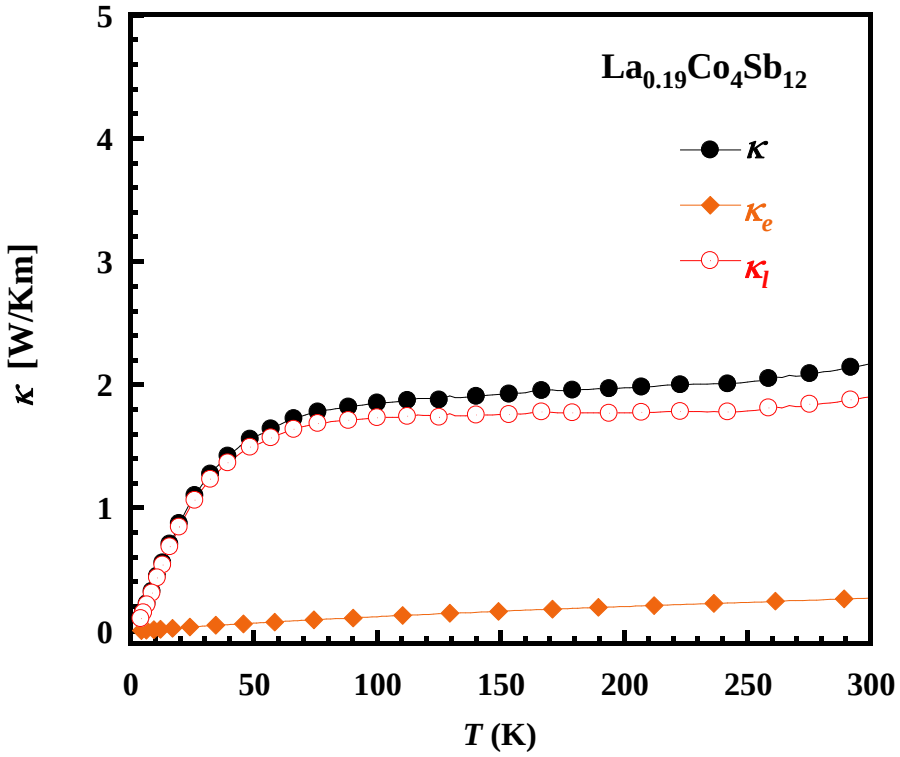
La0.19Co4Sb12
κ
κe
κl
κ [W/Km]
T (K)
0
1
2
3
4
5
0
50
100
150
200
250
300

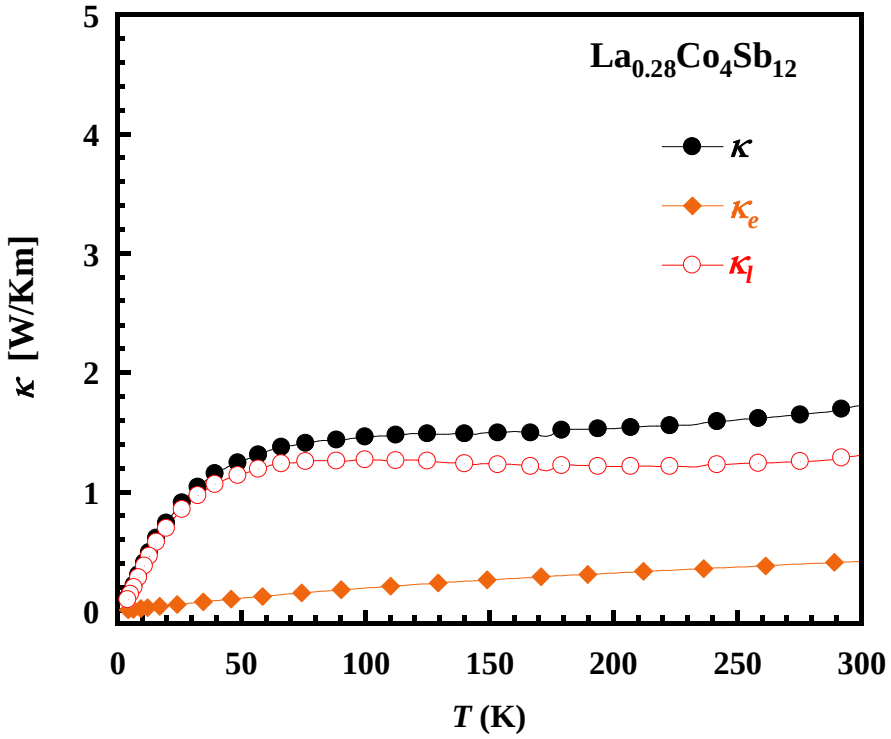
La0.28Co4Sb12
κ
κe
κl
κ [W/Km]
T (K)
0
1
2
3
4
5
0
50
100
150
200
250
300

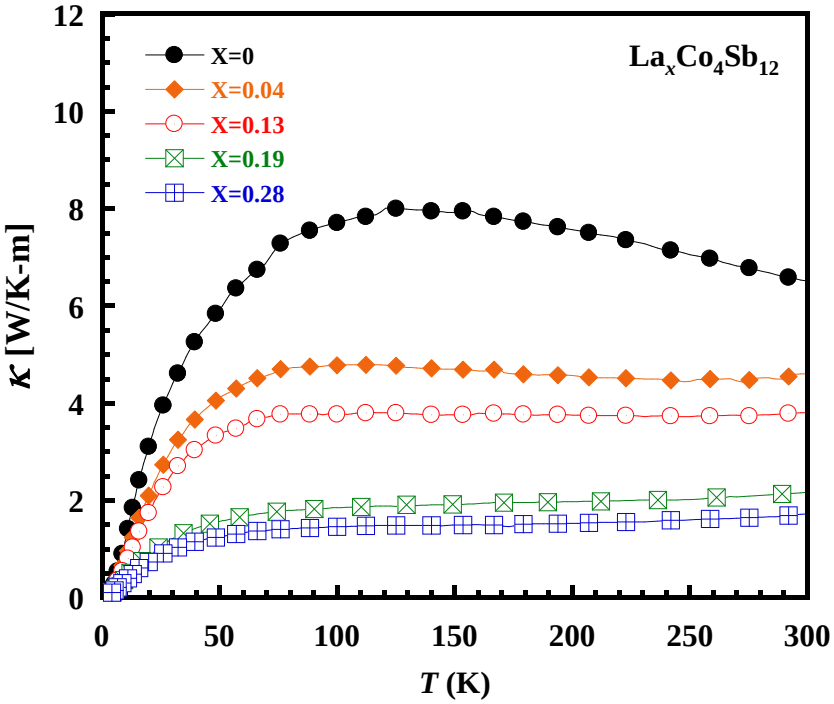

Figure 5-4. Temperature dependences of the thermal conductivity of $La_xCo_4Sb_{12}$.

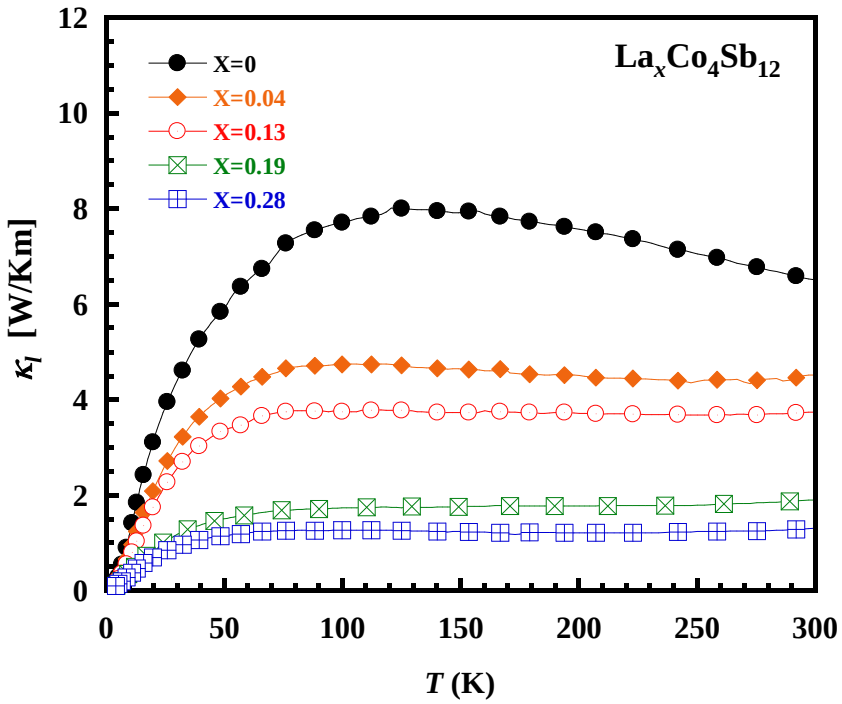

Figure 5-5. Temperature dependences of the lattice thermal conductivity of $La_xCo_4Sb_{12}$.

5.6 The seebeck coefficient and *ZT* value of $La_xCo_4Sb_{12}$

Regarding the temperature dependence of the Seebeck coefficient (*S*), as shows in fig 5-6, all samples of Nd filled skutterudites acquires negative Seebeck coefficients. The absolute Seebeck coefficient values improved with increasing La-doped content and temperature. The highest Seebeck coefficient value reached -55.21 μV/K at 300 K for $La_{0.28}Co_4Sb_{12}$ sample, which is changes to positive of undoped Co_4Sb_{12} sample of 56.59 μV/K at same temperature. This is mainly due to the electrons supplied by La-doping. The dimensionless figure of merit, *ZT* for $La_xCo_4Sb_{12}$ bulk samples as a function of temperature are displayed in Figure 5-7. It can be seen that the *ZT* values improved via increasing La-doped content and temperature. The maximum *ZT* value of 0.03 has been attained for $La_{0.28}Co_4Sb_{12}$ sample at 300 K.

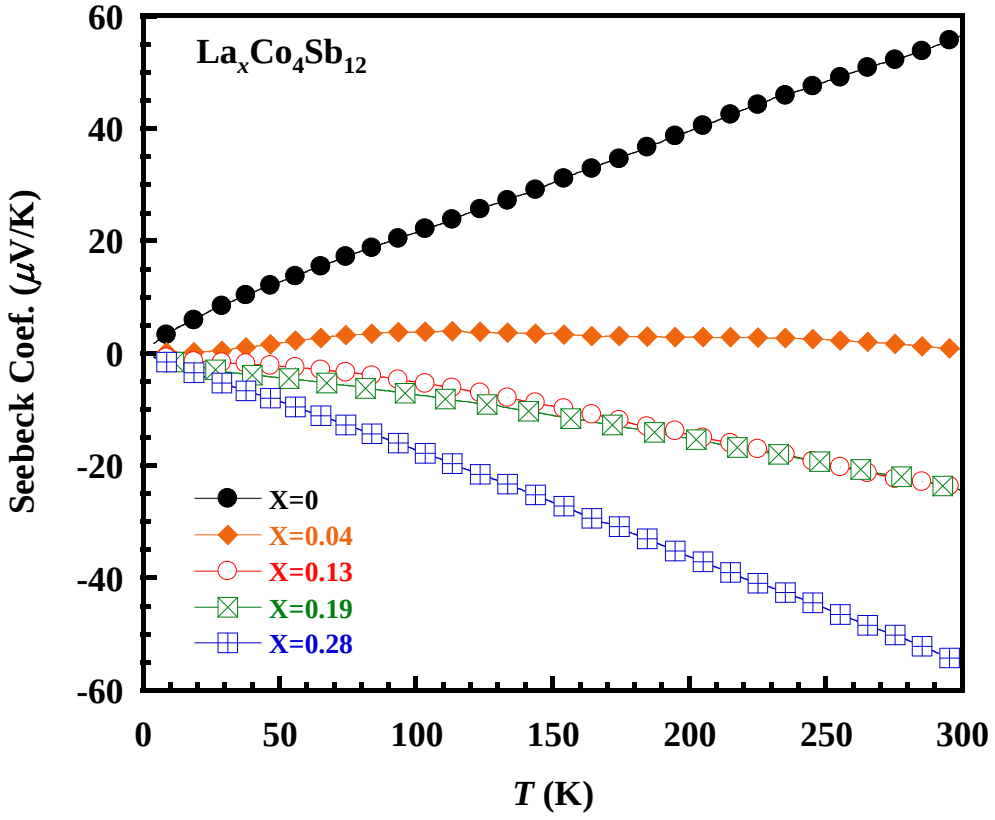

Figure 5-6. Temperature dependences of the Seebeck coefficient of $La_xCo_4Sb_{12}$.

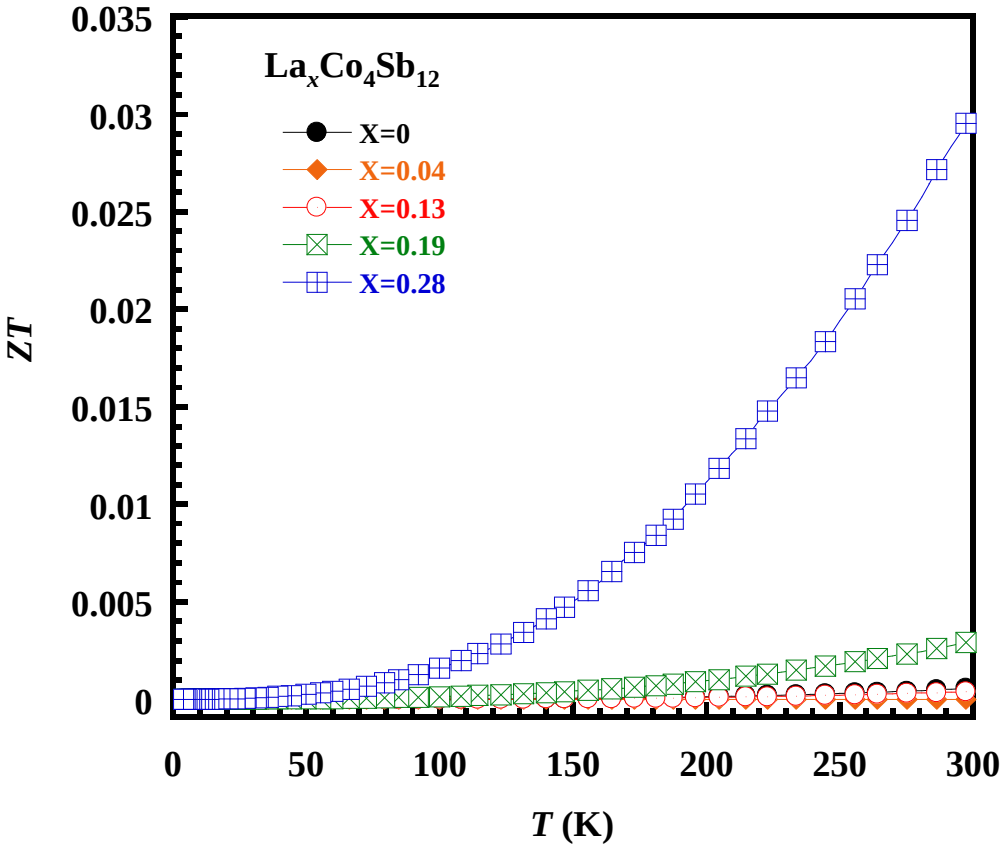

Figure 5-7. Temperature dependences of the dimensionless figure of merit of $La_xCo_4Sb_{12}$.

5.7 Summary

In this chapter, we have successfully synthesized the n-type filled skutterudite using HPHT technique. The actual La filling rate indicates an advantage of HPHT technique which can substantially increase the filling fraction. The use of HPHT can increase the lattice constant to 9.12, which is higher than any previous report so far. The high filling fraction of La-doping greatly suppresses the lattice thermal conductivity. The lattice thermal conductivity of $La_{0.28}Co_4Sb_{12}$ has decreased to 1.31 W/mK at 300K. The optimal of La filled skutterudite shows significantly enhanced *ZT* value of 0.03 at room temperature.

Chapter 6
TE performance at high temperature

6.1 Introduction

In chapter 6, we have continued studied TE properties from chapter 3, 4 and 5 evaluated at high temperature. However, the samples prepared under high pressure are very small and were sometimes fragile and easy to break become small pieces or powder, which are not suitable to evaluate the TE properties at high temperature. Therefore, we combined HPHT synthesis method using a multi-anvil press and spark plasma sintering (SPS) method. First, we removed impurity phases of samples and grind the samples, prepared under high pressure, into powder. Then, the powder was sintered by SPS at 60 MPa and 600 °C for 120 min. to obtain large and dense bulk samples suitable to evaluate the properties with high temperature region. The samples were shaped to discoid shape with 10 mm in diameter and 2 mm in height. The discoid shape samples were used for the thermal conductivity measurements with a laser flash method using an NETZSCH LFA457 system. For other measurements, the discoid samples were cut into rectangle with 2 mm in width, 2 mm in height, and 8 mm in length. The electrical resistivity and Seebeck coefficient were measured using ULVAC ZEM-3 system. Hall effect measurements were performed using the van der Pauw method under a magnetic field of 7 and -7T, were measurement by a thermal relaxation method (Quantum Design PPMS). However, after selected the samples which have highest *ZT* performance to sintering and measure at high temperature it was found that the actual compositions of samples after sintering by SPS technique are decreased to 0.13 and 0.17 for Ce- and Nd- filled skutterudite and the lattice constant decrease to 9.039 and 9.041 Angstrom respectively.

6.2 The electrical resistivity (ρ) at $T > 300$ K

Figure 6-1 shows the temperature dependence of the electrical resistivity ρ for $Ce_{0.13}Co_4Sb_{12}$ and $Nd_{0.17}Co_4Sb_{12}$ prepared by using HPHT synthesis and SPS technique. The data above 300 K for $CoSb_3$ are reference from Park *et al.*,.[31] Based compound of $CoSb_3$ shows semiconducting behavior, Ce- and Nd-doped samples exhibit semimetallic behavior. Furthermore, the values of ρ for $Ce_{0.13}Co_4Sb_{12}$ and $Nd_{0.17}Co_4Sb_{12}$ are much lower than that for $CoSb_3$. This suggests that they are heavily doped semiconductor, which can be attributed to increase of the electron concentration by doping of guest ions with high filling ratio. Moreover, high fillers Nd-doping of 0.17 exhibit greater the electrical conductivity than Ce fillers of 0.13.

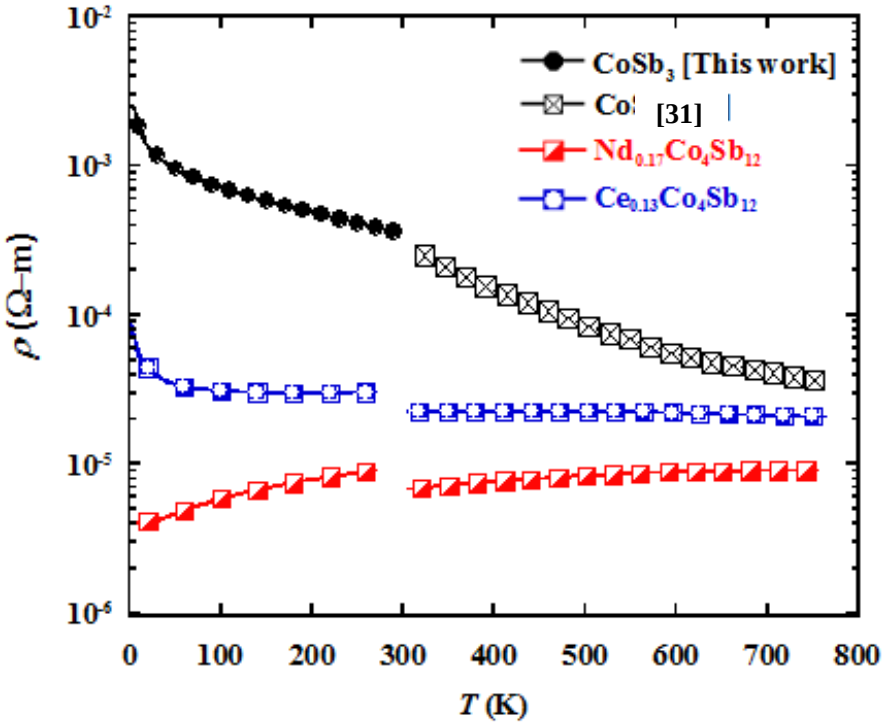

Figure 6-1. Temperature dependences of the electrical resistivity at $T > 300$ K.

6.3 The thermal conductivity at $T > 300$ K

Figure. 6-2 shows the temperature dependence of the total thermal conductivity κ and the lattice thermal conductivity κ_l in fig. 6-3, in the temperature range from 5 to 760 K for $Ce_{0.13}Co_4Sb_{12}$ and $Nd_{0.17}Co_4Sb_{12}$. The data above 300 K for $CoSb_3$ are reference from Park et al.[31] By filling Ce or Nd, both κ and κ_l decrease. The minimum values of κ_l are 2.57 $Wm^{-1}K^{-1}$ at 670 K and 2.11 $Wm^{-1}K^{-1}$ at 680 K for $Ce_{0.13}Co_4Sb_{12}$ and $Nd_{0.17}Co_4Sb_{12}$, respectively. A reduction in κ_l suggests that the rattling of Ce or Nd atoms. Furthermore, the random distribution of partly filled Ce or Nd ions in vacant sites causes more effective scattering of phonons. The difference in reduction of κ_l between Ce and Nd ions, having almost the same content as filling guest ions, could be due to the difference of mass and size of guest ions. The smaller and heavier rattler tends to induce more off-center behavior than the larger and lighter ions. Therefore, the κ_l of Nd filled skutterudite is lower than that of Ce filled skutterudite because Nd has a smaller ionic radius and larger mass than that of Ce.

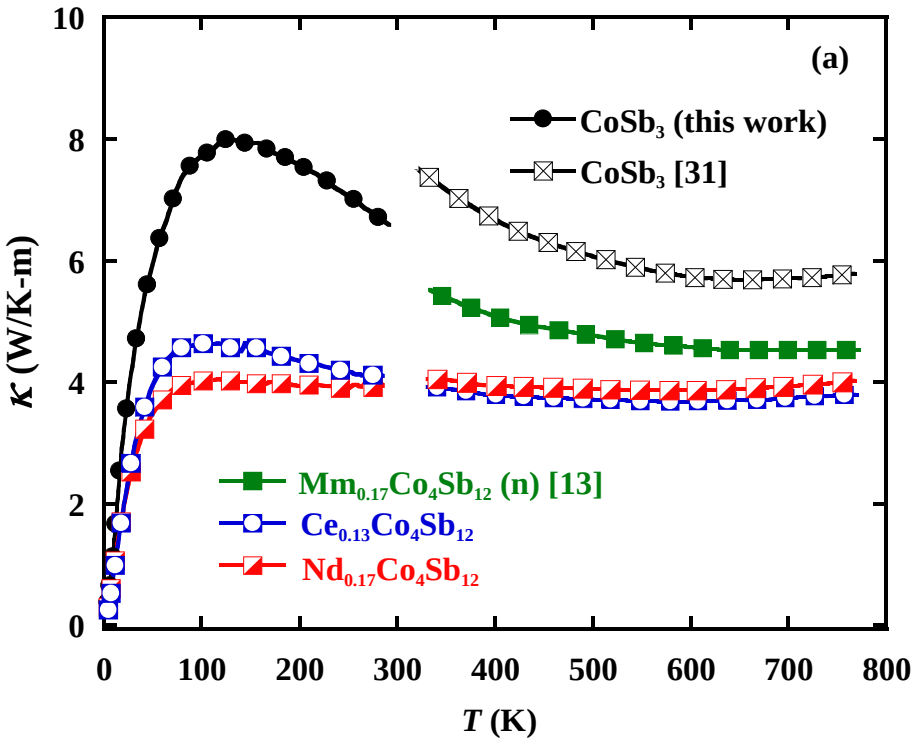

Figure 6-2. Temperature dependences of the thermal conductivity at $T > 300$ K.

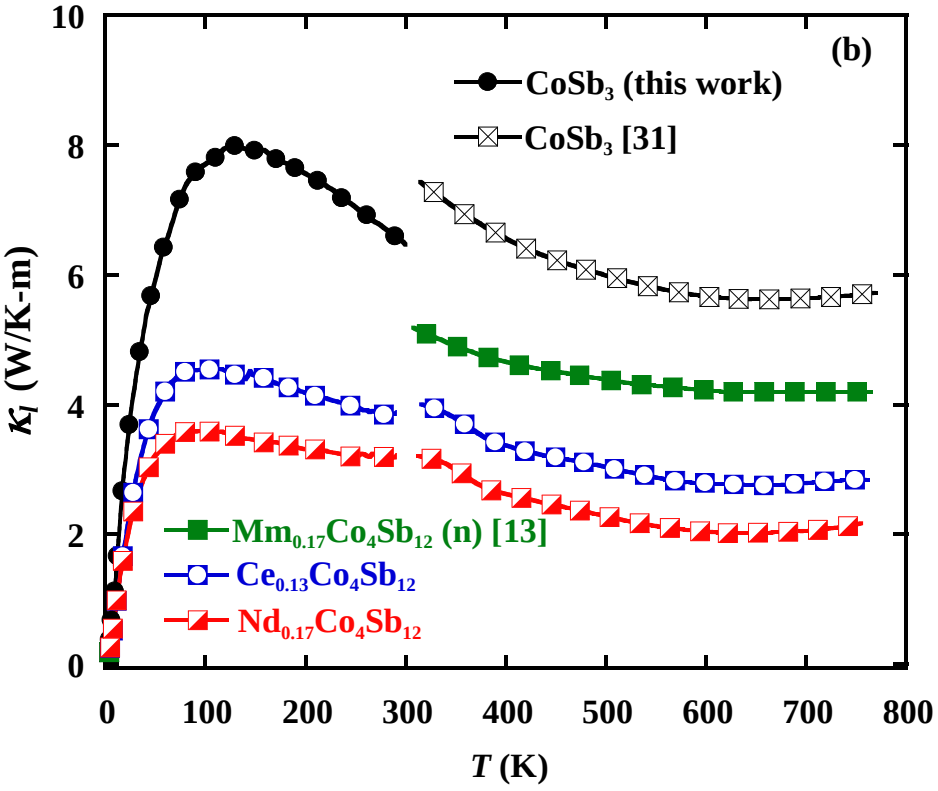

Figure 6-3. Temperature dependences of the thermal conductivity at $T > 300$ K.

6.4 The Seebeck coefficient at $T > 300$ K

The temperature dependence of Seebeck coefficients S for $Ce_{0.13}Co_4Sb_{12}$ and $Nd_{0.17}Co_4Sb_{12}$ is shown in fig. 6-4. The data above 300 K for $CoSb_3$ are also reference from Park et al.[31] While the S of $CoSb_3$ is positive, those for $Ce_{0.13}Co_4Sb_{12}$ and for $Nd_{0.17}Co_4Sb_{12}$ are negative, indicating transition from p-type to n-type conductor. The absolute values of S reach a maximum of 185 μV/K at 480 K for $Ce_{0.13}Co_4Sb_{12}$ and 166 μV/K at 690 K for $Nd_{0.17}Co_4Sb_{12}$. However, after 500 K with increasing temperature the trends of both samples are stable or a little bit increase, this due to the samples are become to intrinsic behaviors.

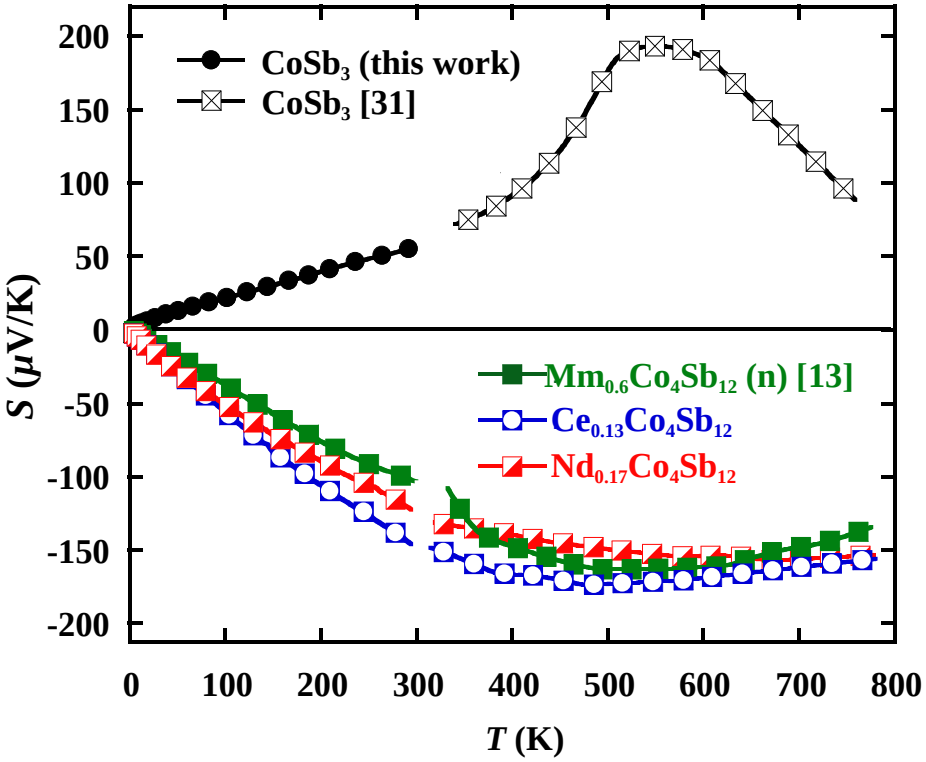

Figure 6-4. Temperature dependences of the Seebeck coefficient at $T > 300$ K.

6.5 The carrier concentration (n)

Figure 6-5 and 6-6 show the temperature dependence of the carrier concentration n and the carrier mobility μ for $Ce_{0.13}Co_4Sb_{12}$ and $Nd_{0.17}Co_4Sb_{12}$.

The n and μ were calculated from Hall coefficient R_H, namely, $n = 1/(eR_H)$ and $\mu = R_H/\rho$, where e is the elementary charge. The n for both $Ce_{0.13}Co_4Sb_{12}$ and $Nd_{0.17}Co_4Sb_{12}$ increases with increasing temperature because of the increased activation of charge carriers across the band gap while the n of $CoSb_3$ is nearly constant in the temperature range of 150–300 K. By filling Ce or Nd, the value of n inceases to 2.6×10^{20} cm^{-3} and 7.6×10^{20} cm^{-3} for $Ce_{0.13}Co_4Sb_{12}$ and $Nd_{0.17}Co_4Sb_{12}$, respectively, from 0.036×10^{20} cm^{-3} ($CoSb_3$) at 300 K. The μ for both $Ce_{0.13}Co_4Sb_{12}$ and $Nd_{0.17}Co_4Sb_{12}$ decreases with increasing temperature while the μ of $CoSb_3$ increases (Fig. 6-6). The μ at room temperature decreases from 220.99 cm^2V^{-1} s^{-1} for $CoSb_3$ to 7.86 and 8.66 cm^2V^{-1} s^{-1} for $Ce_{0.13}Co_4Sb_{12}$ and $Nd_{0.17}Co_4Sb_{12}$. The μ of both compounds exhibits a $T^{-3/2}$ behavior above 150 K. The results suggest that the carrier scattering mechanism is mainly acoustic phonon scattering.

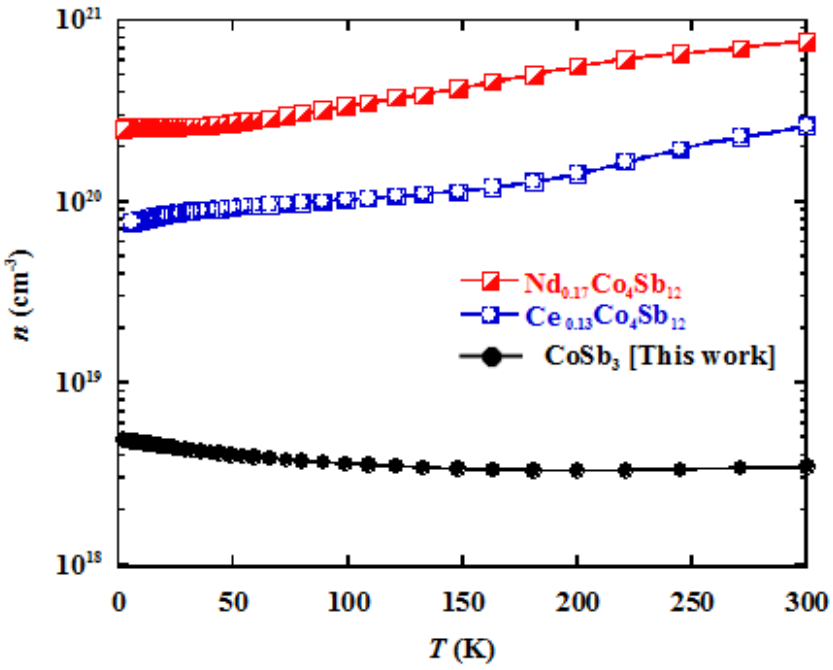

Figure 6-5. Temperature dependences of the Seebeck coefficient at $T > 300$ K.

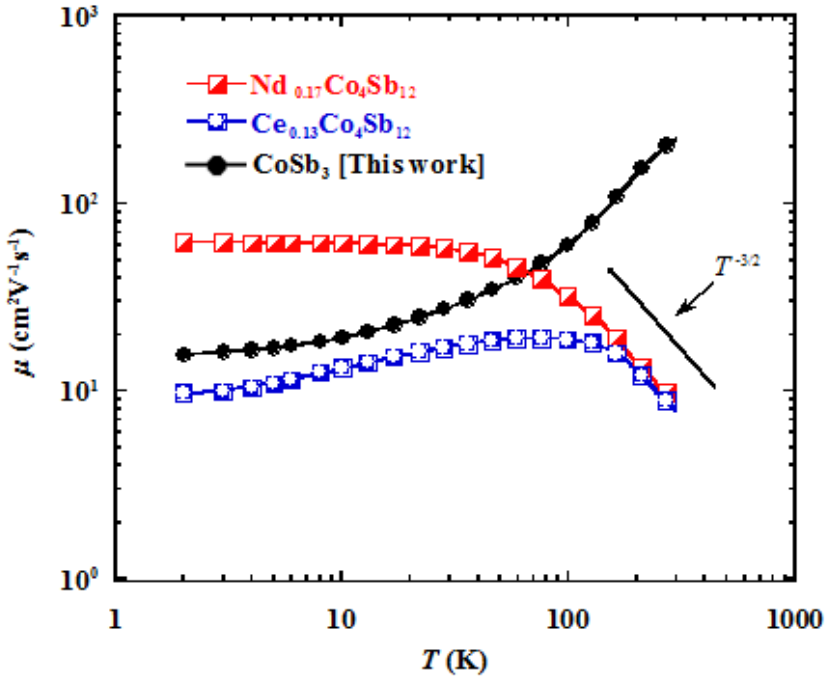

Figure 6-6. Temperature dependence of carrier mobility μ for $Ce_{0.13}Co_4Sb_{12}$ and $Nd_{0.17}Co_4Sb_{12}$.

6.6 The dimensionless figure of merit (ZT) at $T > 300$ K

Figure 6-7 shows the temperature dependence of dimensionless figure of merit (ZT). The maximum ZT values of 0.26 and 0.48 were achieved at 700 K for $Ce_{0.13}Co_4Sb_{12}$ and $Nd_{0.17}Co_4Sb_{12}$, respectively. The enhancement of ZT is mainly due to the high filling of guest ions and the change in carrier concentration. The use of HPHT synthesis not only make it possible to fill a wide variety of elements into Sb vacancies, but can also increase the upper limit of elements. High filling ratio of Ce or Nd ions in voids of $CoSb_3$ results in an improvement of the thermoelectric performance. Unfortunately, the use of SPS technique causes a deviation from the expected compositions, namely, reduction in filling ratio of guest ions. We have to develop a new technique to make large bulk samples with keeping high filling rate of samples prepared by HPHT synthesis.

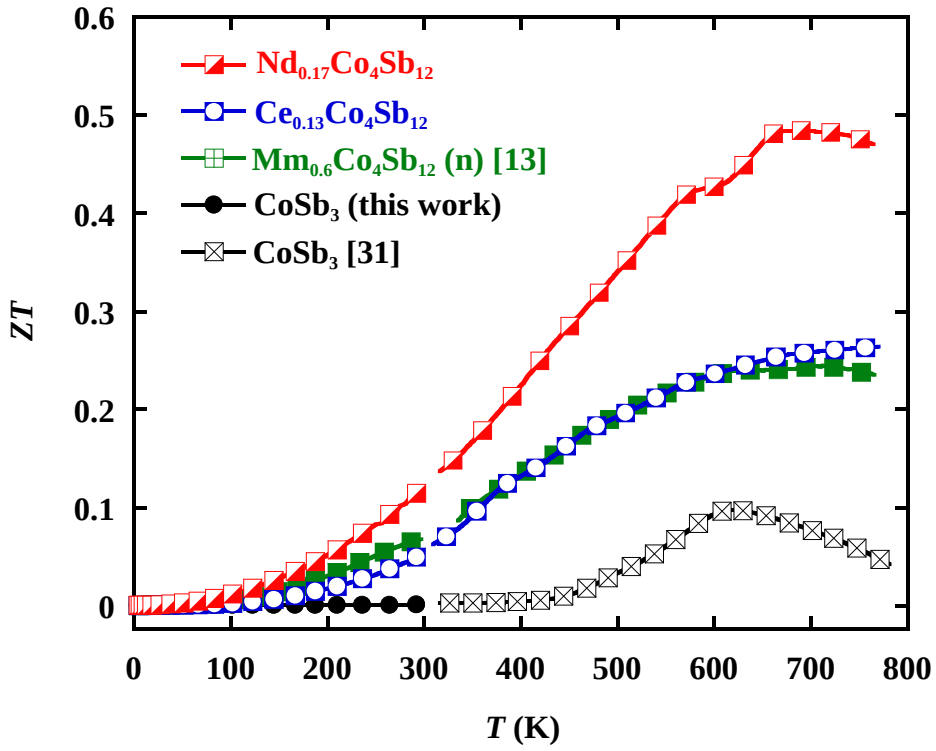

Figure 6-7. Temperature dependences of *ZT* at $T > 300$ K.

Chapter 7
Conclusion

In this study, we have successfully synthesized n-type filled skutterudite using HPHT technique. The actual Ce and Nd filling rate indicates an advantage of HPHT technique which can substantially increase the filling fraction into the voids of $CoSb_3$ compared with conventional synthesis techniques. The high filling fraction rate results in a significant suppression of κ_l. The lowest κ_l of this study is 2.11 W/mK at 680 K for $Nd_{0.17}Co_4Sb_{12}$**.** The maximum *ZT* values for $Ce_{0.13}Co_4Sb_{12}$ and $Nd_{0.17}Co_4Sb_{12}$ are 0.26 and 0.48 at 700 K, respectively. This work suggests that Nd filling is much effective for the improvement TE performance of $CoSb_3$-based compounds. Furthermore, the κ_l of double filled or multi-filled skutterudite compounds is generally lower than that of single filled compounds, which indicates the possibility of inducing lower κ_l by synthesizing double-filled or multi-filled skutterudites prepared by HPHT synthesis. Therefore, if we prepare Nd rich Mm, namely, "artificial Mm" instead of the nature Mm, the TE performance could be improved. In this way, the HPHT technique is one of the most attractive approaches to fabricating n-type filled skutterudite compounds, with the advantages of increasing filling fraction and markedly reduction of lattice thermal conductivity.

7.1 Suggestions

1) Spark Plasma Sintering (SPS) system is not suitable for combination of HPHT because the low pressure of SPS sintering cannot preserve the advantage of high filling rate. Therefore, finding the new method combine with HPHT technique is an importance.

2) Artificial compound of Mm synthesized under high pressure technique, it would be possible to achieve the higher *ZT* performance than (Mm) nature mischmetal.

3) If it is possible, we should synthesis a large bulk sample by using HPHT which suitable to measure with high temperature. It might be known the actual performance with high filling rate.

4) Studying the carrier concentration and carrier mobility is importance for tuning the majority concentration. This can lead to optimized TE material synthesized by HPHT technique.

Bibliography

1) T. Endo, S. Kawajiri, Y. Kojima, K. Takahashi, T. Baba, S. Ibaraki, T. Takahashi, and M. Shinohara, (2007).

2) C. Sprouse and C. Depcik, Appl. Therm. Eng. **51**, 711 (2013).

3) B. C. Sales, D. Mandrus, and R. K. Williams, Science (80-.). **272**, 1325 (1996).

4) T. M. Tritt, H. Böttner, and L. Chen, MRS Bull. **33**, 366 (2008).

5) G. S. Nolas and G. Fowler, J. Mater. Res. **20**, 3234 (2005).

6) J. Graff, S. Zhu, T. Holgate, J. Peng, J. He, and T. M. Tritt, J. Electron. Mater. **40**, 696 (2011).

7) L. Deng, X. P. Jia, T. C. Su, S. Z. Zheng, X. Guo, K. Jie, and H. A. Ma, Mater. Lett. **65**, 2927 (2011).

8) L. Zhang, A. Grytsiv, M. Kerber, P. Rogl, E. Bauer, M. J. Zehetbauer, J. Wosik, and G. E. Nauer, J. Alloy. Compd. **481**, 106 (2009).

9) S. Ballikaya, N. Uzar, S. Yildirim, J. R. Salvador, and C. Uher, J. Solid State Chem. **193**, 31 (2012).

10) Enn Velmre, Est. J. Eng. **13**, 276 (2007).

11) Chemical Engineering Science Group, Renew. Energy Devices **31**, 2006 (2008).

12) Y. Chen, Y. Kawamura, J. Hayashi, and C. Sekine, Jpn. J. Appl. Phys. **55**, 2 (2016).

13) C. Sekine, H. Kato, Y. Kawamura, and C.-H. Lee, Mater. Sci. Forum **879**, 1737 (2017).

14) G. S. Nolas, M. Kaeser, R. T. Littleton IV, and T. M. Tritt, Appl.Phys.Lett. **77**, 1855 (2000).

15) D. M. Rowe, *CRC Handbook of Thermoelectrics* (CRC-Press, 1995).

16) G. S. Nolas, D. T. Morelli, and T. M. Tritt, Annu. Rev. Mater. Sci. **29**, 89 (1999).

17) G. S. Nolas, J. L. Cohn, and G. A. Slack, Phys. Rev. B **58**, 164 (1998).

18) C. Sekine, H. Kato, M. Kanazawa, Y. Kawamura, K. Takeda, M. Matsuda, K. Kihou, C.-H. Lee, and H. Gotou, J. Phys. Conf. Ser. **502**, 012017 (2014).

19) Y. Chen, Y. Kawamura, J. Hayashi, and C. Sekine, Jpn. J. Appl. Phys. **54**, 055501 (2015).

20) H. Takizawa, M. Ito, K. Uheda, and T. Endo, J. Cer. Soc. Jpn. **108**, 530 (2000).

21) D. T. Morelli, G. P. Meisner, B. Chen, S. Hu, and C. Uher, Phys. Rev. B **56**, 7376 (1997).

22) Z. G. Mei, W. Zhang, L. D. Chen, and J. Yang, Phys. Rev. B **74**, 153202 (2006).

23) C. Chen, L. Zhang, J. Li, F. Yu, D. Yu, Y. Tian, and B. Xu, J. Alloys Compd. **699**, 751 (2017).

24) X. Li, Q. Zhang, Y. Kang, C. Chen, L. Zhang, D. Yu, Y. Tian, and B. Xu, J. Alloys Compd. **677**, 61 (2016).

25) Y. Liu, X. Li, Q. Zhang, L. Zhang, D. Yu, B. Xu, and Y. Tian, Materials (Basel). **9**, 257 (2016).

26) V. L. Kuznetsov, L. A. Kuznetsova, and D. M. Rowe, J. Phys. Condens. Matter **15**, 5035 (2003).

27) J. L. Mi, M. Christensen, E. Nishibori, V. Kuznetsov, D. M. Rowe, and B. B. Iversen, J. Appl. Phys. **107**, 0 (2010).

28) H. Mori, H. Anno, and K. Matsubara, Mater. Trans. **46**, 1476 (2005).

29) G. D. Tang, Z. H. Wang, X. N. Xu, Y. He, L. Qiu, and Y. W. Du, J. Electron. Mater. **40**, 611 (2011).

30) X. Shi, J. R. Salvador, J. Yang, and H. Wang, J. Electron. Mater. **38**, 930 (2009).

31) K.-H. Park and W.-S. Seo, J. Korean Phys. Soc. **65**, 491 (2008).

Appendix A

Sample preparation for SPS

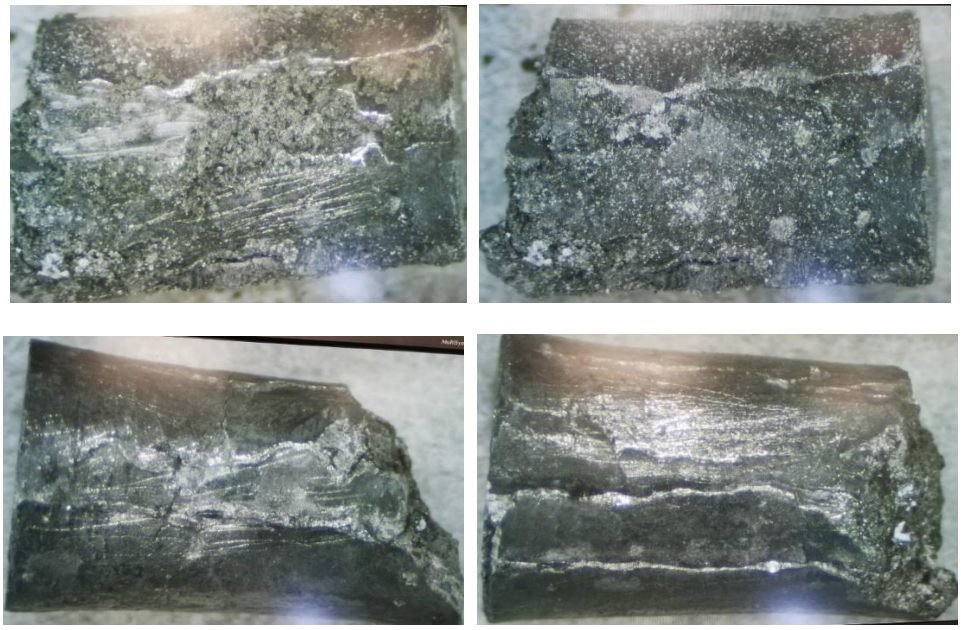

Remove impurity

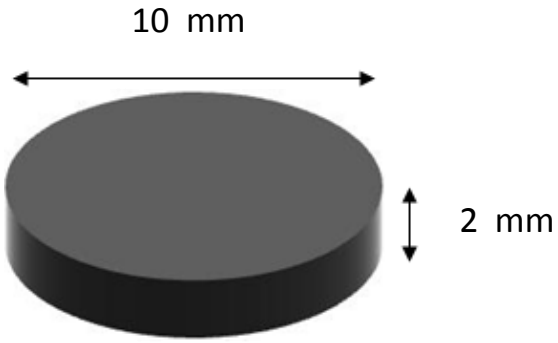

A sample size is required for LFA 457

$$\rho = \frac{m}{v}$$

$$m = 1.2\ g$$

Theoretical density for rare earth filled skutterudite approximately is 7.7 g/cm^3, therefor at least 1.2 g after remove impurity.

SPS Conditions	
Die Size (mm)	10
Amount of Sample (g)	1.5
Maximum Temperature (°C)	600
Heating Rate (°C/min)	15
Holding Time (min)	120
Pressure (MPa)	60

Appendix B

Conference list and Publication list

Conference list

- 2016 Rare Earth workshop, The Westin Rusutsu, Hokkaido - JAPAN.
- 2016 Joint Convention, The Hokkaido chapters of the institutes of electrical and information - JAPAN.
- 2017 Joint seminar on Environmental Science and Disaster Mitigation Research (JSED 2017) - JAPAN.
- 2017 The 28th Rare Earth Research conference, (28th RERC) -Ames, IOWA STATE, USA.
- 2017 Japan-Thailand Joint Seminar and International Symposium - (MIER 2017) - THAILAND.
- 2018 The 37th International Conference on Thermoelectric (ICT 2018) - CAEN, FRANCE.
- 2018 Rare Earth workshop, Lake Toyako, Hokkaido - JAPAN

Public list

- Thermoelectric properties of partially filled skutterudites $R_xCo_4Sb_{12}$ (R = Ce and Nd) synthesized under high pressures